

Validation of Computational Fluid Dynamics Methods Using Prototypic Light Water Reactor Spent Fuel Assembly Thermal-Hydraulic Data

AVAILABILITY OF REFERENCE MATERIALS IN NRC PUBLICATIONS

NRC Reference Material

As of November 1999, you may electronically access NUREG-series publications and other NRC records at the NRC's Public Electronic Reading Room at <http://www.nrc.gov/reading-rm.html>. Publicly released records include, to name a few, NUREG-series publications; *Federal Register* notices; applicant, licensee, and vendor documents and correspondence; NRC correspondence and internal memoranda; bulletins and information notices; inspection and investigative reports; licensee event reports; and Commission papers and their attachments.

NRC publications in the NUREG series, NRC regulations, and Title 10, "Energy," in the *Code of Federal Regulations* may also be purchased from one of these two sources.

1. The Superintendent of Documents

U.S. Government Publishing Office
Mail Stop SSOP
Washington, DC 20402-0001
Internet: <http://bookstore.gpo.gov>
Telephone: 1-866-512-1800
Fax: (202) 512-2104

2. The National Technical Information Service

5301 Shawnee Road
Alexandria, VA 22161-0002
<http://www.ntis.gov>
1-800-553-6847 or, locally, (703) 605-6000

A single copy of each NRC draft report for comment is available free, to the extent of supply, upon written request as follows:

U.S. Nuclear Regulatory Commission

Office of Administration
Publications Branch
Washington, DC 20555-0001
E-mail: distribution_resource@nrc.gov
Facsimile: (301) 415-2289

Some publications in the NUREG series that are posted at the NRC's Web site address <http://www.nrc.gov/reading-rm/doc-collections/nuregs> are updated periodically and may differ from the last printed version. Although references to material found on a Web site bear the date the material was accessed, the material available on the date cited may subsequently be removed from the site.

Non-NRC Reference Material

Documents available from public and special technical libraries include all open literature items, such as books, journal articles, transactions, *Federal Register* notices, Federal and State legislation, and congressional reports. Such documents as theses, dissertations, foreign reports and translations, and non-NRC conference proceedings may be purchased from their sponsoring organization.

Copies of industry codes and standards used in a substantive manner in the NRC regulatory process are maintained at—

The NRC Technical Library

Two White Flint North
11545 Rockville Pike
Rockville, MD 20852-2738

These standards are available in the library for reference use by the public. Codes and standards are usually copyrighted and may be purchased from the originating organization or, if they are American National Standards, from—

American National Standards Institute

11 West 42nd Street
New York, NY 10036-8002
<http://www.ansi.org>
(212) 642-4900

Legally binding regulatory requirements are stated only in laws; NRC regulations; licenses, including technical specifications; or orders, not in NUREG-series publications. The views expressed in contractor-prepared publications in this series are not necessarily those of the NRC.

The NUREG series comprises (1) technical and administrative reports and books prepared by the staff (NUREG-XXXX) or agency contractors (NUREG/CR-XXXX), (2) proceedings of conferences (NUREG/CP-XXXX), (3) reports resulting from international agreements (NUREG/IA-XXXX), (4) brochures (NUREG/BR-XXXX), and (5) compilations of legal decisions and orders of the Commission and Atomic and Safety Licensing Boards and of Directors' decisions under Section 2.206 of NRC's regulations (NUREG-0750).

DISCLAIMER: This report was prepared as an account of work sponsored by an agency of the U.S. Government. Neither the U.S. Government nor any agency thereof, nor any employee, makes any warranty, expressed or implied, or assumes any legal liability or responsibility for any third party's use, or the results of such use, of any information, apparatus, product, or process disclosed in this publication, or represents that its use by such third party would not infringe privately owned rights.

Validation of Computational Fluid Dynamics Methods Using Prototypic Light Water Reactor Spent Fuel Assembly Thermal-Hydraulic Data

Manuscript Completed: November 2016

Date Published: March 2017

Prepared by:

G. Zigh

S. Gonzalez

ABSTRACT

Applicants submit spent nuclear fuel dry storage cask designs to the U.S. Nuclear Regulatory Commission (NRC) for certification under Title 10 of the *Code of Federal Regulations* (10 CFR) Part 72, "Licensing Requirements for the Independent Storage of Spent Nuclear Fuel, High-Level Radioactive Waste, and Reactor-Related Greater Than Class C Waste." The NRC staff performs its technical review of these designs in accordance with 10 CFR Part 72 and NUREG-1536, "Standard Review Plan for Spent Fuel Dry Storage Systems at a General License Facility," Revision 1, issued July 2010. To ensure that the cask and fuel material temperatures of the dry cask storage system remain within the allowable limits or criteria for normal, off-normal, and accident conditions, the NRC staff performs a thermal review as part of the technical review.

Recent applications increasingly have used thermal-hydraulic analyses using computational fluid dynamics (CFD) codes (e.g., ANSYS FLUENT) to demonstrate the adequacy of the thermal design. The NRC Office of Nuclear Material Safety and Safeguards asked the NRC Office of Nuclear Regulatory Research to perform validation studies of the FLUENT CFD code to assist it in making regulatory decisions to ensure adequate protection for storage and transportation casks. The validation studies were based on preignition data (separate effect tests) obtained from the following previous studies:

- NUREG/CR-7143, "Characterization of Thermal-Hydraulic and Ignition Phenomena in Prototypic, Full-Length Boiling Water Reactor Spent Fuel Pool Assemblies After a Postulates Complete Loss-of Coolant Accident," issued March 2013
- NUREG/CR-7215, "Spent Fuel Pool Project Phase I: Pre-Ignition and Ignition Testing of a Single Commercial 17x17 Pressurized Water Reactor Spent Fuel Assembly under Complete Loss of Coolant Accident Conditions," issued April 2016
- NUREG/CR-7216, "Spent Fuel Pool Project Phase II: Pre-Ignition and Ignition Testing of a 1x4 Commercial 17x17 Pressurized Water Reactor Spent Fuel Assemblies under Complete Loss of Coolant Accident Conditions," issued April 2016

The fuel assembly experimental data from these studies provided reliable information for various fuel assembly heat loads that can be used to validate the analytical methods. Combined with current methods to determine modeling and application uncertainty, the measured data offered additional confirmation on the adequacy of the applied analytical methods.

The research summarized in this report relates to the CFD validation studies performed for a single test assembly of a full-length commercial 17x17 pressurized-water reactor (PWR) fuel bundle; a 17x17 PWR 1x4 configuration where the center fuel assembly was electrically heated and the four surrounding assemblies were unheated; and, a single test assembly for a full-length commercial 9x9 boiling-water reactor fuel bundle. For each of these configurations, a detailed and porous media model were developed to validate the results based on the experimental data and conducted parametric studies to assess model sensitivity. The grid conversion index method published by the American Society of Mechanical Engineers (ASME), "Standard for Verification and Validation in Computational Fluid Dynamics and Heat Transfer," was used to calculate the discretization uncertainty of the model.

CONTENTS

ABSTRACT	iii
LIST OF FIGURES	vii
LIST OF TABLES	xi
EXECUTIVE SUMMARY	xiii
ABBREVIATIONS	xv
1 INTRODUCTION	1-1
1.1 Pressurized-Water Reactor Single Assembly	1-1
1.2 Pressurized-Water Reactor 1x4 Assembly Configuration	1-2
1.3 Boiling-Water Reactor Single Assembly	1-4
1.4 Computational Fluid Dynamics Model.....	1-6
2 COMPUTATIONAL FLUID DYNAMICS MODELING	2-1
2.1 Detailed Model	2-1
2.2 Porous Model.....	2-8
3 RESULTS AND DISCUSSION	3-1
3.1 Pressurized-Water Reactor Single Assembly (Cell 2: 223.4 mm).....	3-1
3.1.1 Power—1 kW (Steady State).....	3-1
3.1.2 Power—1 kW (Transient).....	3-5
3.1.3 Power—0.5 kW (Steady State).....	3-13
3.2 Pressurized-Water Reactor Single Assembly (Cell 1: 221.3 mm).....	3-15
3.2.1 Power—1 kW (Steady State).....	3-15
3.2.2 Power—1 kW (Transient).....	3-17
3.3 Pressurized-Water Reactor 1x4 Assembly Configuration	3-18
3.3.1 Power—1 kW (Steady State).....	3-18
3.3.2 Power—1 kW (Transient).....	3-21
3.4 Boiling-Water Reactor Single Assembly	3-26
3.4.1 Power—1,369 W (Steady State)	3-26
3.4.2 Power—1,369 W (Transient)	3-28
3.4.3 Power—2,236 W (Steady State)	3-32
4 COMPUTATIONAL FLUID DYNAMICS DISCRETIZATION ERROR ANALYSIS (GRID CONVERGENCE INDEX)	4-1
4.1 Peak Cladding Temperature	4-3
4.2 Mass Flow Rate	4-4
5 CONCLUSION	5-1
6 REFERENCES	6-1

LIST OF FIGURES

Figure 1-1	Various components in a typical 17x17 PWR fuel assembly	1-1
Figure 1-2	Layout of the Phase II test assembly	1-2
Figure 1-3	Dimensions of the as-built pool rack and the design insulation thickness.....	1-3
Figure 1-4	Arrangement of insulation, radiation barriers, and external thermocouples	1-5
Figure 1-5	Arrangement of drain holes.....	1-5
Figure 1-6	CFD PWR single assembly cross sections of the detailed and porous models	1-6
Figure 2-1	Detailed PWR single assembly (Cell 2 illustrated)—boundary conditions	2-1
Figure 2-2	Detailed PWR single assembly top and bottom views (Cell 2 illustrated)— boundary conditions.....	2-2
Figure 2-3	Detailed BWR single assembly—boundary conditions (1/4 symmetry)	2-2
Figure 2-4	Detailed BWR single assembly top and bottom views—boundary conditions	2-3
Figure 2-5	Detailed PWR 1x4 configuration—boundary conditions	2-3
Figure 2-6	Detailed PWR 1x4 configuration top and bottom views—boundary conditions	2-3
Figure 2-7	2D model to calculate k_{eff} for PWR single assembly (Cell 1 shown)	2-9
Figure 2-8	2D model to calculate k_{eff} for 1x4 PWR configuration (peripheral assembly)	2-10
Figure 2-9	Porous PWR single assembly (Cell 2 illustrated)—boundary conditions	2-17
Figure 2-10	Porous PWR single assembly top and bottom views (Cell 2 illustrated)— boundary conditions.....	2-17
Figure 2-11	Porous PWR 1x4 configuration—boundary conditions	2-18
Figure 2-12	Porous PWR 1x4 configuration top and bottom views—boundary conditions	2-18
Figure 2-13	Porous BWR single assembly—boundary conditions	2-19
Figure 2-14	Porous BWR single assembly top and bottom views—boundary conditions	2-19
Figure 3-1	Detailed configuration—PWR single assembly Cell 2.....	3-2
Figure 3-2	Porous configuration—PWR single assembly Cell 2	3-2
Figure 3-3	Porous configuration for extended models—PWR single assembly Cell 2.....	3-3
Figure 3-4	PWR Cell 2 steady-state PCT as a function of height at 1 kW.....	3-4
Figure 3-5	PWR Cell 2 steady-state pool cell wall maximum temperature as a function of height at 1 kW	3-4
Figure 3-6	PWR Cell 2 steady-state exterior wall maximum temperature as a function of height at 1 kW	3-5
Figure 3-7	PWR Cell 2 PCT as a function of time at 1 kW	3-6
Figure 3-8	PWR Cell 2 mass flow rate as a function of time at 1 kW	3-6
Figure 3-9	PWR Cell 2 pool cell wall maximum temperature as a function of time at 1 kW	3-7
Figure 3-10	PWR Cell 2 exterior wall maximum temperature as a function of time at 1 kW	3-7
Figure 3-11	PWR Cell 2 PCT as a function of height at 1 kW at 20 hours	3-8
Figure 3-12	PWR Cell 2 pool cell wall maximum temperature as a function of height at 1 kW at 20 hours.....	3-8
Figure 3-13	PWR Cell 2 exterior wall maximum temperature as a function of height at 1 kW at 20 hours.....	3-9
Figure 3-14	PWR Cell 2 PCT as a function of time at 1 kW	3-10
Figure 3-15	PWR Cell 2 mass flow rate as a function of time at 1 kW	3-10
Figure 3-16	PWR Cell 2 pool cell wall maximum temperature as a function of time at 1 kW ...	3-11
Figure 3-17	PWR Cell 2 exterior wall maximum temperature as a function of time at 1 kW	3-11
Figure 3-18	PWR Cell 2 PCT as a function of height at 1 kW at 20 hours	3-12
Figure 3-19	PWR Cell 2 pool cell wall maximum temperature as a function of height at 1 kW at 20 hours.....	3-12
Figure 3-20	PWR Cell 2 exterior wall maximum temperature as a function of height at 1 kW at 20 hours.....	3-13

Figure 3-21	PWR Cell 2 steady-state PCT as a function of height at 0.5 kW.....	3-14
Figure 3-22	PWR Cell 2 steady-state pool cell wall maximum temperature as a function of height at 0.5 kW.....	3-14
Figure 3-23	PWR Cell 2 steady-state exterior wall maximum temperature as a function of height at 0.5 kW.....	3-15
Figure 3-24	PWR Cell 1 steady-state PCT as a function of height at 1 kW.....	3-16
Figure 3-25	PWR Cell 1 steady-state pool cell wall temperature as a function off height at 1 kW.....	3-16
Figure 3-26	PWR Cell 1 PCT as a function of time at 1 kW.....	3-17
Figure 3-27	PWR Cell 1 mass flow rate as a function of time at 1 kW.....	3-17
Figure 3-28	PWR 1x4 configuration—steady-state center assembly PCT as a function of height at 1 kW.....	3-19
Figure 3-29	PWR 1x4 configuration—steady-state peripheral assembly PCT as a function of height at 1 kW.....	3-19
Figure 3-30	PWR 1x4 configuration—steady-state outer pool cell wall maximum temperature as a function of height at 1 kW.....	3-20
Figure 3-31	PWR 1x4 configuration—steady-state exterior wall maximum temperature as a function of height at 1 kW.....	3-20
Figure 3-32	PWR 1x4 configuration—PCT location in peripheral assembly.....	3-21
Figure 3-33	PWR 1x4 configuration—center assembly PCT as a function of time at 1 kW.....	3-22
Figure 3-34	PWR 1x4 configuration—center assembly mass flow rate as a function of time at 1 kW.....	3-22
Figure 3-35	PWR 1x4 configuration—peripheral assembly PCT as a function of time at 1 kW.....	3-23
Figure 3-36	PWR 1x4 configuration—peripheral assembly mass flow rate as a function of time at 1 kW.....	3-23
Figure 3-37	PWR 1x4 configuration—exterior wall maximum temperature as a function of time at 1 kW.....	3-24
Figure 3-38	PWR 1x4 configuration—center assembly PCT as a function of height at 1 kW at 24 hours.....	3-25
Figure 3-39	PWR 1x4 configuration—peripheral assembly PCT as a function of height at 1 kW at 24 hours.....	3-25
Figure 3-40	PWR 1x4 configuration—exterior wall maximum temperature as a function of height at 1 kW at 24 hours.....	3-26
Figure 3-41	BWR steady-state PCT as a function of height at 1,369 W.....	3-27
Figure 3-42	BWR steady-state pool cell wall maximum temperature as a function of height at 1,369 W.....	3-27
Figure 3-43	BWR steady-state exterior wall maximum temperature as a function of height at 1,369 W.....	3-28
Figure 3-44	BWR PCT as a function of time at 1,369 W.....	3-28
Figure 3-45	BWR inlet bundle mass flow rate as a function of time at 1,369 W.....	3-29
Figure 3-46	BWR inlet drain mass flow rate as a function of time at 1,369 W.....	3-29
Figure 3-47	BWR pool cell wall maximum temperature as a function of time at 1,369 W.....	3-30
Figure 3-48	BWR exterior wall maximum temperature as a function of time at 1,369 W.....	3-30
Figure 3-49	BWR PCT as a function of height at 1,369 W at 12 hours.....	3-31
Figure 3-50	BWR pool cell wall maximum temperature as a function of height at 1,369 W at 12 hours.....	3-31
Figure 3-51	BWR exterior wall maximum temperature as a function of height at 1,369 W at 12 hours.....	3-32
Figure 3-52	BWR steady-state PCT as a function of height at 2,236 W.....	3-33

Figure 3-53	BWR steady-state pool cell wall maximum temperature as a function of height at 2,236 W.....	3-33
Figure 3-54	BWR steady-state exterior wall maximum temperature as a function of height at 2,236 W.....	3-34

LIST OF TABLES

Table 1-1	Summary of Assembly Hydraulic Characteristics for Storage Cell 1 and Cell 2.....	1-1
Table 1-2	Hydraulic Dimensions for the Center Assembly, Average Peripheral Assembly, and the Cross-Flow Path	1-4
Table 1-3	Dimensions of Assembly Components in the 9x9 BWR.....	1-4
Table 2-1	Detailed PWR Assemblies—Materials	2-4
Table 2-2	Detailed BWR Assembly—Materials	2-4
Table 2-3	Density of Materials	2-4
Table 2-4	Heat Capacity of Air	2-5
Table 2-5	Thermal Conductivity of Air	2-5
Table 2-6	Viscosity of Air	2-5
Table 2-7	Heat Capacity of Zircaloy-2	2-5
Table 2-8	Thermal Conductivity of Zircaloy-2	2-5
Table 2-9	Heat Capacity of Steel.....	2-6
Table 2-10	Thermal Conductivity of Steel	2-6
Table 2-11	Heat Capacity of the Surrogate Fuel in the Heated Assembly	2-6
Table 2-12	Thermal Conductivity of the Surrogate Fuel in the Heated Assembly	2-6
Table 2-13	Heat Capacity of the Surrogate Fuel in the Unheated Assemblies	2-7
Table 2-14	Thermal Conductivity of the Surrogate Fuel in the Unheated Assemblies	2-7
Table 2-15	Heat Capacity of Aluminum.....	2-7
Table 2-16	Thermal Conductivity of Aluminum.....	2-7
Table 2-17	Heat Capacity of Incoloy	2-7
Table 2-18	Thermal Conductivity of Incoloy	2-8
Table 2-19	Heat Capacity of Kaowool	2-8
Table 2-20	Thermal Conductivity of Kaowool.....	2-8
Table 2-21	Predicted and TRW Radial k_{eff} Comparison	2-10
Table 2-22	PWR Cell 1 Porous Model—Radial k_{eff}	2-11
Table 2-23	PWR Cell 1 Porous Model—Axial k_{eff}	2-11
Table 2-24	PWR Cell 2 Porous Model—Radial k_{eff}	2-11
Table 2-25	PWR Cell 2 Porous Model—Axial k_{eff}	2-11
Table 2-26	1x4 PWR Center Assembly Porous Model—Radial k_{eff}	2-12
Table 2-27	1x4 PWR Center Assembly Porous Model—Axial k_{eff}	2-12
Table 2-28	1x4 PWR Peripheral Assembly Porous Model—Radial k_{eff}	2-12
Table 2-29	1x4 PWR Peripheral Assembly Porous Model—Axial k_{eff}	2-12
Table 2-30	BWR Fully Populated Cladding Region Porous Model—Radial k_{eff}	2-12
Table 2-31	BWR Fully Populated Cladding Region Porous Model—Axial k_{eff}	2-13
Table 2-32	BWR Partially Populated Cladding Region Porous Model—Radial k_{eff}	2-13
Table 2-33	BWR Partially Populated Cladding Region Porous Model—Axial k_{eff}	2-13
Table 2-34	Equivalent Porous Model Density	2-14
Table 2-35	PWR Cell 1 Porous Model—Heat Capacity	2-14
Table 2-36	PWR Cell 2 Porous Model—Heat Capacity	2-14
Table 2-37	1x4 PWR Center Porous Model—Heat Capacity	2-15
Table 2-38	1x4 PWR Peripheral Assembly Porous Model—Heat Capacity.....	2-15
Table 2-39	BWR Fully Populated Cladding Region Porous Model—Heat Capacity	2-15
Table 2-40	BWR Partially Populated Cladding Region Porous Model—Heat Capacity	2-15
Table 2-41	Friction Coefficient—PWR Assemblies	2-16
Table 2-42	Friction Coefficient—BWR Assemblies	2-16
Table 3-1	PWR Single Assembly Cell 2—Models.....	3-1
Table 3-2	PWR Cell 2 Steady-State Summary Results at 1 kW	3-3

Table 3-3	PWR Cell 2 Steady-State Convected Heat and Heat Transfer Coefficient at 1 kW.....	3-3
Table 3-4	PWR Single Assembly Cell 2—PCT and Mass Flow rate at 1 kW at 20 Hours	3-7
Table 3-5	PWR Single Assembly Cell 2 (Thermal Mass)—PCT and Mass Flow rate at 1 kW at 20 hours.....	3-11
Table 3-6	PWR Cell 2 Steady-State Mass Flow Rate at 0.5 kW	3-14
Table 3-7	PWR Single Assemble Cell 1—Models.....	3-15
Table 3-8	PWR Cell 1 Steady-State Mass Flow Rate at 1 kW	3-16
Table 3-9	PWR 1x4 Configuration—Models.....	3-18
Table 3-10	PWR 1x4 Configuration—Steady-State Mass Flow Rate at 1 kW	3-18
Table 3-11	PWR 1x4 Configuration—PCT and Mass Flow Rate at 1 kW at 24 Hours	3-24
Table 3-12	BWR Single Assembly—Models	3-26
Table 3-13	BWR Steady-State Mass Flow Rate at 1,369 W	3-27
Table 3-14	WR Single Assembly—PCT and Mass Flow Rate at 1,369 W at 12 Hours	3-31
Table 3-15	BWR Steady-State Mass Flow Rate at 2,236 W	3-32
Table 4-1	Total Number of Cells for Different Grid Levels.....	4-2
Table 4-2	Combinations	4-3
Table 4-3	Mesh Level Ratios.....	4-3
Table 4-4	Computed Maximum Temperature.....	4-3
Table 4-5	PCT—GCI for Calculated Order of Accuracy	4-3
Table 4-6	PCT—GCI for Formal Order of Accuracy	4-3
Table 4-7	Computed Mass Flow Rate.....	4-4
Table 4-8	Mass Flow Rate—GCI for Calculated Order of Accuracy	4-4
Table 4-9	Mass Flow Rate—GCI for Formal Order of Accuracy	4-4

EXECUTIVE SUMMARY

Computational fluid dynamics (CFD) technologies are rapidly expanding, with a large database of proven capabilities. The driving force for program development generally is not the nuclear community, as it was for the classical thermal-hydraulic system codes. Nevertheless, many applications overlap with those associated with the nuclear industry, and in particular, dry cask applications: flows in complex geometries, mixing in stratified fluids, flow separation and reattachment, turbulence, multiphase phenomena, chemical species interaction, and combustion. Consequently, practitioners in areas related to dry cask applications can benefit from advancements in the technology taking place elsewhere. However, because of the complexity of modern commercial CFD packages, careful input preparation and solution of model equations are essential to avoiding errors.

In 2003, the U.S. Nuclear Regulatory Commission (NRC) undertook an experimental program to address thermal-hydraulic conditions and zirconium fire propagation during a complete loss of coolant event in a boiling-water reactor (BWR) spent fuel pool. The accident conditions of interest for the spent fuel pool were simulated in a full-scale prototypic fashion (electrically heated, prototypic BWR 9x9 assemblies in a prototypic spent fuel pool rack) so that the results closely represented actual fuel assembly responses. These experiments are summarized in NUREG/CR-7143, “Characterization of Thermal-Hydraulic and Ignition Phenomena in Prototypic, Full-Length Boiling Water Reactor Spent Fuel Pool Assemblies After a Postulated Complete Loss-of-Coolant Accident,” issued March 2013.

Similarly, in 2009, the NRC, in collaboration with the Organisation for Economic Co-operation and Development/Nuclear Energy Agency (OECD/NEA) and 12 international partners signed an agreement called the “OECD/NEA Sandia Fuel Project—An Experimental Programme and Related Analyses for the Characterization of Hydraulic and Ignition Phenomena of Prototypic Water Reactor Fuel Assemblies.” This program defined an experimental test matrix, experimental conditions, and the parameters to be examined. The overall objective was to perform a highly detailed thermal-hydraulic characterization of a full-length pressurized-water reactor (PWR; 17x17) commercial fuel assembly mockup to provide data for the direct validation of severe accident computer codes. These experiments are summarized in NUREG/CR-7215, “Spent Fuel Pool Project Phase 1: Pre-Ignition and Ignition Testing of a Single Commercial 17x17 Pressurized Water Reactor Spent Fuel Assembly under Complete Loss of Coolant Accident Conditions,” issued April 2016, and NUREG/CR-7216, “Spent Fuel Pool Project Phase II: Pre-Ignition and Ignition Testing of a 1x4 Commercial 17x17 Pressurized Water Reactor Spent Fuel Assemblies under Complete Loss of Coolant Accident Conditions,” issued April 2016.

The experiments for both the BWR and the PWR assemblies were conducted in two phases: Phase I focused on a single, heated assembly and Phase II consisted of a single, heated assembly surrounded by four unheated assemblies representing a 1x4 loading pattern.

Both phases included separate effect tests (i.e., preignition tests) and integral effects tests (i.e., ignition tests). The experiments in the separate effect tests were designed to investigate heat transfer and flow phenomena (i.e., naturally induced mass flow). The temperature values reached in these tests were below the ignition point of the cladding. As such, these tests were nondestructive. The experiments in the integral effects tests were conducted to reach the onset of cladding fire. As such, these tests led to the destruction of the assemblies. Both phases were conducted using a uniform axial power profile with electrically heated rods at multiple decay powers.

This NUREG summarizes the efforts to validate the ANSYS FLUENT code using experimental data collected in the separate effects tests. The data of interest for these nondestructive tests were measured temperatures throughout the fuel assembly and induced mass flow rate. Detailed and porous CFD models were created for each assembly configuration including a single, heated full-length 17x17 PWR fuel bundle; a single, heated 17x17 PWR assembly surrounded by four unheated similar assemblies in a 1x4 loading pattern; and, a single, heated full-length 9x9 BWR fuel bundle.

Steady-state and transient simulations were performed at different decay power values. Peak cladding temperature, exterior wall temperature, and mass flow rate from CFD predictions were compared to the experimental data.

The CFD results and experimental data for PCT and air mass flow rate agreed favorably within the calculated experimental and CFD numerical uncertainties range. The results demonstrate that ANSYS Fluent modeling can be used to demonstrate the safety of dry cask storage and transportation.

ABBREVIATIONS

2D	two dimensional
BWR	boiling-water reactor
CFD	computational fluid dynamics
CFR	<i>Code of Federal Regulations</i>
D_H	hydraulic diameter
ft	foot/feet
GCI	grid convergence index
ID	inner dimension
in.	inch(es)
J	joule(s)
K	Kelvin
k_{eff}	effective thermal conductivity
kg	kilogram(s)
kW	kilowatt(s)
m	meter(s)
MgO	magnesium oxide
mm	millimeter(s)
NRC	U.S. Nuclear Regulatory Commission
OD	outer dimension
OECD/NEA	Organisation for Economic Co-operation and Development/Nuclear Energy Agency
PCT	peak cladding temperature
PWR	pressurized-water reactor
TRW	TRW Environmental Safety Systems, Inc.
U.S.	United States
V&V	verification and validation
W	watt(s)

1 INTRODUCTION

1.1 Pressurized-Water Reactor Single Assembly

The testing in Phase I of the Spent Fuel Pool Project focused on axial heating and burn propagation. The near-prototypic test assembly was constructed to represent a commercial 17x17 pressurized-water reactor (PWR) fuel bundle. Figure 1-1 illustrates the various components comprising a typical 17x17 PWR assembly. The main structural component of the assembly is the core skeleton, which consists of 11 spacers permanently attached to 25 guide tubes. The 264 fuel rods pass through the spacers and are held captive in the assembly by the top and bottom nozzles.

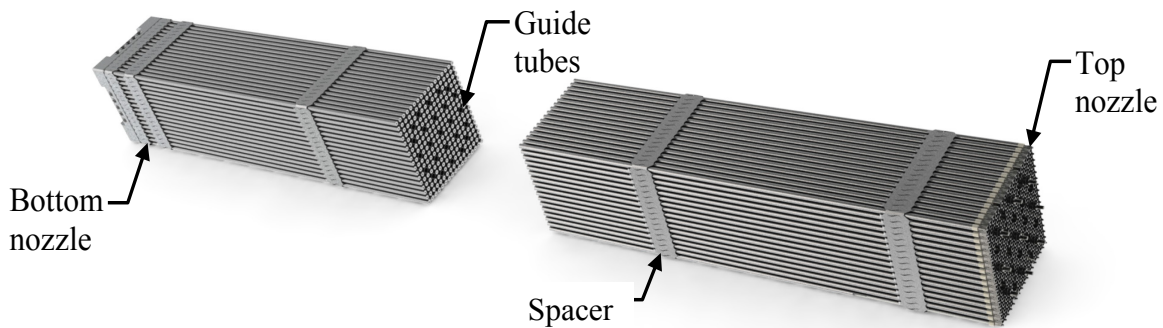


Figure 1-1 Various components in a typical 17x17 PWR fuel assembly

The single full-length, electrically heated PWR assembly was fabricated using prototypic, commercial 17x17 PWR components and 9.50-millimeter (mm) (0.374-inch (in.)) heater rods made from 11.18-mm (0.44-in.) Zircaloy-2 tubing. The as-built heater rod diameter of 9.50 mm (0.374 in.) is slightly smaller than the typical PWR design value of 9.53 mm (0.375 in.) but is not expected to significantly affect system hydraulics.

The tests were performed using a uniform power profile with electrically heated rods. A 0.1524-meter (m) (6-in.) layer of Kaowool insulation was installed around the pool cell and then wrapped with a 0.9 mm (0.036 in.) thick sheet of stainless steel.

During the tests, the assembly cooled by natural circulation, and the pressure and air inlet temperature maintained the local ambient conditions.

The tests were performed for two storage pool cell sizes. Table 1-1 presents a summary of the hydraulic characteristics of the cells.

Table 1-1 Summary of Assembly Hydraulic Characteristics for Storage Cell 1 and Cell 2

Description	Cell 1	Cell 2
Inner Dimension (mm/in)	221.3/8.71	223.4/8.80
Flow Area (m ² /in ²)	0.0273/4.2e-5	0.0283/4.4e-5
Hydraulic diameter, D _H (mm/in)	11.2/0.441	11.6/0.457

NUREG-7215, "Spent Fuel Project Phase I: Pre-Ignition and Ignition Testing of a Single Commercial 17x17 Pressurized Water Reactor Spent Fuel Assembly under Complete Loss of Coolant Accident Conditions," issued April 2016, contains further details of the test conditions, such as thermocouple and hot wire anemometer layout.

1.2 Pressurized-Water Reactor 1x4 Assembly Configuration

The testing in Phase II of the Spent Fuel Pool Project focused on axial and transverse heating propagation from the center to the peripheral bundles of the full-length assemblies with the same components as used for Phase I. The fuel assemblies were arranged in a pool rack with the heated assembly in the center pool cell as shown in Figure 1-2. The four unheated peripheral fuel assemblies shared a cell wall with the center assembly, representing older spent fuel. All mock fuel assemblies were constructed with zirconium alloy cladding and prototypic structural components. The center assembly was constructed with electrically resistive heaters. The thermal mass of the compacted magnesium oxide (MgO) powder used to make the electric heater matched the prototypic uranium oxide spent fuel as demonstrated in the boiling-water reactor (BWR) study (NUREG/CR-7143, "Characterization of Thermal-Hydraulic and Ignition Phenomena in Prototypic, Full-Length Boiling Water Reactor Spent Fuel Pool Assemblies After a Postulated Complete Loss-of-Coolant Accident," issued March 2013). The peripheral assemblies were loaded with MgO pellets in order to closely match the thermal mass of spent fuel. A series of preignition tests were conducted to build a database of the thermal-hydraulic response of fuel below ignition temperatures.

The main structural component of the assembly is the core skeleton, which consists of 11 spacers permanently attached to 25 guide tubes. The 264 fuel rods pass through the spacers and are held captive in the assembly by the top and bottom nozzles.

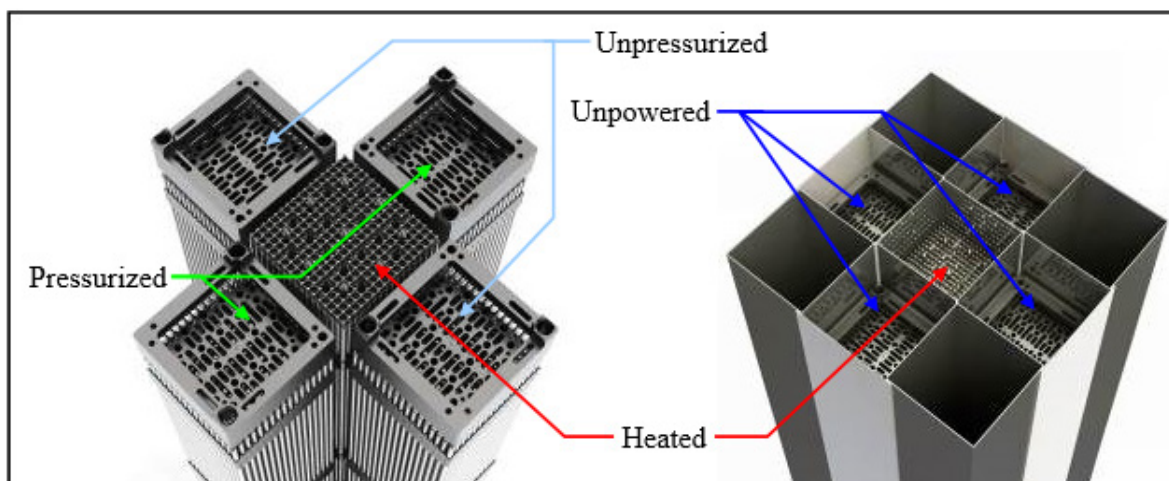


Figure 1-2 Layout of the Phase II test assembly

The four peripheral PWR assemblies were fabricated using prototypic, commercial 17x17 PWR components including a skeleton, top and bottom nozzles, 9.50-mm (0.374-in.) outer dimension by 0.57-mm (0.0225-in.) wall tubing, top and bottom end plugs, and plenum springs. The center heated PWR assembly was fabricated using prototypic, commercial 17x17 PWR components and 9.53-mm (0.375-in.) outer dimension heater rods made from 11.18-mm (0.44-in.) zirconium alloy tubing supplied by an industrial vendor. The wall thickness of the Zircaloy-2 cladding measured

approximately 0.71 mm (0.028 in.) and was relatively unchanged by the heater fabrication process. The spent fuel rod simulators for Phase II had a linear power profile and a maximum output of 31.1 watts (W)/m (9.5 W/foot (ft)), which was twice that expected to produce ignition.

The pool rack for the 17x17 PWR fuel assemblies incorporates pool cells with an inner dimension of 224.5 mm (8.84 in.). As with the Phase I pool cells, the Phase II pool rack was constructed of 1.91-mm (0.075-in.)-thick stainless steel material. Figure 1-3 shows the actual inner dimensions of each of the pool cells. The inner dimension of the center cell used in this experiment was 224.2 mm (8.83 in.), which is nearly identical to the 224.5-mm (8.84-in.) inner dimension of the pool rack. The as-built peripheral cells are slightly smaller than the design, with an average inner dimension of 222.7 mm (8.77 in.), or less than a 1 percent difference. Figure 1-3 also shows the insulation scheme for Phase II. The corner cells were filled with high-temperature insulation. The entire assembly was surrounded by approximately 152.4 mm (6 in.) of the same high-temperature insulation. A stainless steel thermal radiation barrier was installed around the external insulation. Table 1-2 summarizes the hydraulic characteristics.

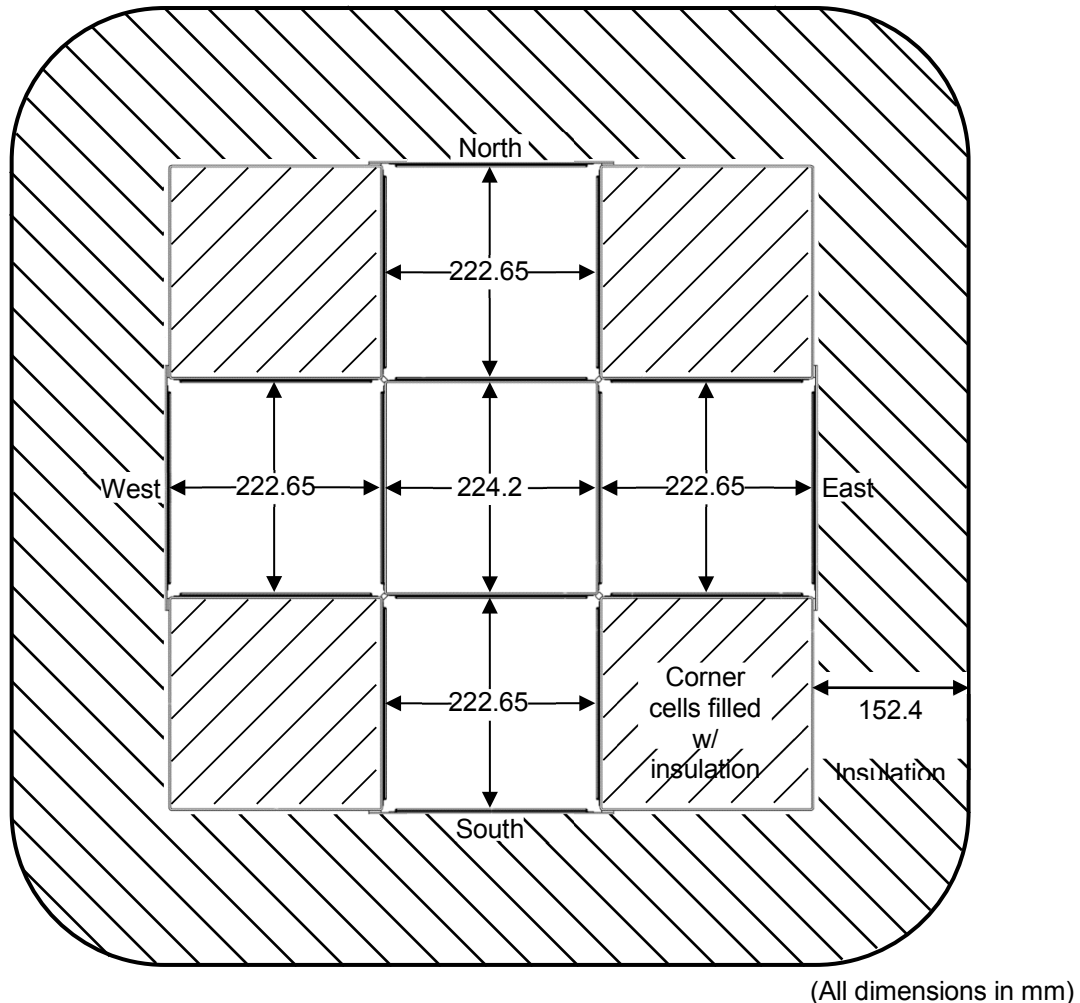


Figure 1-3 Dimensions of the as-built pool rack and the design insulation thickness

Table 1-2 Hydraulic Dimensions for the Center Assembly, Average Peripheral Assembly, and the Cross-Flow Path

Description	Center	Peripheral	Cross-Flow Path
Inner Dimension (mm/in.)	224.2/8.83	222.65/8.77	8.7/0.34
Flow Area (m ² /in. ²)	0.0287/44.49	0.0283/43.87	5.89E-5/0.0913
Hydraulic diameter, D _H (mm/in.)	11.7/0.46	11.6/0.46	8.7/0.34

NUREG/CR-7216, “Spent Fuel Project Phase II: Pre-Ignition and Ignition Testing of a 1x4 Commercial 17x17 Pressurized Water Reactor Spent Fuel Assemblies under Complete Loss of Coolant Accident Conditions,” issued April 2016, has further details about the instrumentation, including the hot wire anemometers, oxygen sensors, residual gas analyzer, strain gauges, and thermocouples.

1.3 Boiling-Water Reactor Single Assembly

The prototypic 9x9 BWR assembly includes the top and bottom tie plates, spacers, water rods, channel box, and all related assembly hardware. Incoloy heater rods were substituted for the fuel rod pins for heated testing. The diameter of the Incoloy heaters was slightly smaller than that of the prototypic pins, 1.09×10^{-2} m versus 1.12×10^{-2} m. Table 1-3 lists the dimensions of the assembly components.

Table 1-3 Dimensions of Assembly Components in the 9x9 BWR

Description	Lower (Fully Populated) Section	Upper (Partially Populated) Section
Number of Pins	74	66
Pin Diameter (m)	1.09×10^{-2}	1.09×10^{-2}
Pin Pitch (m)	1.44×10^{-2}	1.44×10^{-2}
Pin Separation (m)	3.48×10^{-3}	3.48×10^{-3}
Water Rod OD (main section) (m)	2.49×10^{-2}	2.49×10^{-2}
Water Rod ID (m)	2.34×10^{-2}	2.34×10^{-2}
Storage Cell Dimension D _{cell} (mm)	132.6	132.6
Flow Area, A _{Assembly} (m ²)	0.0098	0.0106
D _{H, Ref.} (m)	0.0119	0.0141

A stainless steel enclosure housed the entire fuel assembly, simulating the rack walls of a spent fuel pool. This enclosure was then insulated with 0.15 m (6 in.) of Fiberfrax Durablanket® type S insulation. Two radiation barriers, consisting of stainless steel shim stock, were placed at 0.075-m (3-in.) intervals, as shown in Figure 1-4.

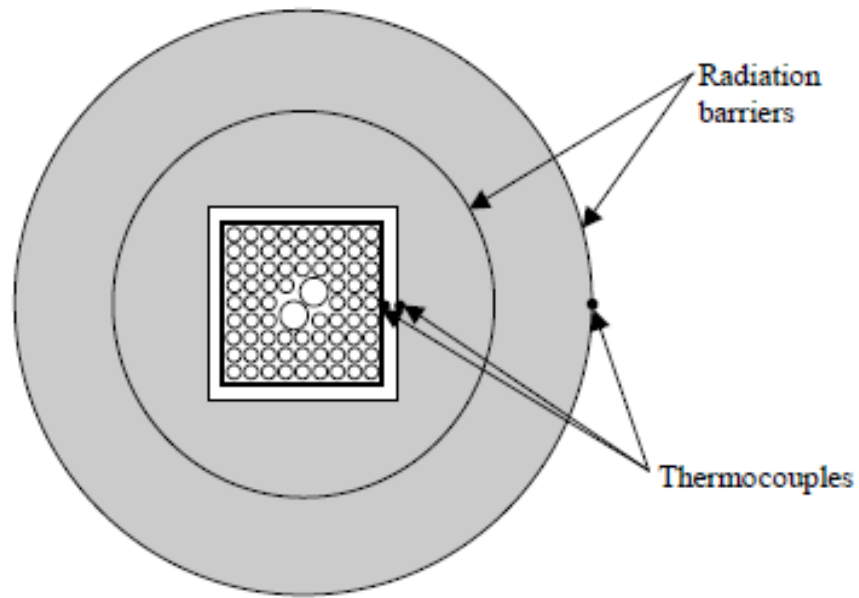


Figure 1-4 Arrangement of insulation, radiation barriers, and external thermocouples

Data using closed bypass and open drain holes were used for the validation effort. Bypass holes are part the BWR 9x9 configuration. The drain holes simulate the flow from the plenum and other assemblies. Figure 1-5 shows the drain holes at the bottom side of the BWR single assembly.

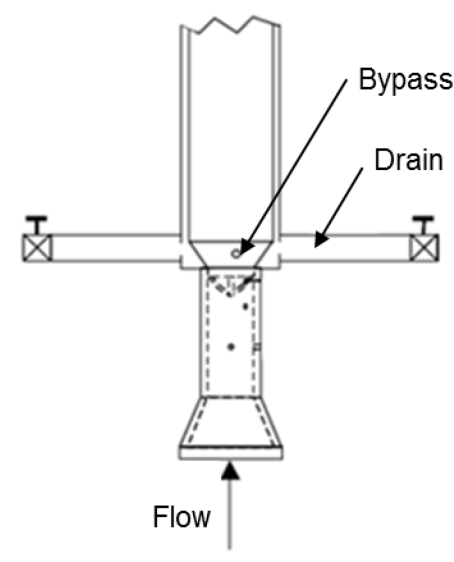


Figure 1-5 Arrangement of drain holes

NUREG/CR-7143 contains more details about the instrumentation.

The 1x4 BWR experimental setup consisted of five shortened assemblies, recreating the top 1.22-m (4-ft.) section. For this testing, airflow rates and inlet temperature were controlled for the center and peripheral assemblies. The mass flow was not naturally induced (i.e., forced flow) in

the assemblies, which is not prototypical for dry cask applications. Therefore, this validation effort did not include this part of the experiment.

1.4 Computational Fluid Dynamics Model

Detailed and porous media simulations were performed for each of the aforementioned preignition tests using ANSYS FLUENT. As an example, Figure 1-6 shows a cross section of the CFD PWR single assembly detailed and porous models. Both models used 1/8th symmetry boundary conditions to reduce the modeling efforts.

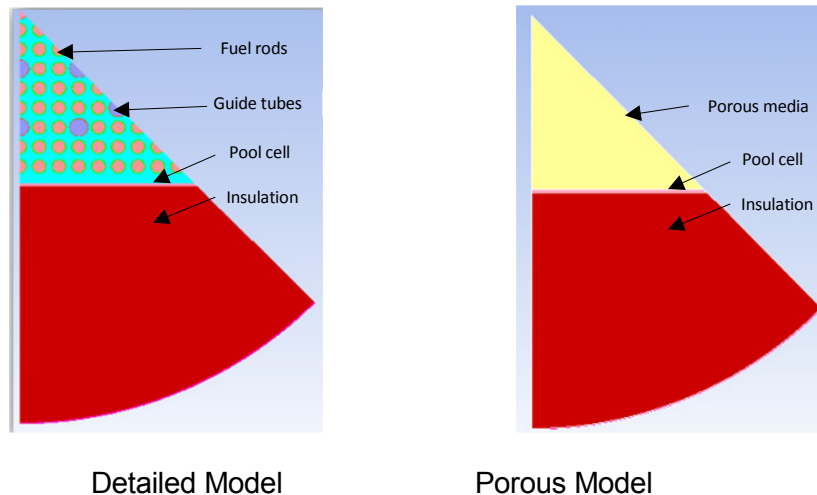


Figure 1-6 CFD PWR single assembly cross sections of the detailed and porous models

The PWR and BWR detailed models explicitly represent each component of the assemblies, including fuel rods, cladding, guide tubes, grid spacers, neutron absorbers in the peripheral assemblies, and bottom and top nozzles. The porous media model in the PWR assemblies was representative of the fuel, cladding, fluid within the pool cell, grid spacers and guide tubes. In the BWR assemblies, the porous media represented the fuel, cladding, water rods, and the flow within the channel box and grid spacers. Use of porous media involves representing the absence of these components with an equivalent frictional and inertial hydraulic loss, equivalent thermal conductivity, equivalent density, and equivalent heat capacity.

FLUENT, Version 16, was used for the validation in this NUREG.

2 COMPUTATIONAL FLUID DYNAMICS MODELING

2.1 Detailed Model

Geometry and mesh models were generated for a single PWR assembly, single BWR assembly, and 1x4 PWR configuration. The model's boundary conditions represented the existing conditions during the experiment. Figure 2-1 through Figure 2-6 show a schematic of the boundary conditions applied to the detailed models. The model used a pressure inlet boundary at the entry of the assembly (shown in blue), pressure outlet at the exit (shown in red) and applied a volumetric heat source in the volume occupied by MgO powder. The flow regime through the assembly was modeled as laminar, as the corresponding Reynolds number based on the hydraulic diameter was below 200. The model used an operating pressure of 84,000 Pa, which corresponded to the altitude of the location of the experiment. To reduce the extent of the analyzed control volume, the model considered symmetry. As such, the PWR assemblies for the Phase 1 and Phase 2 simulations used 1/8th symmetry (shown in the figures in yellow), and the BWR single assembly simulation used 1/4th symmetry. In the BWR assembly, the drain holes were modeled by adding an inlet at the bottom of the assembly, as shown in Figure 2-4, using an inlet vent boundary condition (shown in blue) with a loss coefficient of 0.42 to represent minor losses from the experimental drain holes arrangement shown in Figure 1-5.

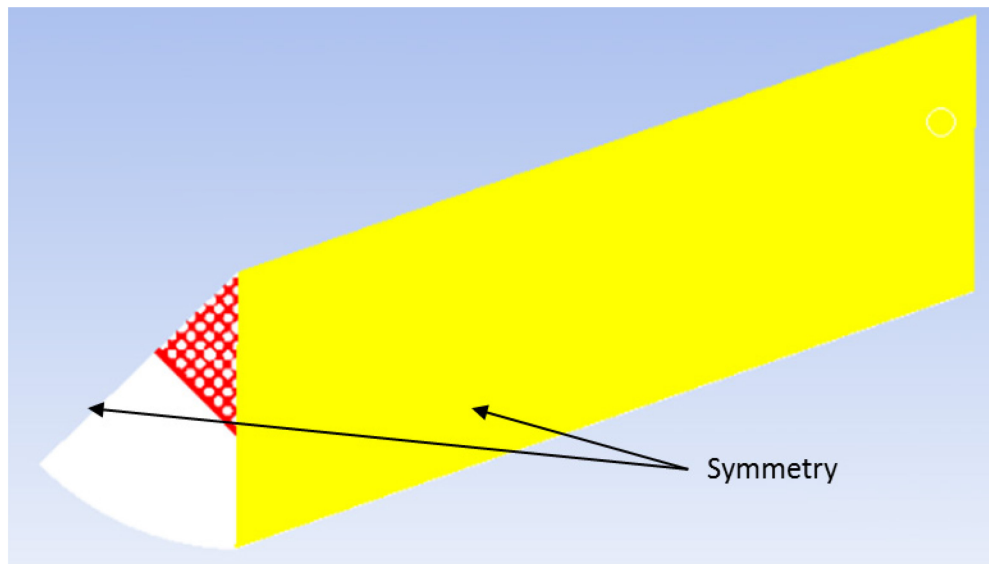


Figure 2-1 Detailed PWR single assembly (Cell 2 illustrated)—boundary conditions

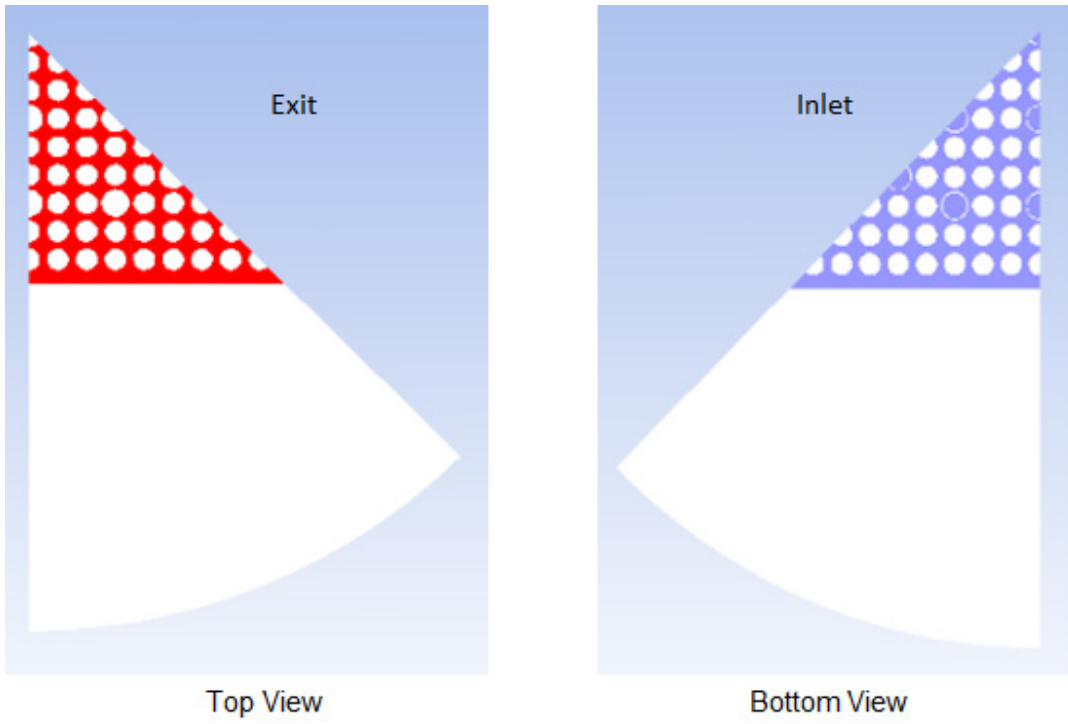


Figure 2-2 Detailed PWR single assembly top and bottom views (Cell 2 illustrated)—boundary conditions

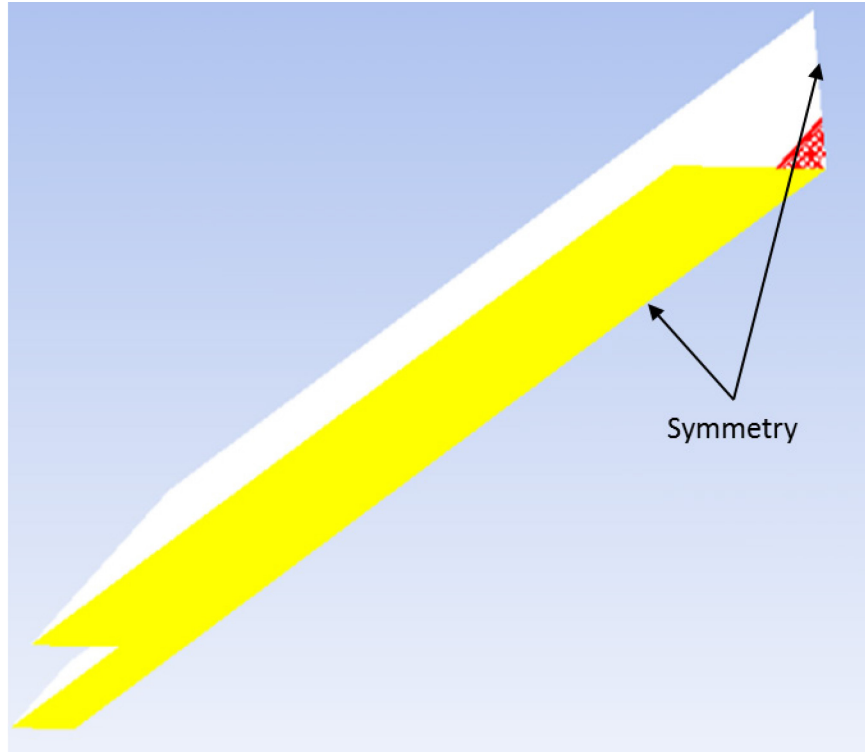


Figure 2-3 Detailed BWR single assembly—boundary conditions (1/4 symmetry)

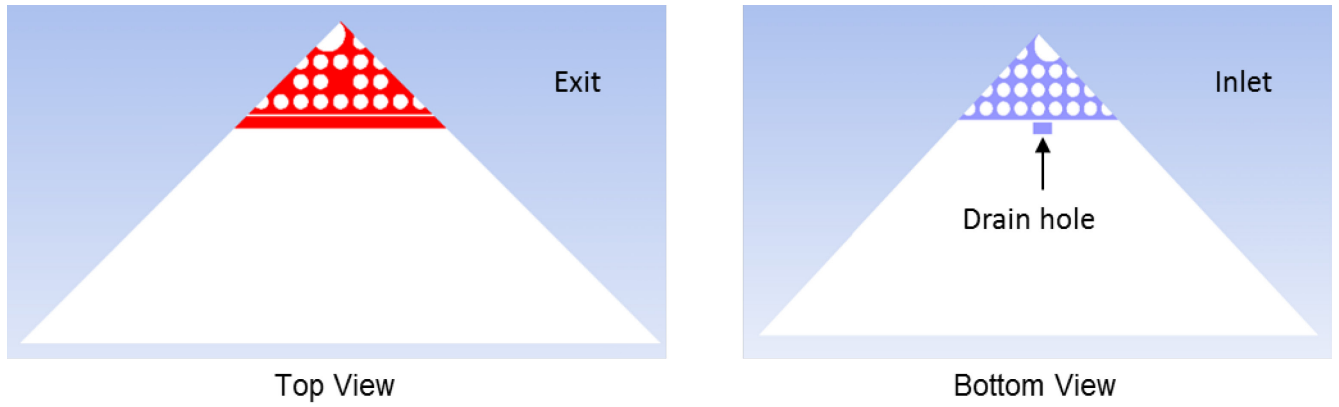


Figure 2-4 Detailed BWR single assembly top and bottom views—boundary conditions

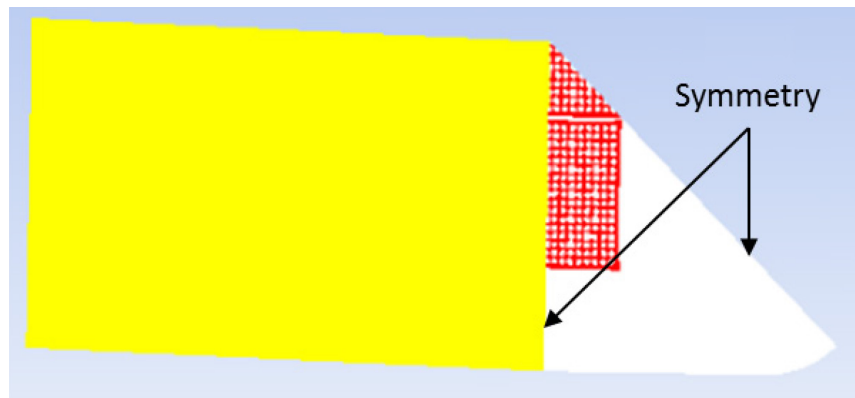


Figure 2-5 Detailed PWR 1x4 configuration—boundary conditions

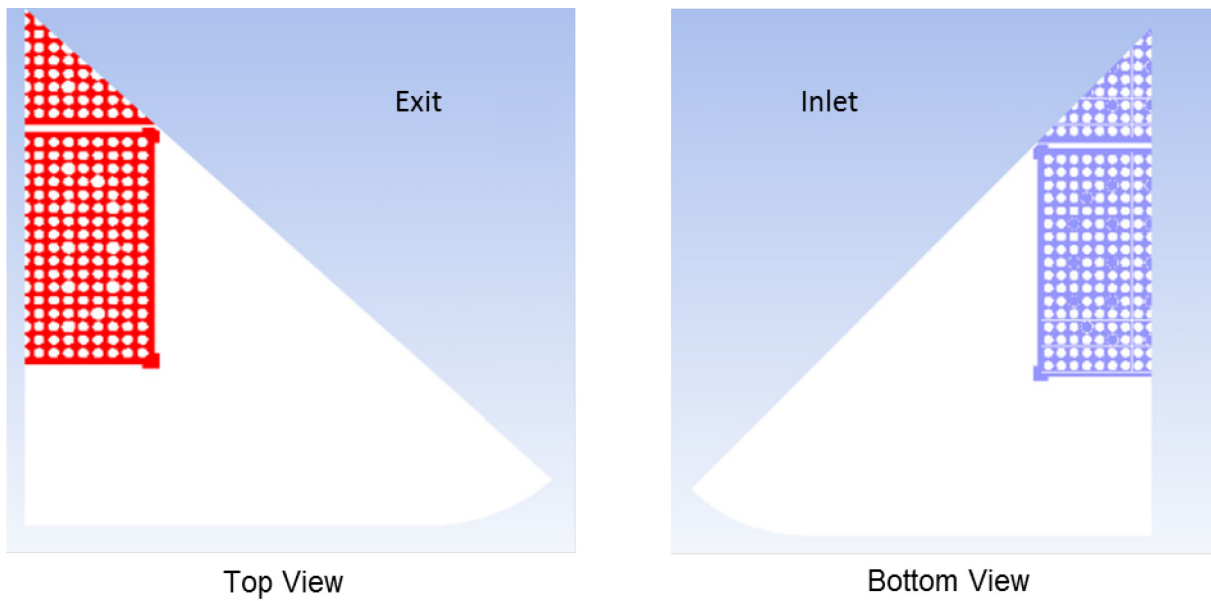


Figure 2-6 Detailed PWR 1x4 configuration top and bottom views—boundary conditions

Table 2-1 and Table 2-2 summarize the materials of each component in the assembly. Table 2-3 shows the material densities with the exception of air, which was modeled as an ideal gas. All other physical properties for the materials used were implemented as function of temperature, as seen in Table 2-4 through Table 2-20.

Table 2-1 Detailed PWR Assemblies—Materials

Component	Material
Surrogate Fuel (heated assembly)	Magnesium Oxide Powder and Nichrome
Surrogate Fuel (unheated assembly)	Magnesium Oxide Pellets
Cladding	Zircaloy-2
Guide Tubes	Zircaloy-2
Fluid	Air
Grid Spacers	Zircaloy-2
Insulation	Kaowool
Cell Wall	Steel
Exterior Wall	Steel
Neutron Absorber	Aluminum

Table 2-2 Detailed BWR Assembly—Materials

Component	Material
Surrogate Fuel	Magnesium Oxide Powder and Nichrome
Cladding	Incoloy
Water Rod	Zircaloy-2
Fluid	Air
Grid Spacers	Zircaloy-2
Insulation	Kaowool
Channel Box	Zircaloy-2
Cell Wall	Steel
Exterior Wall	Steel

Table 2-3 Density of Materials

Material	Density (kg/m³)
Zirconium	6,500
Steel	8,030
Magnesium Oxide powder and Nichrome	2,913
Magnesium Oxide Pellets	2,720
Aluminum	2,702
Inconel	8,000
Kaowool	96

Table 2-4 Heat Capacity of Air

Temperature (K)	c_p (J/kg-K)
250	1,007
500	1,030
800	1,091
1,000	1,141
1,600	1,248

Table 2-5 Thermal Conductivity of Air

Temperature (K)	k (W/m-K)
250	0.0223
500	0.0373
800	0.0573
1,000	0.0667
1,600	0.106

Table 2-6 Viscosity of Air

Temperature (K)	μ (kg/m-s)
250	1.6E-5
500	2.7E-5
800	3.7E-5
1,000	4.24E-5
1,600	5.84E-5

Table 2-7 Heat Capacity of Zircaloy-2

Temperature (K)	c_p (J/kg-K)
273	275
400	302
640	331
1,090	375
1,093	505

Table 2-8 Thermal Conductivity of Zircaloy-2

Temperature (K)	k (W/m-K)
273	12.1
473	14.5
673	17
873	19.9
1,073	23.1

Table 2-9 Heat Capacity of Steel

Temperature (K)	c_p (J/kg-K)
200	402
400	526
600	554
800	581
1,000	608
1,200	640
1,500	682

Table 2-10 Thermal Conductivity of Steel

Temperature (K)	k (W/m-K)
273	16
398	17
498	19
800	22.6
1,000	25.4
1,200	28
1,500	31.7

Table 2-11 Heat Capacity of the Surrogate Fuel in the Heated Assembly

Temperature (K)	c_p (J/kg-K)
273	848
400	100
600	1,111
800	1,167
1,000	1,209
1,145	1,228

Table 2-12 Thermal Conductivity of the Surrogate Fuel in the Heated Assembly

Temperature (K)	k (W/m-K)
273	400
400	12.8
600	15.3
800	17.6
1,000	19.7
1,100	20.6

Table 2-13 Heat Capacity of the Surrogate Fuel in the Unheated Assemblies

Temperature (K)	c_p (J/kg-K)
273	892.4
400	1,058
600	1,176
800	1,234
1,000	1,272

Table 2-14 Thermal Conductivity of the Surrogate Fuel in the Unheated Assemblies

Temperature (K)	k (W/m-K)
273	1.73
400	1.88
600	2.06
800	2.2
1,000	2.28
1,100	2.3

Table 2-15 Heat Capacity of Aluminum

Temperature (K)	c_p (J/kg-K)
100	482
200	798
400	949
600	1,033
800	1,146

Table 2-16 Thermal Conductivity of Aluminum

Temperature (K)	k (W/m-K)
100	302
200	237
400	240
600	231
800	218

Table 2-17 Heat Capacity of Incoloy

Temperature (K)	c_p (J/kg-K)
298	428
473	435
673	450
873	469
1,073	488

Table 2-18 Thermal Conductivity of Incoloy

Temperature (K)	k (W/m-K)
298	11.5
473	14.3
673	17.4
873	20.6
1,073	23.8

Table 2-19 Heat Capacity of Kaowool

Temperature (K)	c _p (J/kg-K)
273	788
473	862
673	928
873	985
1,073	1,030
1,273	1,090
1,473	1,100

Table 2-20 Thermal Conductivity of Kaowool

Temperature (K)	k (W/m-K)
273	0.0208
473	0.0502
673	0.088
873	0.134
1,073	0.188
1,273	0.251
1,473	0.322

2.2 Porous Model

All dry cask applicants favor the use of the porous model, or media method, since it simplifies the configuration and saves on processing time. As such, the porous media method was chosen for validation to test its robustness and predictive capabilities. The use of this model involves input to make up for the simplifications made in the geometry. Simplifications, such as fuel rods, grid spacers, and any assembly's intricacies, are replaced by a volume filled with porous media with an equivalent flow resistance. Additionally, the combination of radiation and conduction heat transfer within that volume is represented by an effective thermal conductivity (k_{eff}). To accomplish this task, a two-dimensional (2D) model representing the detailed cross section of an assembly explicitly showing fuel rods was used (as shown in Figure 2-7) to obtain k_{eff} for different temperature boundary conditions. The TRW Environmental Safety Systems, Inc. (TRW) report, "Spent Nuclear Fuel Effective Thermal Conductivity," dated July 11, 1996, describes the k_{eff} approach in detail.

Figure 2-7 shows the CFD 2D model with 1/8th symmetry used to calculate the radial effective thermal conductivity for the PWR cell 1 single assembly configuration. The model shows all the

components in the assembly including fuel, cladding, guide tubes, and cell wall. This model used symmetry as well as constant wall temperature as boundary conditions.

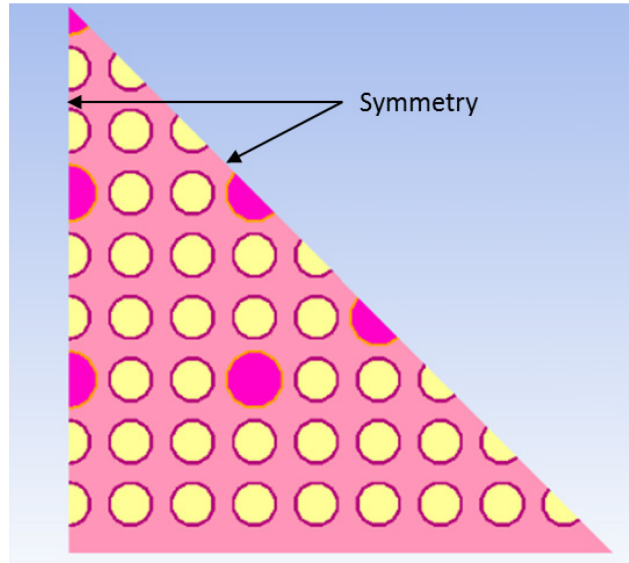


Figure 2-7 2D model to calculate k_{eff} for PWR single assembly (Cell 1 shown)

Similarly, 2D models were developed for each configuration that was validated to calculate the effective thermal conductivity as a function of temperature. In these models, the boundary conditions consisted of the fuel rods surrounded by the pool cell wall. Multiple runs at different powers for each assembly configuration were performed in order to generate a “database” that would represent the temperature range to which each assembly would be exposed. Equation 2-1 and Equation 2-2 show the radial and axial components of the effective conductivity in the PWR and BWR single assembly configurations and the center assembly in the 1x4 PWR configuration. Equation 2-2 and Equation 2-3 were applied to the peripheral assembly configuration since the heat source was not coming from the center of assembly itself like the other assemblies, but rather from the wall next to the center assembly.

$$k_{eff(radial)} = 0.2947 * \frac{Q}{4 * L_a * (T_{peak} - T_{edge})} \quad \text{Equation 2-1}$$

$$k_{eff(axial)} = \sum_i^n k_i * A_{i_ratio} \quad \text{Equation 2-2}$$

$$k_{eff(radial)} = \frac{Q * \Delta y}{A * \Delta T} \quad \text{Equation 2-3}$$

Where:

- k_{eff} = The effective thermal conductivity
- Q = the power
- L_a = the active length of the assembly
- T_{peak} = the maximum temperature in the assembly
- T_{edge} = the constant boundary condition temperature at the edge of the assembly
- k_i = the thermal conductivity of the material
- A_{i_ratio} = the area ratio
- Δy = the width of the assembly
- A = the cross sectional area
- ΔT = the difference in temperature between the hot wall and the assembly temperature area weighted average.

In order to verify the effective conductivity values obtained with this model, the results were compared with the results from the TRW report. The values in the TRW report were obtained using a finite element method. Table 2-21 summarizes the results of this comparison.

Table 2-21 Predicted and TRW Radial k_{eff} Comparison

Temperature (Kelvin)	k_{eff} (W/m ² *K)	k_{eff} (W/m ² *K) (calculated based on TRW report data)
298	0.4061	0.3987
473	0.6676	0.6763
673	1.1346	1.1890

Similarly, Figure 2-8 shows the 2D model used to calculate the effective radial thermal conductivity for the peripheral assembly in the 1x4 configuration. The model shows half of one of the peripheral assemblies, representing 1/8th of all the peripheral assemblies. This model applied constant heat flux on the hot wall, constant temperature at the opposing wall, and symmetry.

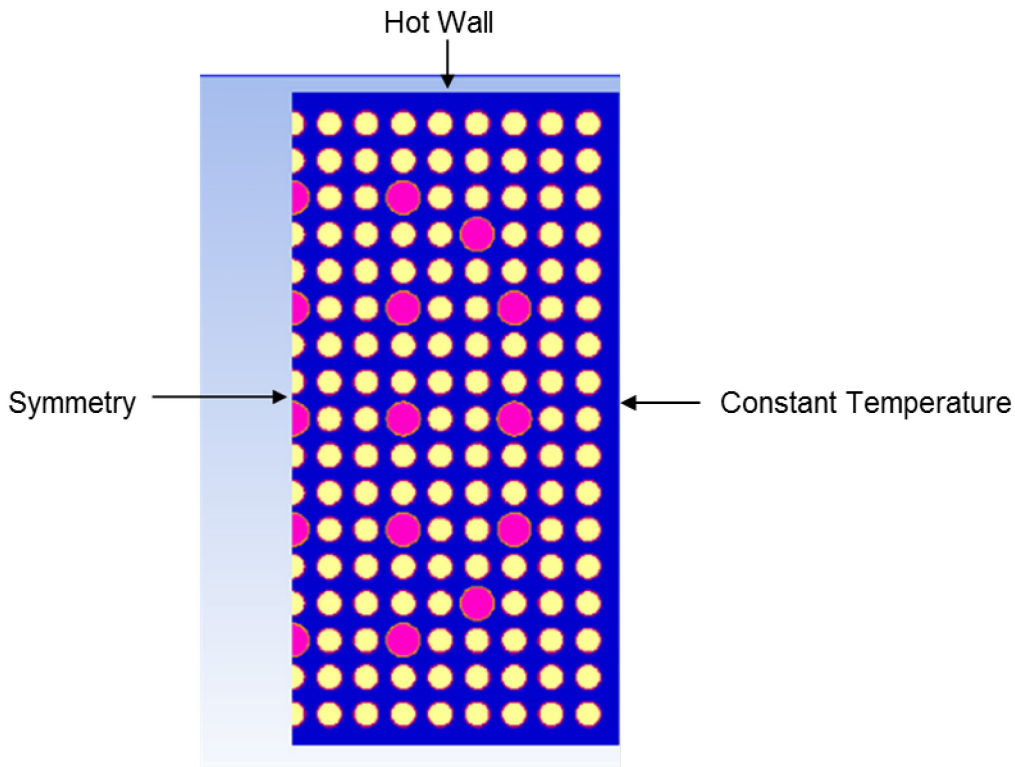


Figure 2-8 2D model to calculate k_{eff} for 1x4 PWR configuration (peripheral assembly)

Table 2-22 through Table 2-33 summarize the results for all configurations.

Table 2-22 PWR Cell 1 Porous Model—Radial k_{eff}

Temperature (Kelvin)	K_{eff} (W/m ² *K)
293	0.0846
312	0.0928
394	0.1308
465	0.1841
545	0.2622
631	0.3721

Table 2-23 PWR Cell 1 Porous Model—Axial k_{eff}

Temperature (Kelvin)	K_{eff} (W/m ² *K)
273	4.5186
400	5.1989
600	6.1722
800	7.0880
1,000	7.9906
1,100	8.4468

Table 2-24 PWR Cell 2 Porous Model—Radial k_{eff}

Temperature (Kelvin)	K_{eff} (W/m ² *K)
292	0.0967
311	0.1078
348	0.129
385	0.1523
456	0.2248
537	0.3343
580	0.4064

Table 2-25 PWR Cell 2 Porous Model—Axial k_{eff}

Temperature (Kelvin)	K_{eff} (W/m ² *K)
273	4.43
400	5.1
600	6.06
800	6.96
1,000	7.84
1,100	8.29

Table 2-26 1x4 PWR Center Assembly Porous Model—Radial k_{eff}

Temperature (Kelvin)	K_{eff} (W/m ² *K)
293	0.0867
312	0.0959
389	0.1357
459	0.1962
539	0.2866

Table 2-27 1x4 PWR Center Assembly Porous Model—Axial k_{eff}

Temperature (Kelvin)	K_{eff} (W/m ² *K)
273	4.21
400	4.8443
600	5.7517
800	6.6053
1,000	7.4466
1,100	7.8718

Table 2-28 1x4 PWR Peripheral Assembly Porous Model—Radial k_{eff}

Temperature (Kelvin)	K_{eff} (W/m ² *K)
293	0.1999
318	0.2664
348	0.3596
410	0.4601

Table 2-29 1x4 PWR Peripheral Assembly Porous Model—Axial k_{eff}

Temperature (Kelvin)	K_{eff} (W/m ² *K)
273	1.6066
400	1.8287
600	2.1162
800	2.3817
1,000	2.6573
1,100	2.8125

Table 2-30 BWR Fully Populated Cladding Region Porous Model—Radial k_{eff}

Temperature (Kelvin)	K_{eff} (W/m ² *K)
297	0.0981
324	0.1113
423	0.1576
489	0.215
564	0.2975
646	0.4121
733	0.5653

Table 2-31 BWR Fully Populated Cladding Region Porous Model—Axial k_{eff}

Temperature (Kelvin)	K_{eff} (W/m*K)
273	4.5002
400	5.2028
600	6.2560
800	7.2618
1,000	8.2211
1,100	8.8762

Table 2-32 BWR Partially Populated Cladding Region Porous Model—Radial k_{eff}

Temperature (Kelvin)	K_{eff} (W/m*K)
294	0.0959
321	0.11
410	0.155
478	0.2166
555	0.3061
639	0.4315
728	0.5998

Table 2-33 BWR Partially Populated Cladding Region Porous Model—Axial k_{eff}

Temperature (Kelvin)	K_{eff} (W/m*K)
273	4.0248
400	4.6537
600	5.5962
800	6.4961
1,000	7.3546
1,100	7.7621

The equivalent density for the porous models was calculated as shown in

$$\rho = \sum_i^n \rho_i * A_{i_ratio} \quad \text{Equation 2-4}$$

Where:

ρ = the density
 A_{ratio} = the area ratio

Table 2-34 lists the values used for each of the models.

Table 2-34 lists the values used for each of the models.

Table 2-34 Equivalent Porous Model Density

Assembly Configuration	Density (kg/m ³)
PWR single assembly (Cell 1)	1,562
PWR single assembly (Cell 2)	1,533
PWR 1x4 configuration (center assembly)	1,455
PWR 1x4 configuration (peripheral assembly)	1,355
BWR single assembly (fully populated rods region)	1,680
BWR single assembly (partially populated rods region)	1,503

The equivalent heat capacity for each porous model was calculated using Equation 2-5.

$$c_p = \sum_i^n c_{p_i} * m_{i_ratio} ; m_{i_ratio} = \frac{(\rho_i * A_{i_ratio})}{\rho} \quad \text{Equation 2-5}$$

Where:

- c_p = the heat capacity
- m_{ratio} = the mass ratio
- A_{ratio} = the area ratio

Table 2-35 to Table 2-40 illustrates the results and values used for each porous configuration.

Table 2-35 PWR Cell 1 Porous Model—Heat Capacity

Temperature (Kelvin)	c_p (J/kg*K)
273	571
400	662
600	731
800	770
1,000	801

Table 2-36 PWR Cell 2 Porous Model—Heat Capacity

Temperature (Kelvin)	c_p (J/kg*K)
273	571
400	662
600	731
800	770
1,000	801

Table 2-37 1x4 PWR Center Porous Model—Heat Capacity

Temperature (Kelvin)	c_p (J/kg*K)
273	571
400	662
600	731
800	770
1,000	801

Table 2-38 1x4 PWR Peripheral Assembly Porous Model—Heat Capacity

Temperature (Kelvin)	c_p (J/kg*K)
273	621
400	726
600	802
800	844
1,000	874

Table 2-39 BWR Fully Populated Cladding Region Porous Model—Heat Capacity

Temperature (Kelvin)	c_p (J/kg*K)
273	641
400	723
600	786
800	824
1,000	855

Table 2-40 BWR Partially Populated Cladding Region Porous Model—Heat Capacity

Temperature (Kelvin)	c_p (J/kg*K)
273	640
400	721
600	785
800	823
1,000	853

Another important parameter for the porous media model was the frictional coefficient for each assembly configuration. Three methods were used to calculate the friction coefficient. The first two methods used are shown in Equation 2-6 and Equation 2-7. The values for the variables in these equations were obtained from ANSYS FLUENT simulations of the detailed model for both the heated and isothermal models, respectively.

$$D = \frac{4*\tau_w}{\mu*V_{avginlet_por}*D_{hyd}} \quad \text{Equation 2-6}$$

$$D = \frac{\Delta P}{\mu*L*V_{avginlet_por}} \quad \text{Equation 2-7}$$

Where:

- D = the friction coefficient
- τ_w = the shear stress at the wall
- μ = the viscosity
- $V_{avg_inlet_por}$ = the average inlet velocity for the porous model
- D_{hyd} = the hydraulic diameter
- ΔP = the pressure difference
- L = the length of the assembly

The frictional coefficient obtained from either Equation 2-6 or Equation 2-7 was used as an initial input for the third method. The third method used the comparison of the peak cladding temperature (PCT) obtained from the detailed and porous models. The frictional coefficient of the porous media model was changed until the PCT matched. Table 2-41 and Table 2-42 show the values used for the porous model for each configuration using the third method.

Table 2-41 Friction Coefficient—PWR Assemblies

Power (kW)	Single Assembly Cell 1	Single Assembly Cell 2	1x4 Configuration Center Assembly	1x4 configuration Peripheral Assembly
0.5		1,005,000		
1	1,120,000	992,000	1,120,000	800,000

Table 2-42 Friction Coefficient—BWR Assemblies

Power (kW)	Single Assembly
1.369	547,000
2.236	529,000

The boundary conditions were representative of those present during the experiment. Figure 2-9 to Figure 2-14 show a schematic of the boundary conditions. Pressure inlet was used at the inlet (shown in blue), pressure outlet at the exit (shown in red), and volumetric heat source was used in the volume occupied by MgO powder. Laminar flow was assumed inside the assembly, as the Reynolds number was below 200. An operating pressure of 84,000 Pa and symmetry (shown in yellow) were used to reduce the extent of the analyzed control volume. The drain holes in the BWR assembly were represented in the porous model in the same manner as previously discussed in the detailed model. Section 2.1 provides more details.

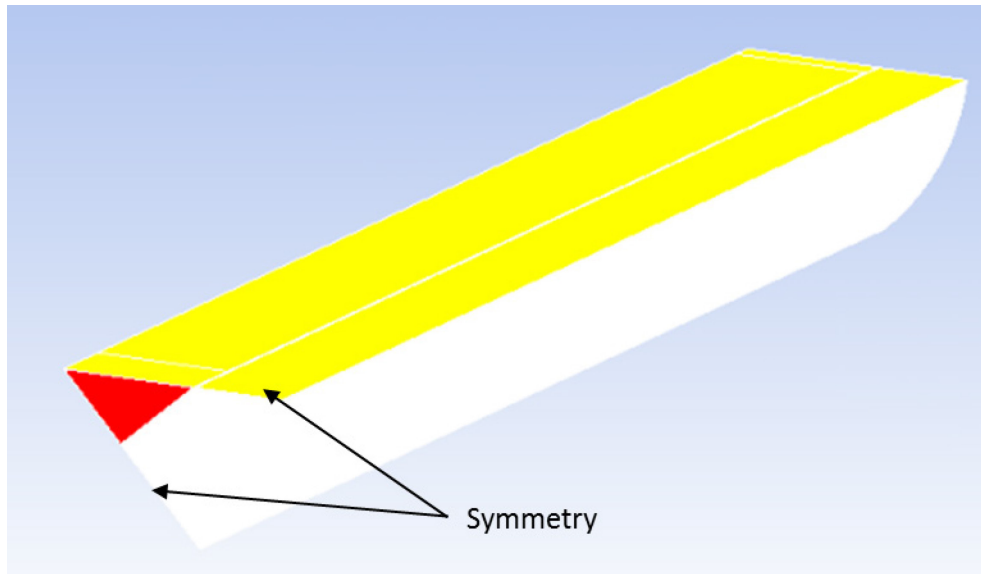


Figure 2-9 Porous PWR single assembly (Cell 2 illustrated)—boundary conditions

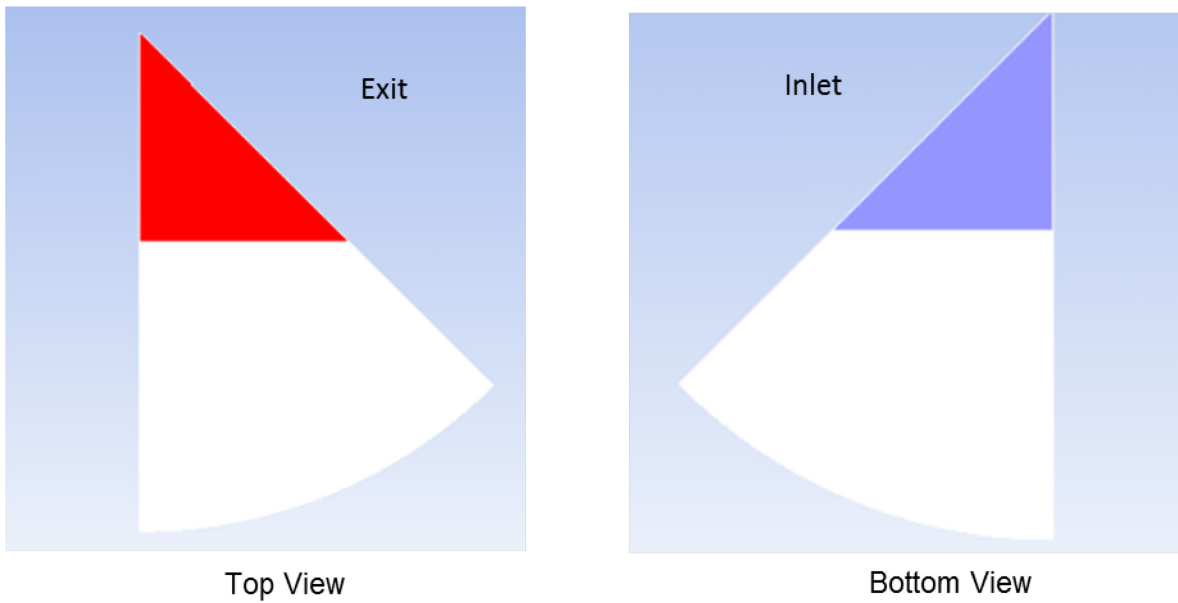


Figure 2-10 Porous PWR single assembly top and bottom views (Cell 2 illustrated)—boundary conditions

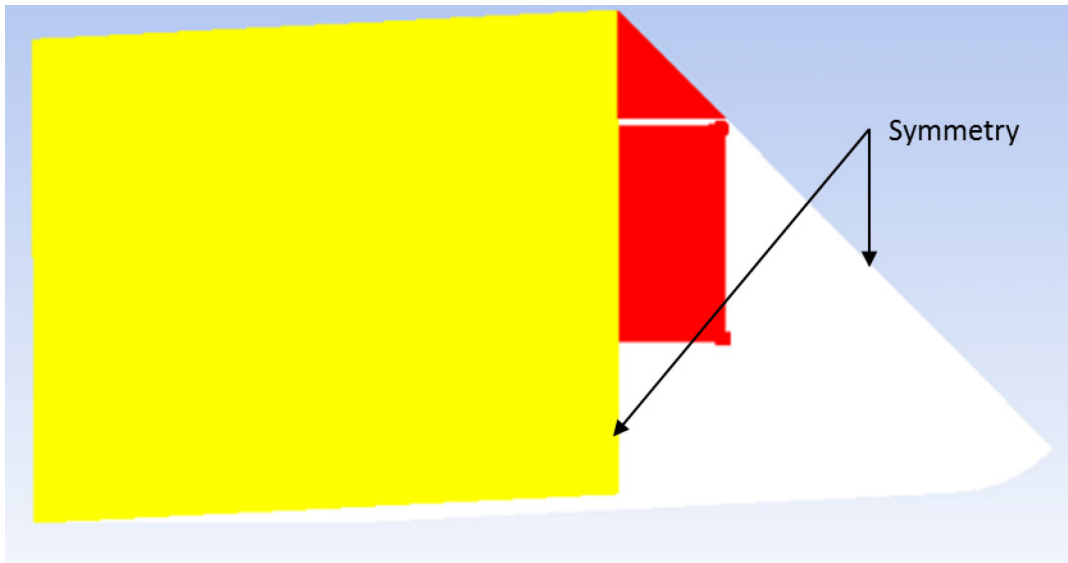


Figure 2-11 Porous PWR 1x4 configuration—boundary conditions

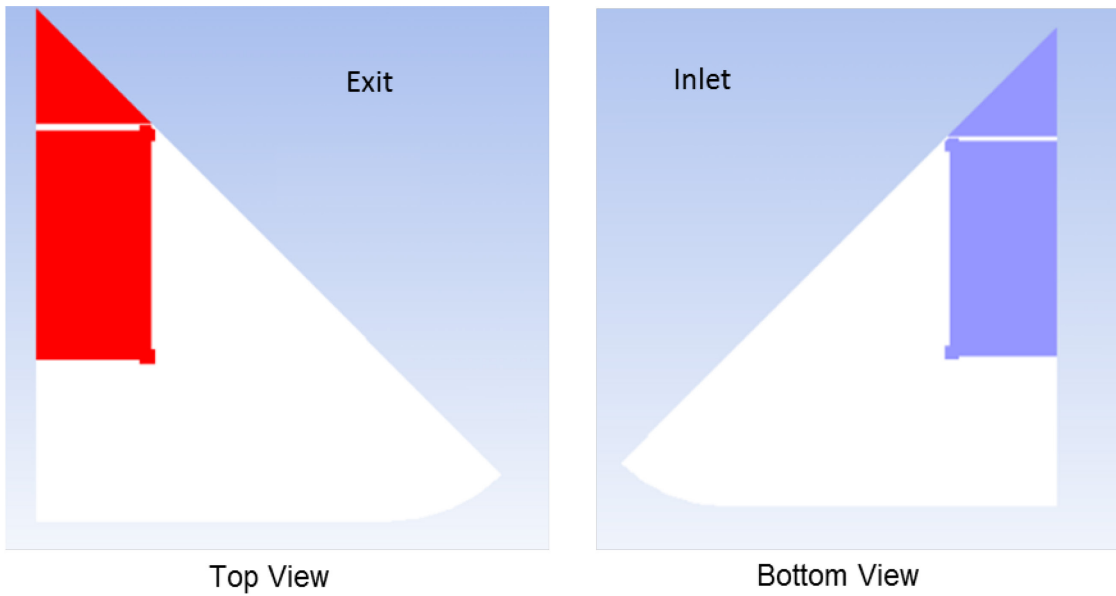


Figure 2-12 Porous PWR 1x4 configuration top and bottom views—boundary conditions

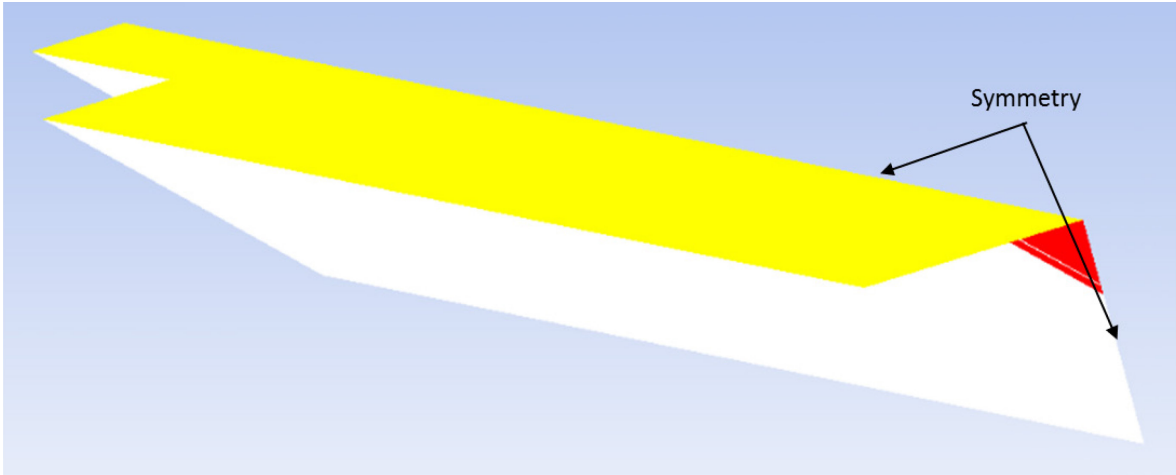


Figure 2-13 Porous BWR single assembly—boundary conditions

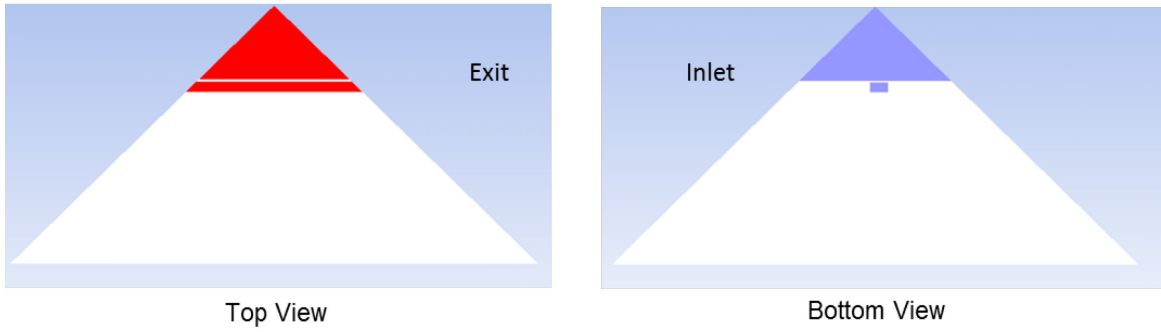


Figure 2-14 Porous BWR single assembly top and bottom views—boundary conditions

3 RESULTS AND DISCUSSION

3.1 Pressurized-Water Reactor Single Assembly (Cell 2: 223.4 mm)

The tables and graphs in this section summarize the results for a single PWR assembly with a cell size inner dimension of 223.4 mm (8.8 in.). Table 3-1 summarizes the scenarios modeled in this section. Section 3.1.1 includes a detailed description of the purpose for each of these models. This explanation provides the basis for all other models throughout this report.

Table 3-1 PWR Single Assembly Cell 2—Models

Model	Steady State		Transient
	1	0.5	
Power (kW)	1	0.5	1
Detailed	✓	✓	✓
Porous	✓	✓	✓
Extended Porous (laminar)	✓		
Extended Porous (turbulent)	✓		
Detailed (MgO - 3,204 (kg/m ³))			✓
Detailed (MgO -1,747 (kg/m ³))			✓

3.1.1 Power—1 kW (Steady State)

Three configurations were used to obtain the correct heat transfer coefficient at the external boundary. The first two configurations, which were used in the rest of this report, included only the insulated assembly without the surroundings, as shown in Figure 3-1 and Figure 3-2. These two configurations used model and porous media, respectively. Table 3-2 summarizes the results from these models including PCT, mass flow rate through the assembly, and the exterior wall temperature. The heat transfer interaction of the insulated assembly with the surroundings through the outside walls (i.e., external and top walls) was modeled using a heat transfer correlation. Table 3-3 shows the heat transfer coefficients for all these cases. The heat transfer coefficient correlations used for the vertical and horizontal walls came from Rohsenow et al. (1998) and Bergman et al. (2011). Radiation heat transfer was also included at these boundaries. The third configuration included the surroundings and used the porous media model, as depicted in Figure 3-3. Both laminar and turbulent flow models were considered to model the flow of the surroundings for this configuration to test the effect of the flow regime. The predictions in this section were undertaken to check the heat transfer boundary condition at the external wall of the first two configurations. This could be done simply by comparing the PCT temperature, air mass flow rate entering the assembly, and the external wall temperature of these models, as shown in Table 3-2, or by calculating the heat transfer coefficient from the extended model shown in Table 3-3. Figure 3-4 through Figure 3-6 summarize the results obtained for each of these configurations and models. Cell wall temperature profiles were used to compare the CFD modeling approaches (i.e., detailed vs. porous modeling), as Figure 3-5 shows. The same approach was taken for all other configurations in the NUREG.

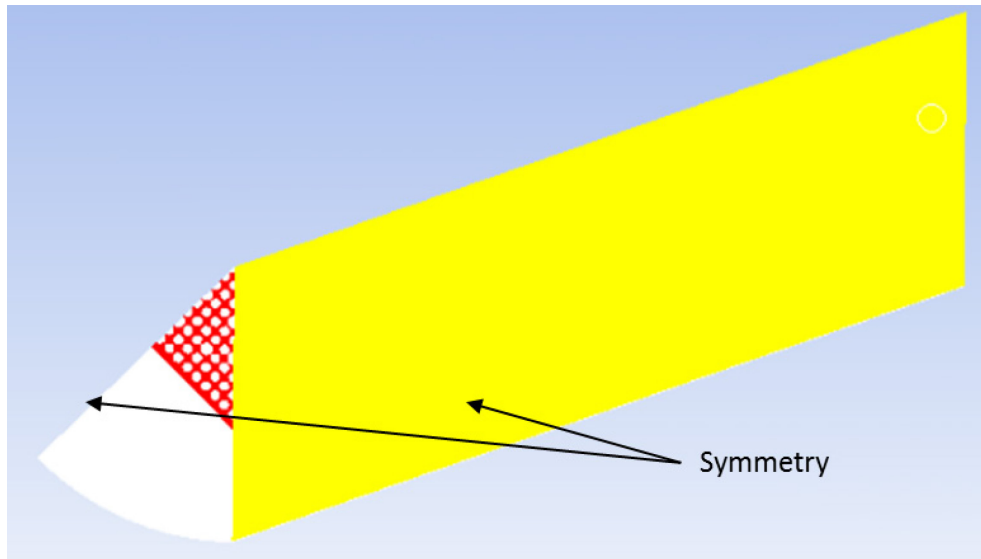


Figure 3-1 Detailed configuration—PWR single assembly Cell 2

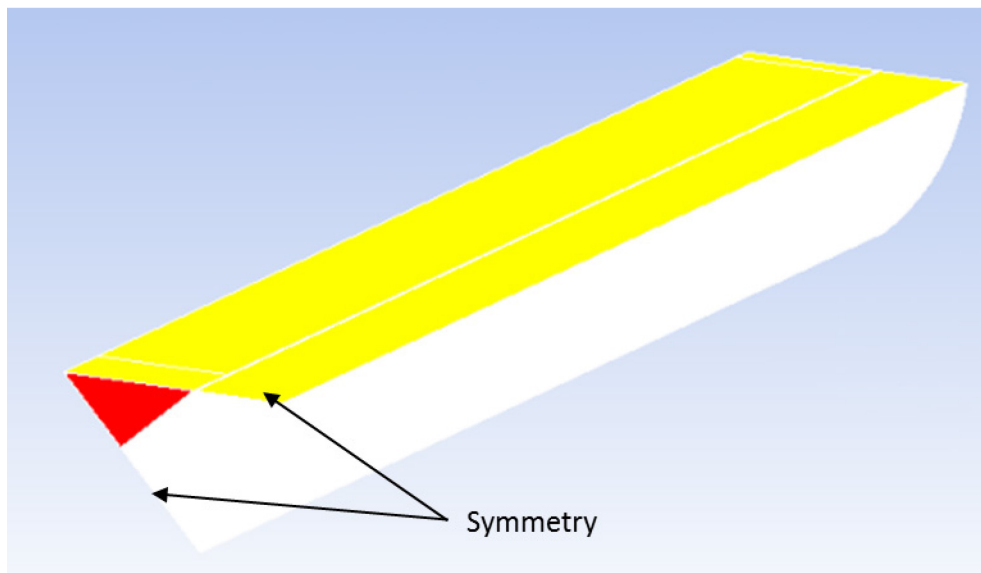


Figure 3-2 Porous configuration—PWR single assembly Cell 2

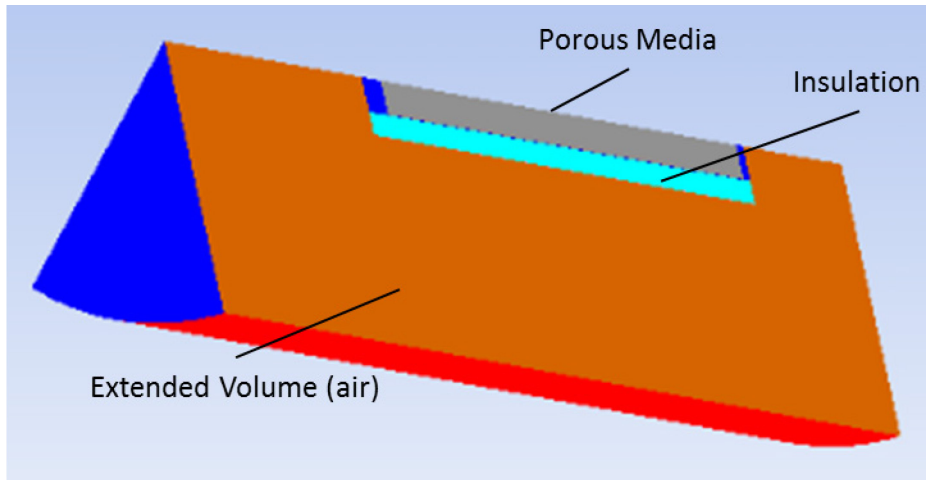


Figure 3-3 Porous configuration for extended models—PWR single assembly Cell 2

Table 3-2 PWR Cell 2 Steady-State Summary Results at 1 kW

Model	PCT (K)	Mass Flow Rate (kg/s)	Exterior Wall Temperature (K)
Detailed	533	0.00048	310
Porous	533	0.00047	311
Porous Extended (laminar)	530	0.00047	312
Porous Extended (turbulent)	530	0.00048	312
Experiment at 20 hours	525	0.00052	310

Table 3-3 PWR Cell 2 Steady-State Convected Heat and Heat Transfer Coefficient at 1 kW

Model	Exterior Wall Convected Heat (W)	Exterior Wall Heat Transfer Coefficient (W/m ² .K)	Top Wall Convected Heat (W)	Top Wall Heat Transfer Coefficient (W/m ² .K)
Detailed	8.4 (from Correlations)	1.89 (from Correlations)	1.02 (from Correlations)	5.52 (from Correlations)
Porous	9.1 (from Correlations)	1.88 (from Correlations)	0.93 (from Correlations)	5.15 (from Correlations)
Porous Extended (laminar)	8.9 (from CFD predictions)	1.84 (from CFD predictions)	0.69 (from CFD predictions)	2.76 (from CFD predictions)
Porous Extended (turbulent)	8.9 (from CFD predictions)	1.85 (from CFD predictions)	0.82 (from CFD predictions)	3.32 (from CFD predictions)

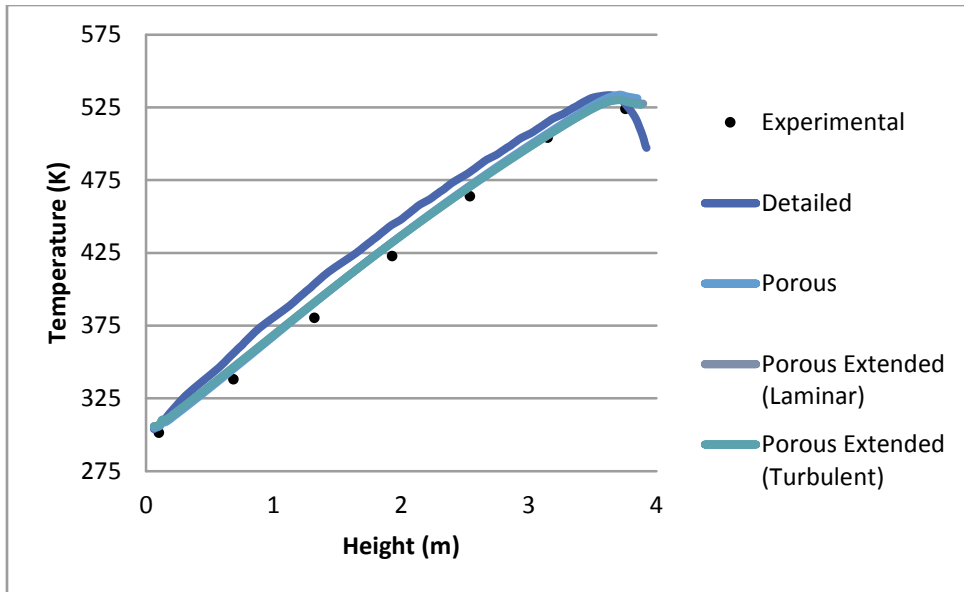


Figure 3-4 PWR Cell 2 steady-state PCT as a function of height at 1 kW

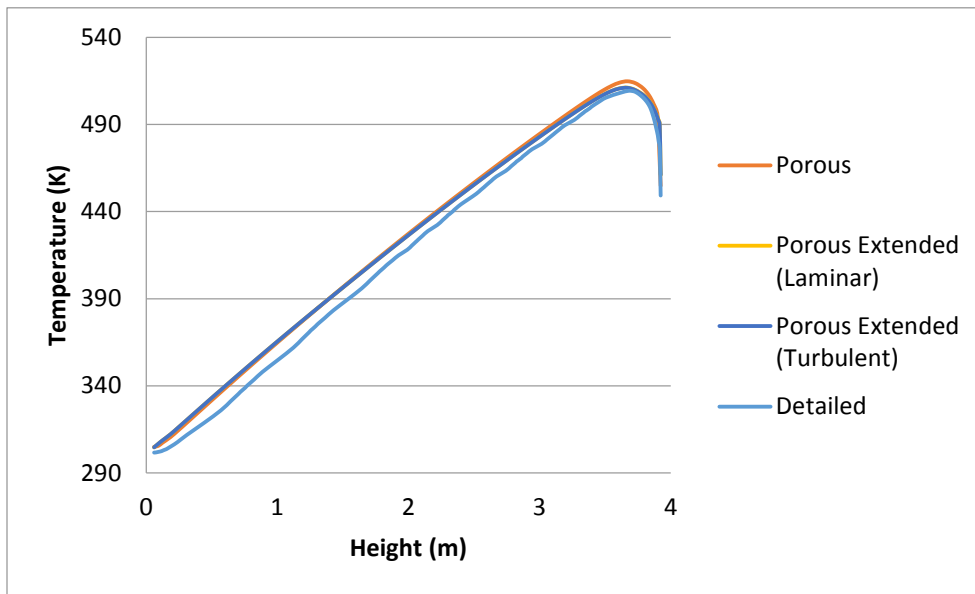


Figure 3-5 PWR Cell 2 steady-state pool cell wall maximum temperature as a function of height at 1 kW

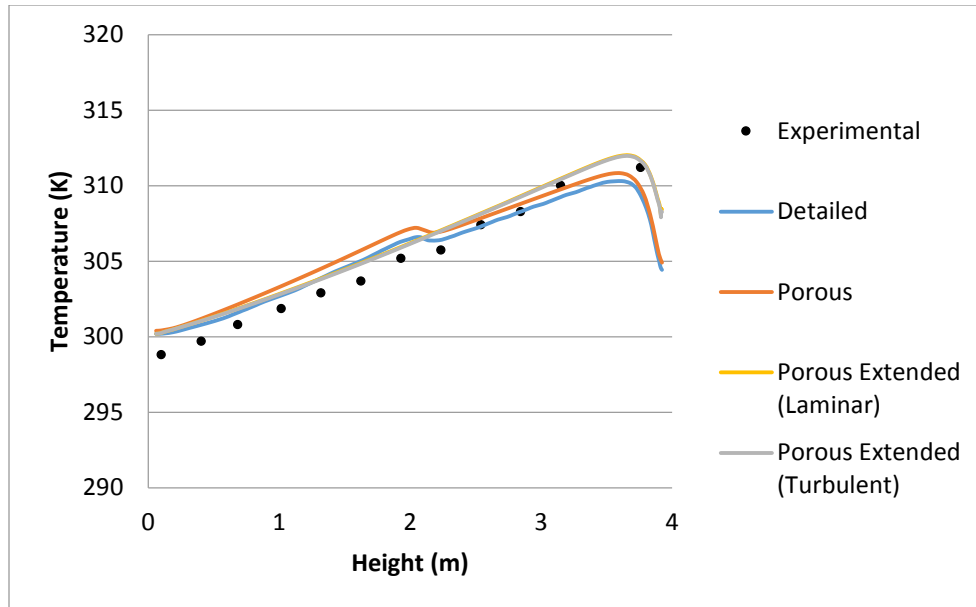


Figure 3-6 PWR Cell 2 steady-state exterior wall maximum temperature as a function of height at 1 kW

Table 3-2 and Table 3-3 results show that the heat transfer correlations used in the nonextended models predicted very well the heat transfer at the walls surrounding the insulated assembly. This is also apparent in Figure 3-4 through Figure 3-6 when comparing the models. As shown in these figures, the effect of turbulence on the extended models is negligible.

The porous model predicted the profiles of the PCT, external wall, and cell wall favorably, as shown in Figure 3-4 through Figure 3-6. In addition, the porous media model predictions were slightly more conservative than the detailed model. As such, the choice for the porous media parameters, as explained in Section 2.2, such as frictional factor and the effective heat conductivity, are justified. The initial guess of the friction factor was obtained from the isothermal pressure drop method or the isothermal shear stress method. The final tuning of the friction factor was obtained by comparing the PCT values between the porous and the detailed models. Further, the experimental data in these plots are shown at the last time step (20 hours). The CFD models for the detailed and the porous models predicted very closely the profile of the PCT and the external wall temperature obtained in the experiment. Any discrepancy between the experimental data and the CFD predictions can be attributed to the fact that steady state was not yet reached in the final step of the experiment as well as the uncertainty from both the experiment and grid convergence index (GCI) calculations (see Section 4).

3.1.2 Power—1 kW (Transient)

Figure 3-7 through Figure 3-13 show that CFD predictions matched the experimental data profile for the PCT, mass flow rate, pool cell wall, and external wall temperature closely. The predictions obtained from CFD also matched the profiles of the experimental data for the PCT and external wall temperature at 20 hours (see Table 3-4 and Figure 3-11 through Figure 3-13). Any discrepancy between the CFD predictions and experimental data may be attributed to the uncertainty of the thermal mass (i.e., ρ^*c_p , where ρ is the density and c_p is the specific heat capacity) used in the CFD predictions. Section 3.1.2.1 provide a more detailed analysis of this discrepancy. As a general highlight, the higher the thermal mass, the more resistance to heat

transfer and the lower the temperature. Additionally, this discrepancy can be attributed to the uncertainty of measurement and CFD discretization error (see Section 4). Another fact that can lead to this discrepancy is the possibility of leakage through the top of the 25 guide tubes. The tops of the guide tubes were fitted with spherical objects. This type of seal leaks quickly as the assembly is heated. As such, potential air flow rate can lower the temperature of the experimental setup.

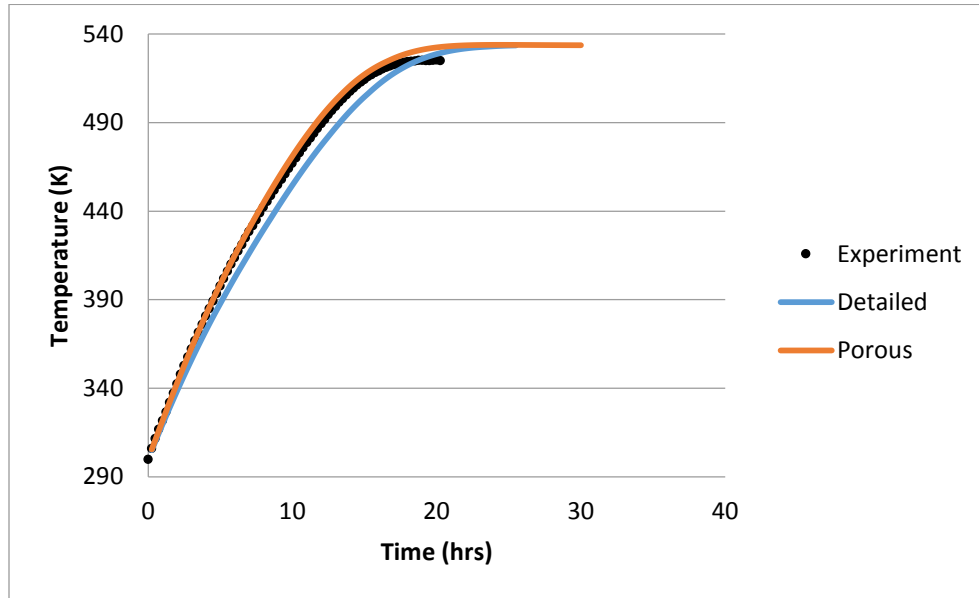


Figure 3-7 PWR Cell 2 PCT as a function of time at 1 kW

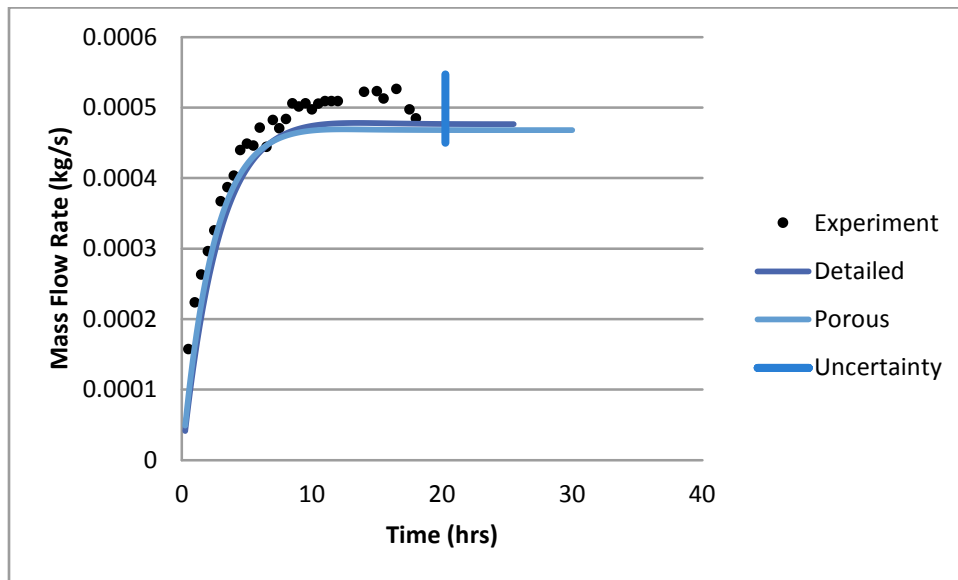


Figure 3-8 PWR Cell 2 mass flow rate as a function of time at 1 kW

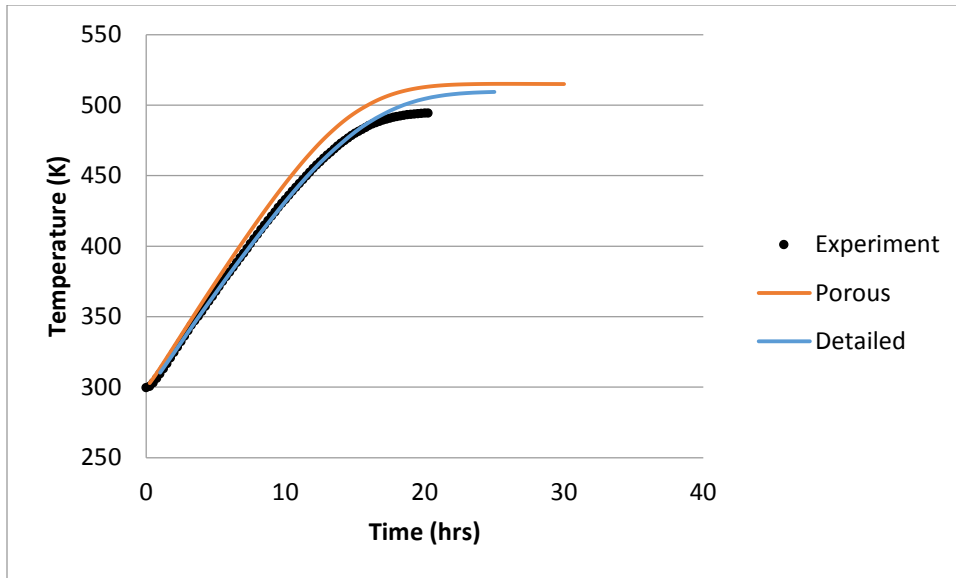


Figure 3-9 PWR Cell 2 pool cell wall maximum temperature as a function of time at 1 kW

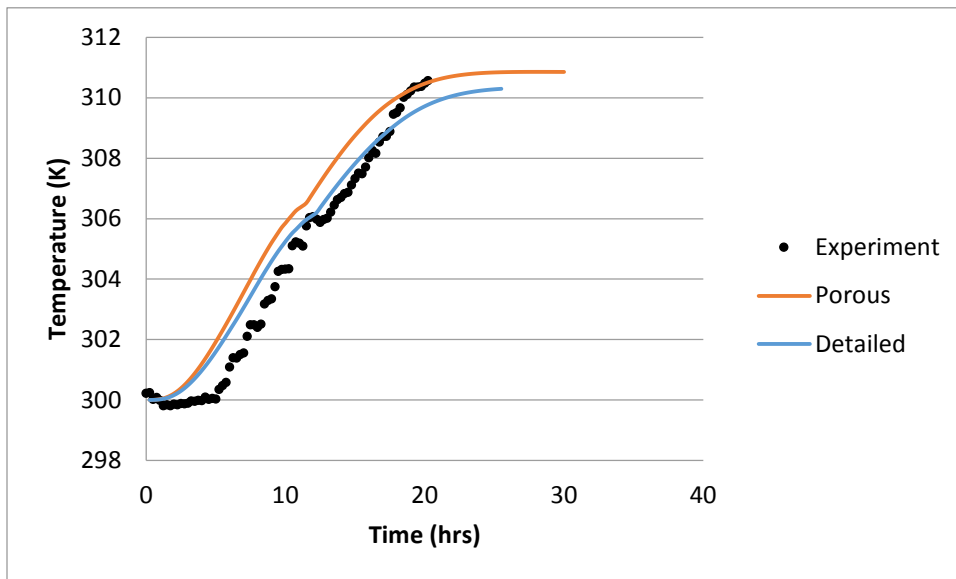


Figure 3-10 PWR Cell 2 exterior wall maximum temperature as a function of time at 1 kW

Table 3-4 PWR Single Assembly Cell 2—PCT and Mass Flow rate at 1 kW at 20 Hours

Model	PCT (K)	Mass Flow Rate (kg/s)
Experiment	525	0.00053
Detailed	529	0.00048
Porous	532	0.00047

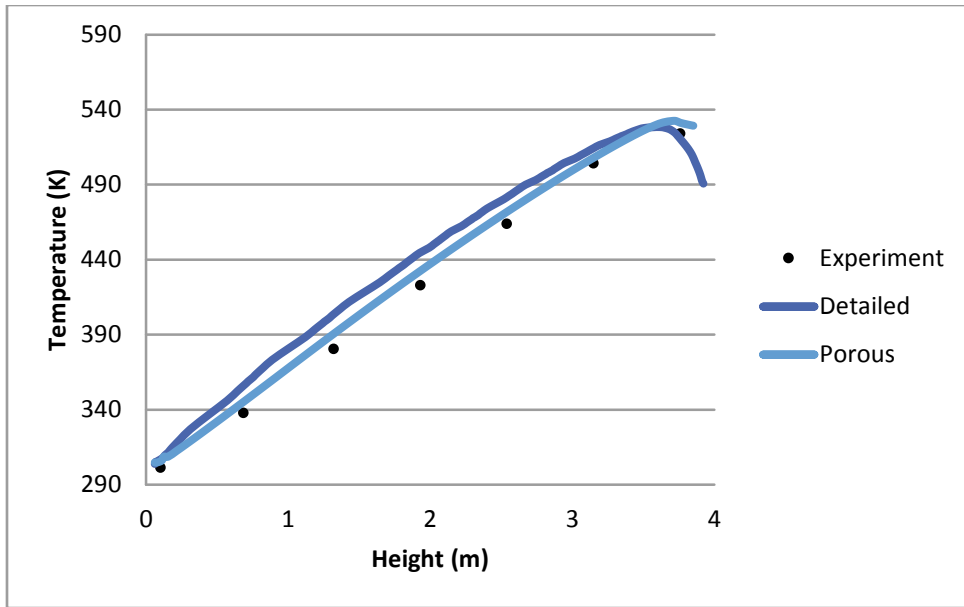


Figure 3-11 PWR Cell 2 PCT as a function of height at 1 kW at 20 hours

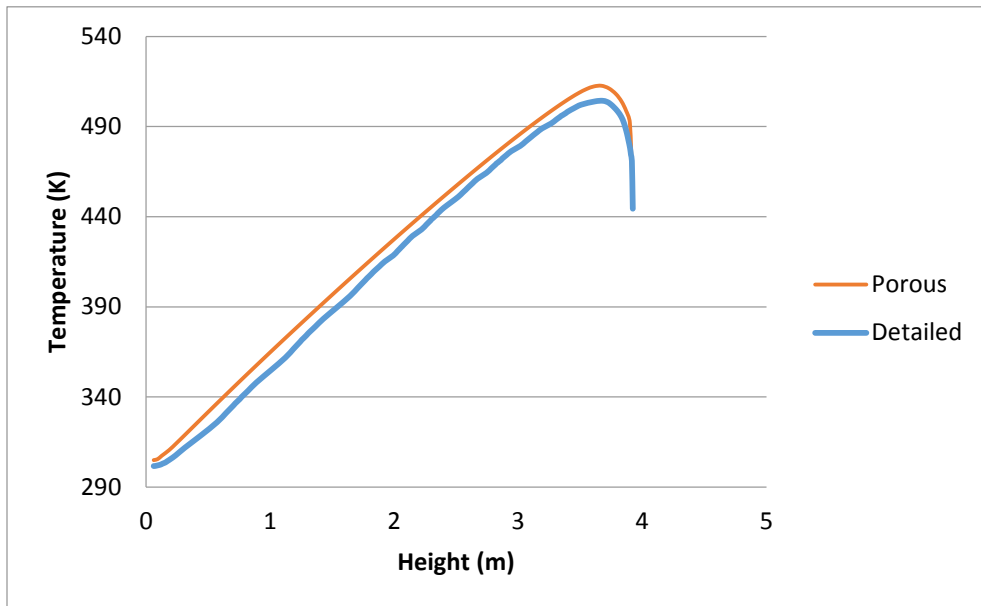


Figure 3-12 PWR Cell 2 pool cell wall maximum temperature as a function of height at 1 kW at 20 hours

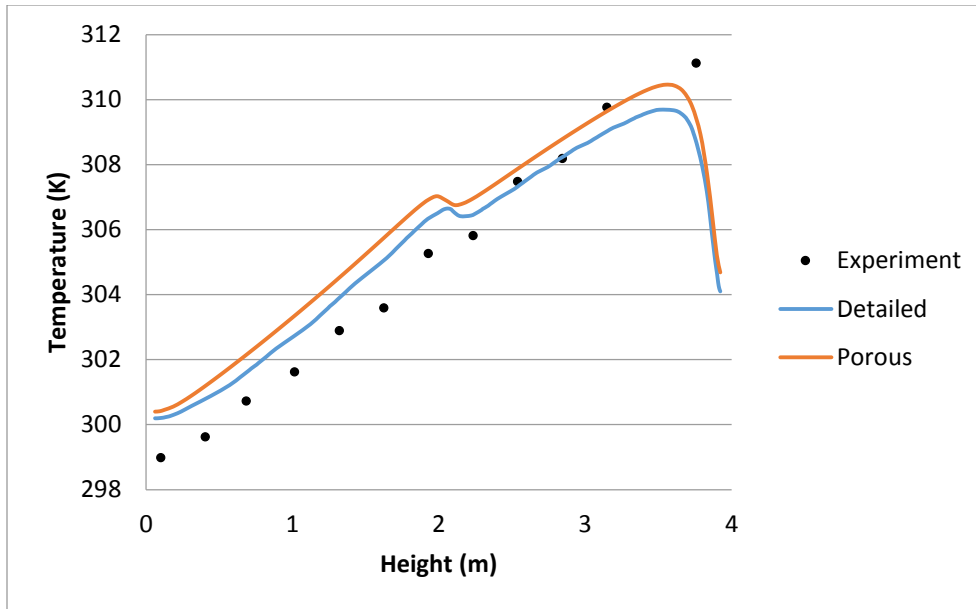


Figure 3-13 PWR Cell 2 exterior wall maximum temperature as a function of height at 1 kW at 20 hours

As seen in the figures for the power of 1 kilowatt (kW) for both the transient and steady analyses, the porous media model predictions matched the detailed model predictions and the experimental data closely. The close prediction is the result of using the right friction factor. In all porous media models, the difference in friction factor values obtained from the 3 methods mentioned in Section 2.2 was negligible. As such, the initial guess of the friction factor was obtained from the isothermal pressure drop method or the isothermal shear stress method. The final tuning of the friction factor was obtained by comparing the PCT values with the porous and the detailed models.

3.1.2.1 Thermal Mass Uncertainty

Figure 3-11 and Table 3-4 show that the PCT at 20 hours predicted by CFD is slightly higher than the experimental data. Therefore, sensitivity study was performed by increasing and decreasing the thermal mass of the MgO of the detailed model. The density was first increased to 3,204 kg/m³, keeping c_p unchanged. The density was then decreased to 1,747 kg/m³, also keeping c_p unchanged. Figure 3-14 through Figure 3-20 show the results of this sensitivity study.

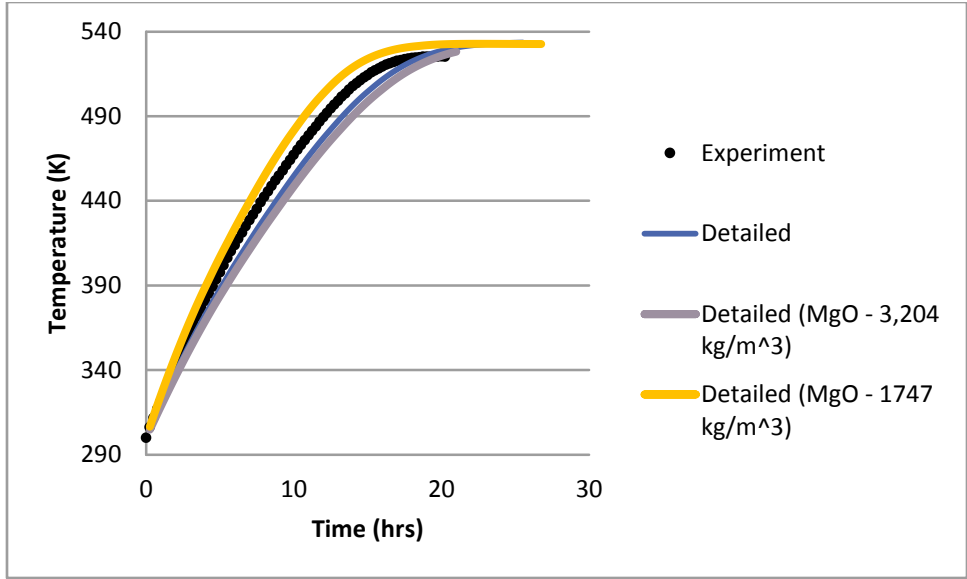


Figure 3-14 PWR Cell 2 PCT as a function of time at 1 kW

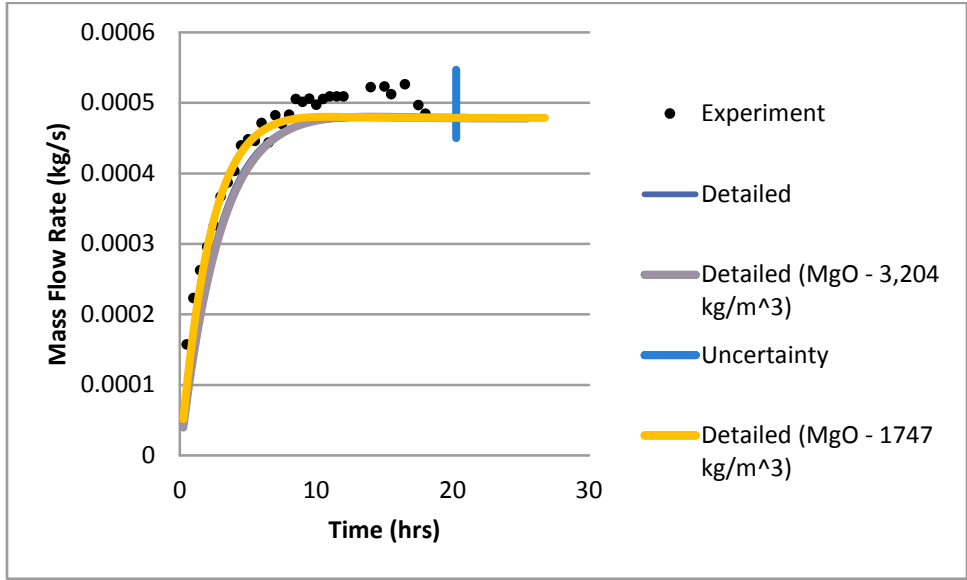


Figure 3-15 PWR Cell 2 mass flow rate as a function of time at 1 kW

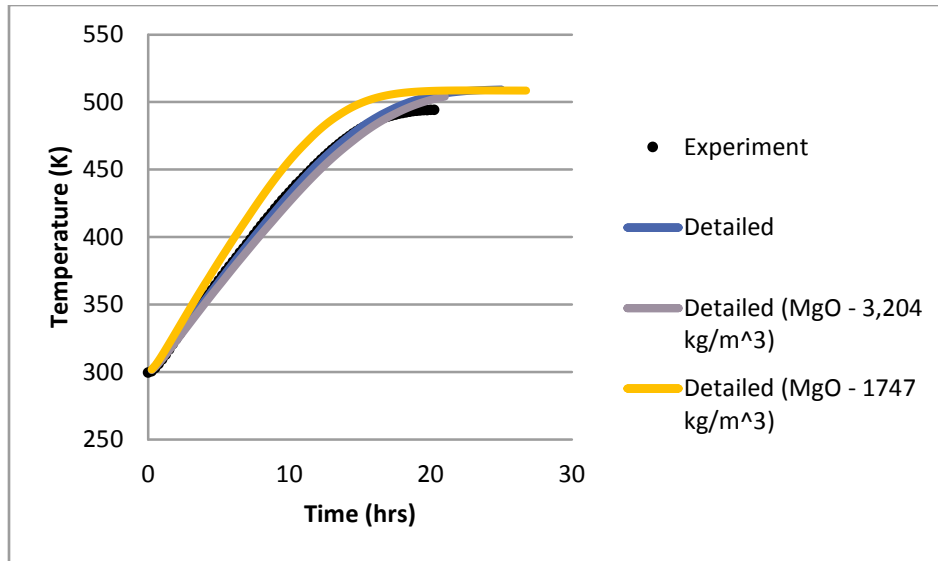


Figure 3-16 PWR Cell 2 pool cell wall maximum temperature as a function of time at 1 kW

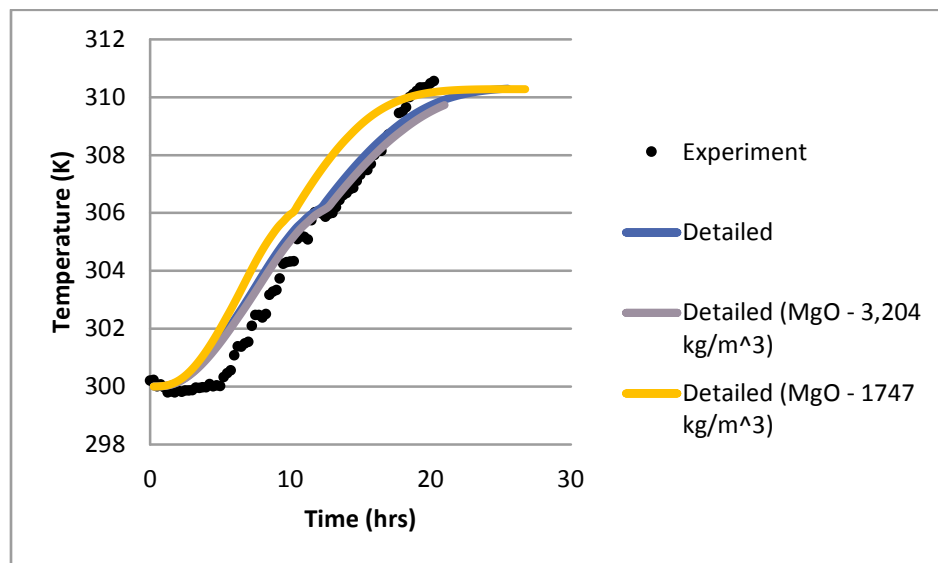


Figure 3-17 PWR Cell 2 exterior wall maximum temperature as a function of time at 1 kW

Table 3-5 PWR Single Assembly Cell 2 (Thermal Mass)—PCT and Mass Flow rate at 1 kW at 20 hours

Model	PCT (K)	Mass Flow Rate (kg/s)
Experiment	525	0.00053
Detailed	529	0.00048
Detailed (MgO - 3,204 (kg/m ³))	527	0.00048
Detailed (MgO - 1,747 (kg/m ³))	532	0.00048

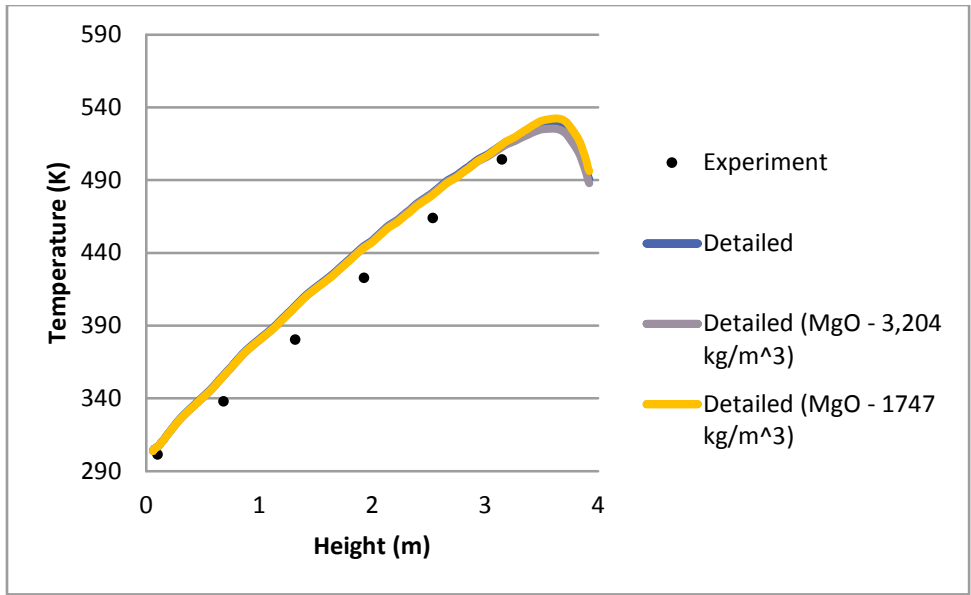


Figure 3-18 PWR Cell 2 PCT as a function of height at 1 kW at 20 hours

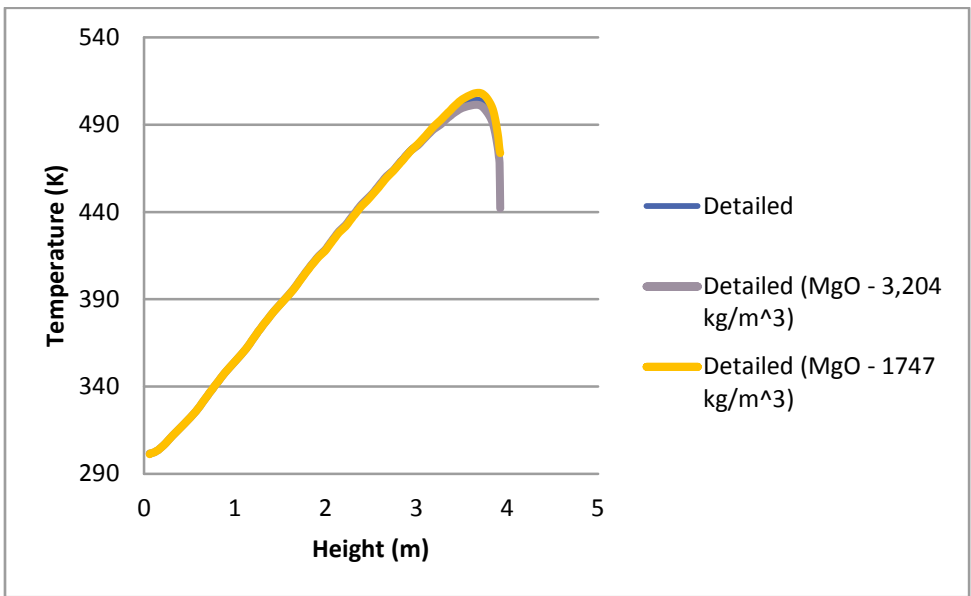


Figure 3-19 PWR Cell 2 pool cell wall maximum temperature as a function of height at 1 kW at 20 hours

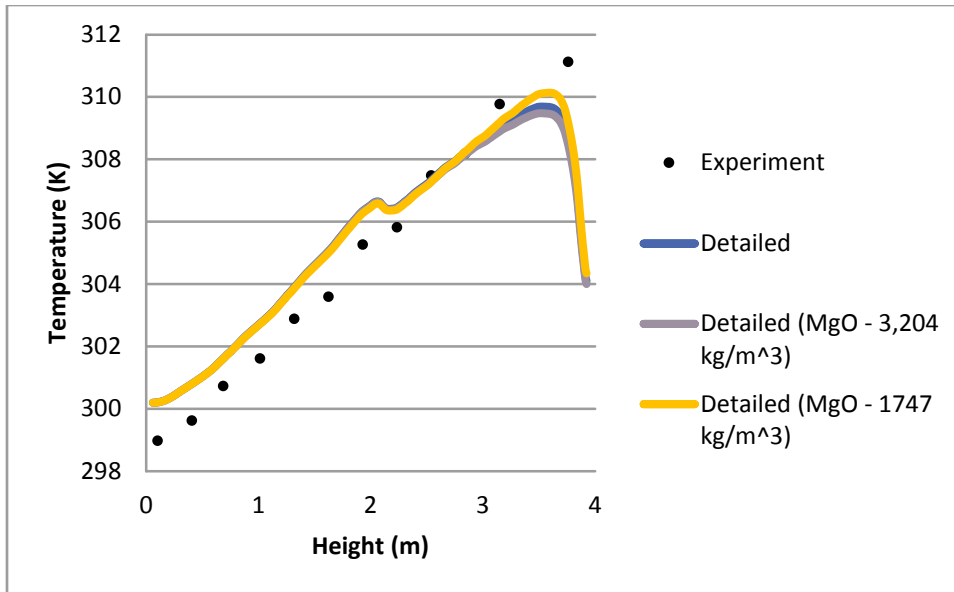


Figure 3-20 PWR Cell 2 exterior wall maximum temperature as a function of height at 1 kW at 20 hours

The results in this sensitivity study shows that steady state was not yet reached, as the temperature is still a function of the thermal mass of the fuel used. As Figure 3-14 shows, the variation of the thermal mass did envelope the experimental data. This will attest that the thermal mass can influence the transient thermal response of the fuel assembly.

3.1.3 Power—0.5 kW (Steady State)

Table 3-6 shows that steady state was reached at the end of the experiment (i.e., 19 hours) by looking at the rate of change of PCT and mass flow rate with time.

Figure 3-21 through Figure 3-23 show that CFD predictions matched the profile the experimental data of the PCT, mass flow rate, pool cell wall temperature, and external wall temperature closely and favorably. The predictions obtained from CFD also matched the profiles of the experimental data for PCT and external wall temperature at time of 19 hours. Any discrepancy between the CFD predictions and experimental data can be attributed to the uncertainty of measurement and CFD discretization error, as shown in Section 4 .

Figure 3-21 through Figure 3-23 also show that the porous media model predictions matched the detailed model predictions and the experimental data closely. The close prediction is the result of using the right friction factor. In all the porous media models, the difference in friction factor values obtained from the three methods mentioned in Section 2.2 were negligible. As such, the initial guess of the friction factor obtained from the isothermal pressure drop method or the isothermal shear stress method was a good prediction. The final tuning of the friction factor was performed using the PCT values between the porous and the detailed models.

Table 3-6 PWR Cell 2 Steady-State Mass Flow Rate at 0.5 kW

Model	PCT (K)	Mass Flow Rate (kg/s)	Exterior Wall Temperature (K)
Detailed	434	0.00042	304
Porous	434	0.00041	304
Experiment at 19 hours	432	0.00042	304

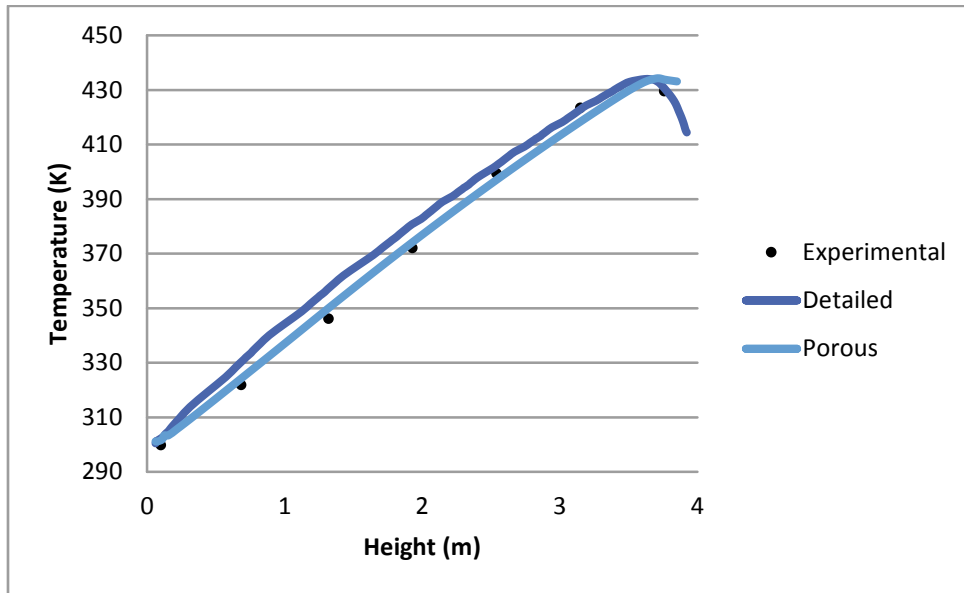


Figure 3-21 PWR Cell 2 steady-state PCT as a function of height at 0.5 kW

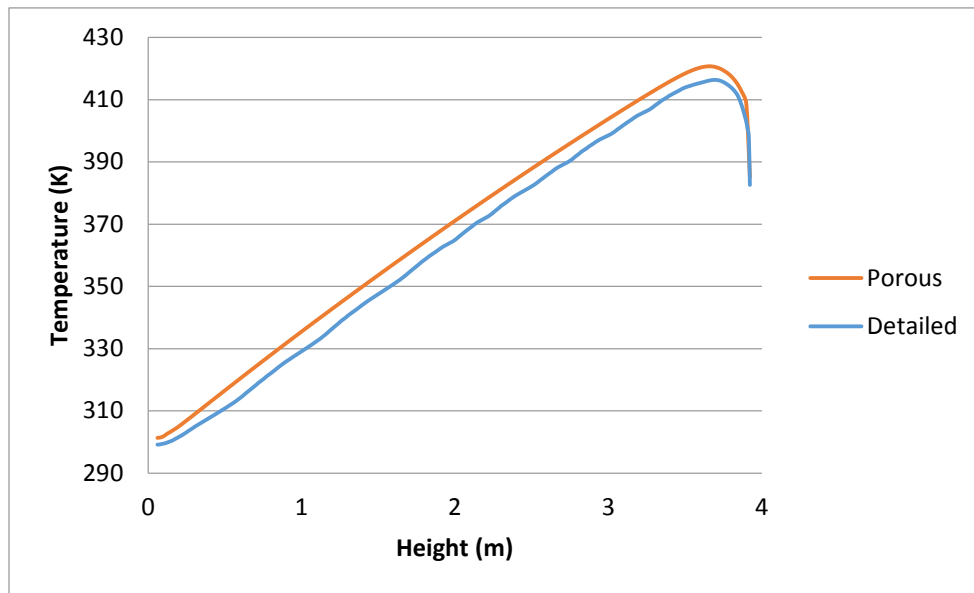


Figure 3-22 PWR Cell 2 steady-state pool cell wall maximum temperature as a function of height at 0.5 kW

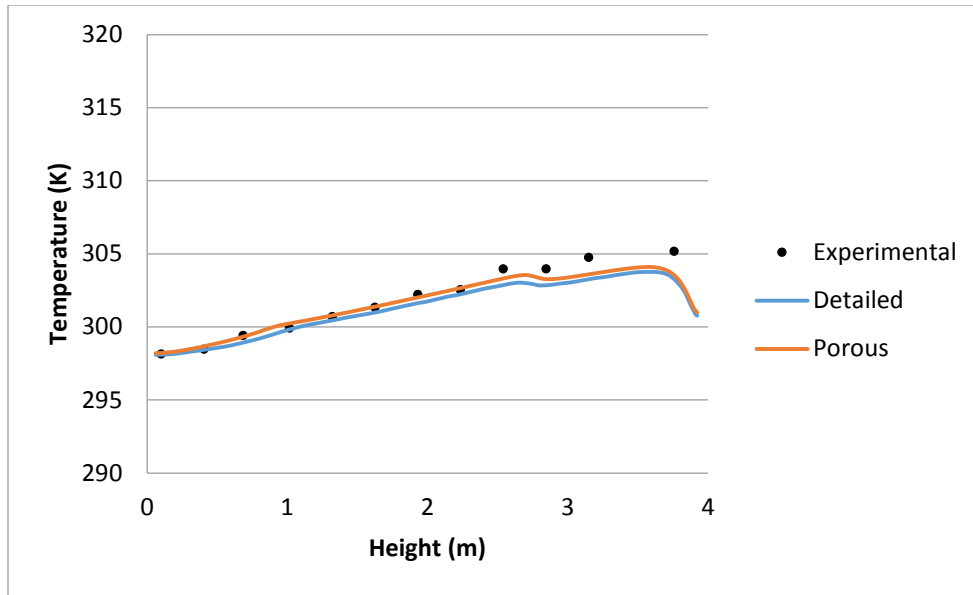


Figure 3-23 PWR Cell 2 steady-state exterior wall maximum temperature as a function of height at 0.5 kW

3.2 Pressurized-Water Reactor Single Assembly (Cell 1: 221.3 mm)

The tables and graphs in this section summarize the results for a single PWR assembly with a cell size inner dimension of 221.3 mm (8.7 in.). Table 3-7 summarizes the scenarios modeled in this section. Sections 3.2.1 and 3.2.2 summarize the PWR Cell 1 assembly experiment and CFD results for steady-state and transient runs.

Table 3-7 PWR Single Assemble Cell 1—Models

Model	Steady State	Transient
Power (kW)	1	1
Detailed	✓	
Porous	✓	✓

3.2.1 Power—1 kW (Steady State)

Figure 3-24 and Figure 3-25 show the PCT and pool cell wall temperature as a function of height. As the experiment had not yet reached steady state, the PCT predictions in Figure 3-24 are slightly higher than the experimental data. Table 3-8 also reflects slightly higher predictions than experimental data. Figure 3-24 and Figure 3-25 show that the predictions from both the detailed and porous models agree favorably.

Table 3-8 PWR Cell 1 Steady-State Mass Flow Rate at 1 kW

Model	PCT (K)	Mass Flow Rate (kg/s)	Exterior Wall Temperature (K)
Detailed	560	0.00041	312
Porous	560	0.00041	312
Experiment at 20 hours	545	0.00045	314

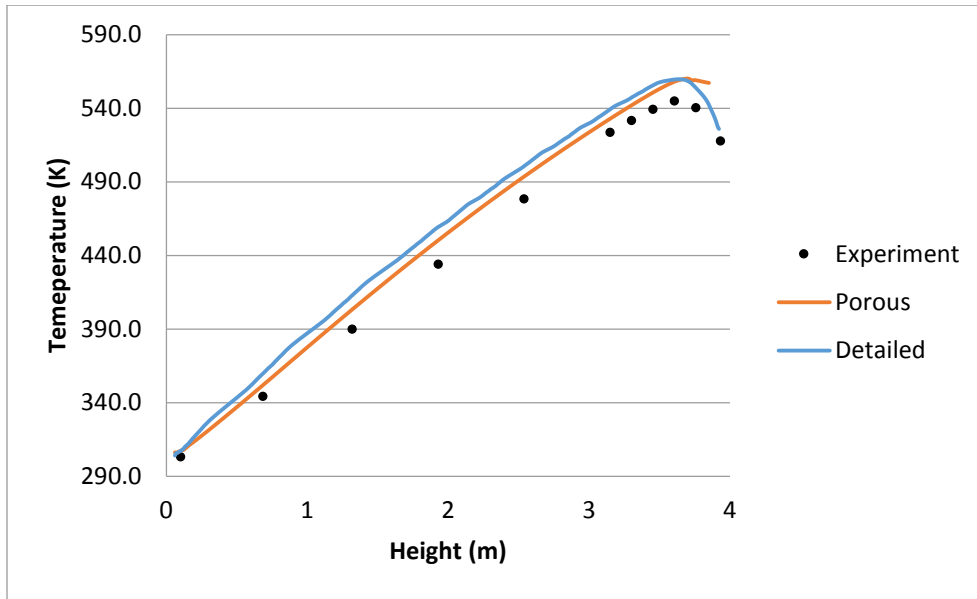


Figure 3-24 PWR Cell 1 steady-state PCT as a function of height at 1 kW

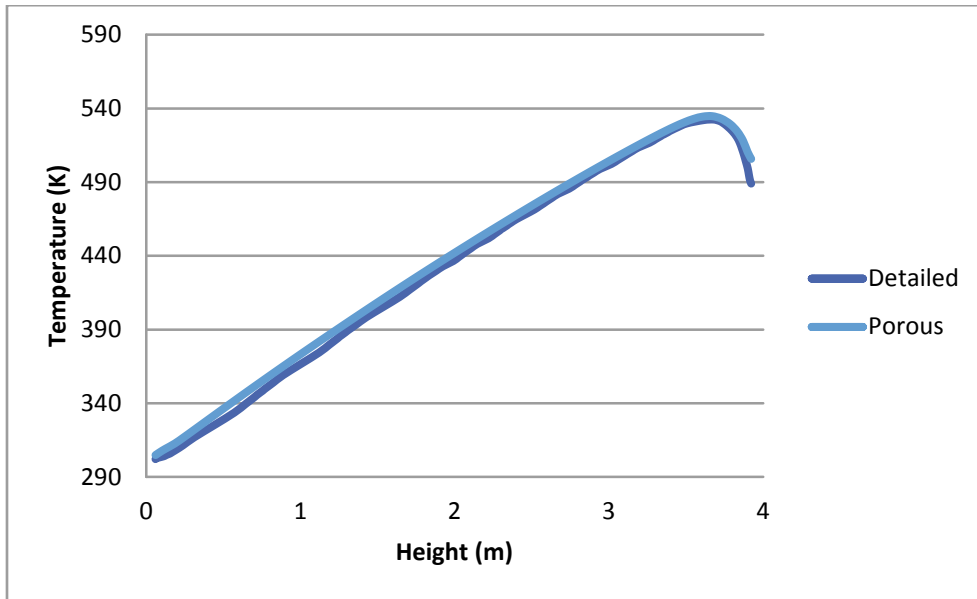


Figure 3-25 PWR Cell 1 steady-state pool cell wall temperature as a function off height at 1 kW

3.2.2 Power—1 kW (Transient)

The CFD prediction in this section was obtained by using only porous media model, as it is the method of choice for the dry cask applicants. Additionally, the discrepancy between the detailed and porous models is minimal, as shown in Section 3.2.1. Figure 3-26 and Figure 3-27 show the PCT and mass flow rate as a function of time. Any discrepancy between the prediction using the porous model and the experimental data can be attributed to the measurement errors as well as the discretization error summarized in Section 4 .

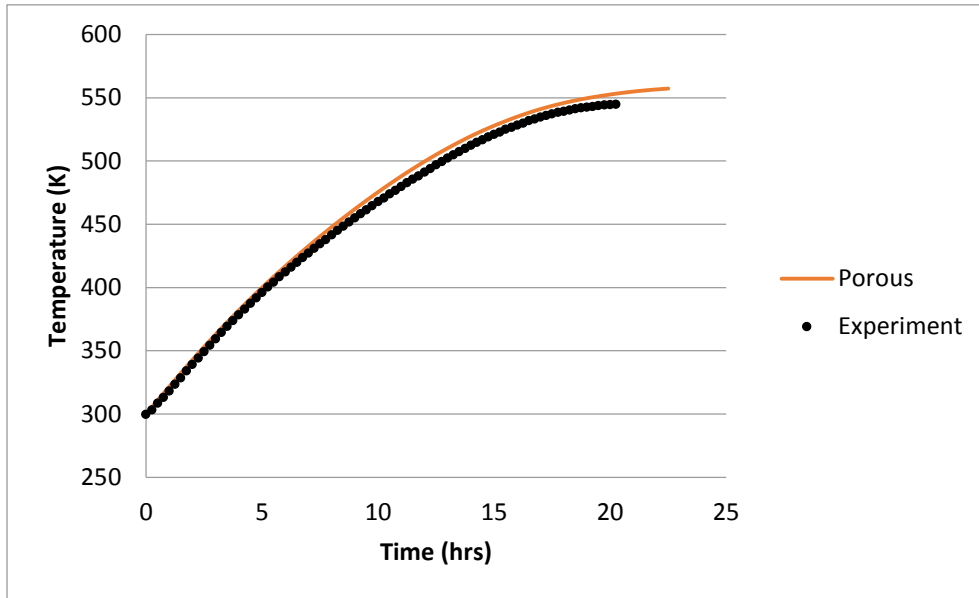


Figure 3-26 PWR Cell 1 PCT as a function of time at 1 kW

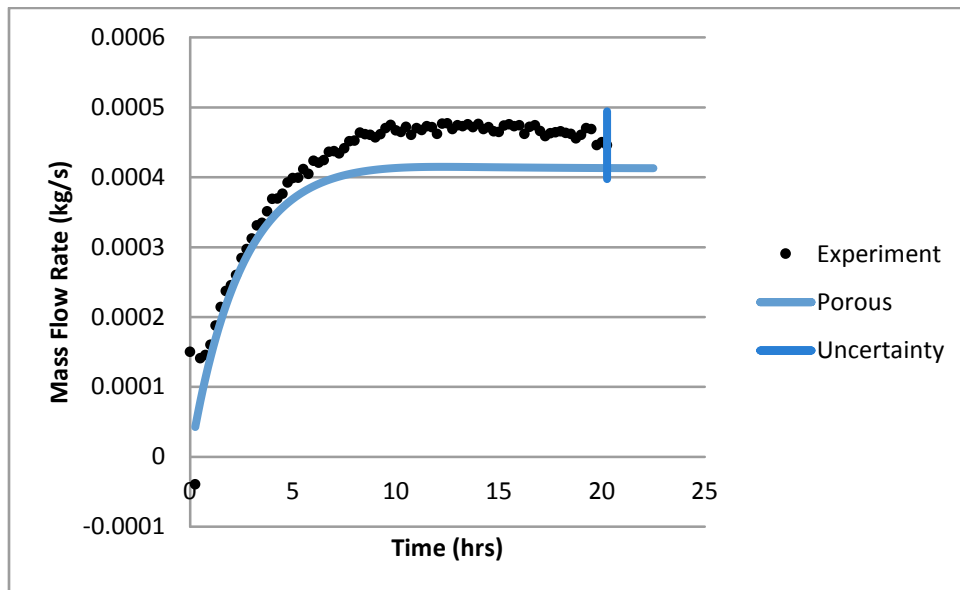


Figure 3-27 PWR Cell 1 mass flow rate as a function of time at 1 kW

3.3 Pressurized-Water Reactor 1x4 Assembly Configuration

The tables and graphs in this section summarize the results for a PWR 1x4 assembly. Table 3-9 summarizes the scenarios modeled in this section.

Table 3-9 PWR 1x4 Configuration—Models

Model	Steady State	Transient
Power (kW)	1	1
Detailed	✓	✓
Porous	✓	✓

3.3.1 Power—1 kW (Steady State)

Figure 3-28 through Figure 3-31 show the steady-state CFD predictions and the experiment at 24 hours. The results of the experimental data show that the center assembly PCT and mass flow rate reached the steady conditions, but the peripheral assembly did not. This was concluded by looking at the rate of change of these variables as a function of time (see Figure 3-33 through Figure 3-37 in Section 3.3.2).

Table 3-10 shows that the CFD predictions matched the experimental data within the experimental error for the center assembly. As the peripheral assembly was still losing heat at 24 hours (i.e., not yet reaching steady state), both the PCT and the mass flow rate were lower than the steady-state CFD predictions.

Figure 3-28 and Figure 3-31 show PCT and external wall temperature as a function of height. There is good agreement between the CFD prediction and experimental data. Figure 3-29 shows the PCT as function of height of the peripheral assembly for the steady CFD predictions using the detailed and porous models and the experimental data at 24 hours. The discrepancies between the predictions and the experimental data are mainly because steady state was not reached in the peripheral assembly. In addition, the porous media model predicted higher PCT than the corresponding detailed model, as the porous model PCT is obtained at the peripheral hot cell wall, whereas the detailed model PCT is in the center of the first row cladding, as shown in Figure 3-32.

Table 3-10 PWR 1x4 Configuration—Steady-State Mass Flow Rate at 1 kW

Model	Temperature (K)			Mass Flow Rate (kg/s)	
	Center Assembly PCT (K)	Peripheral Assembly PCT (K)	Exterior Wall (K)	Center Assembly	Peripheral Assembly
Detailed	472	375	300	0.00040	0.00095
Porous	473	380	300	0.00040	0.00096
Experiment at 24 hours	470	367	300	0.00044	0.00087

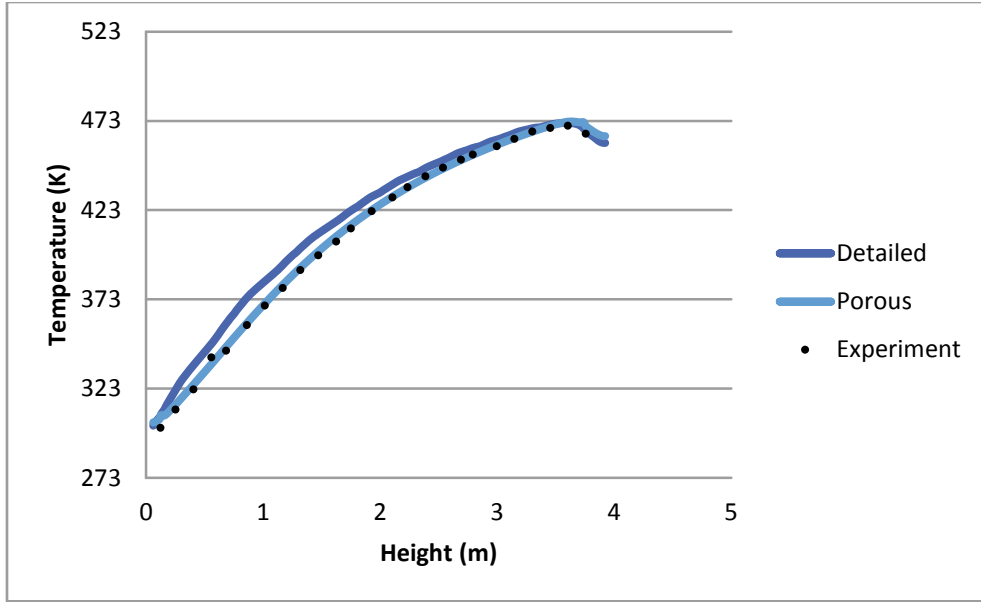


Figure 3-28 PWR 1x4 configuration—steady-state center assembly PCT as a function of height at 1 kW

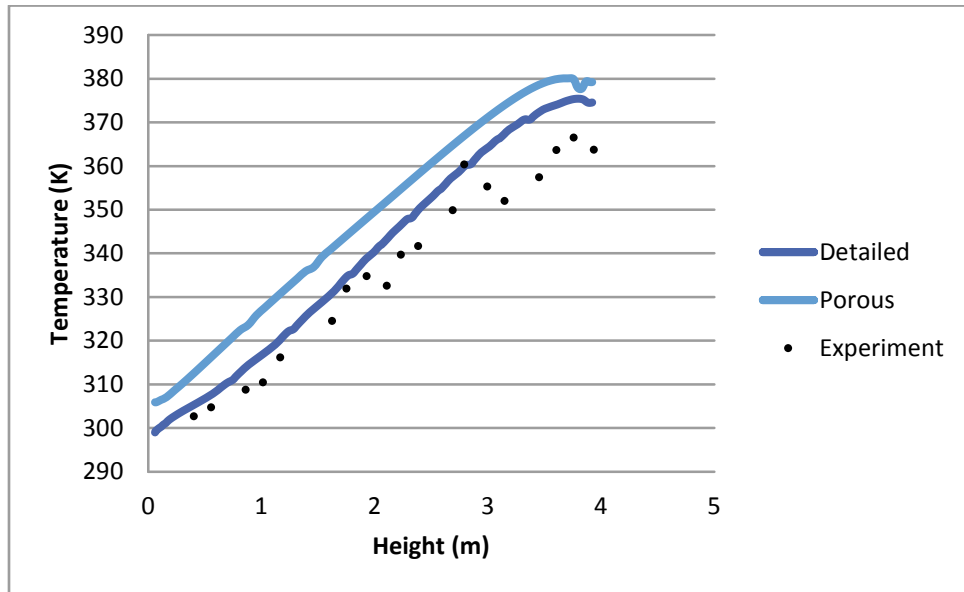


Figure 3-29 PWR 1x4 configuration—steady-state peripheral assembly PCT as a function of height at 1 kW

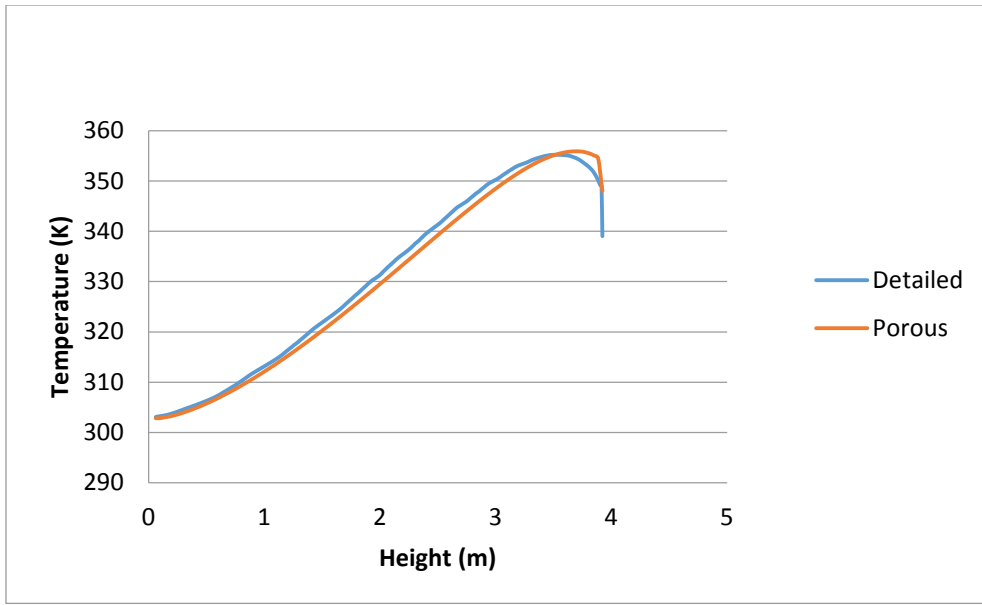


Figure 3-30 PWR 1x4 configuration—steady-state outer pool cell wall maximum temperature as a function of height at 1 kW

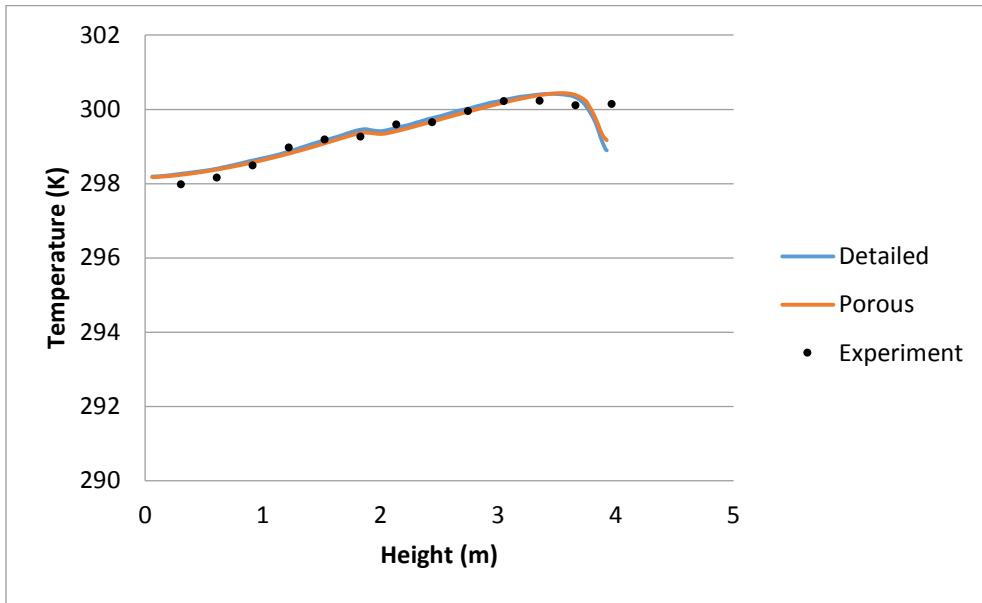


Figure 3-31 PWR 1x4 configuration—steady-state exterior wall maximum temperature as a function of height at 1 kW

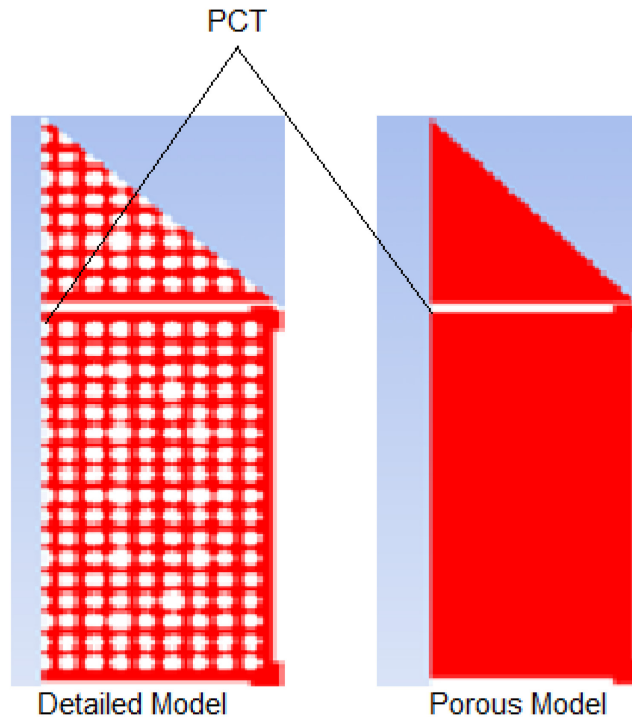


Figure 3-32 PWR 1x4 configuration—PCT location in peripheral assembly

3.3.2 Power—1 kW (Transient)

Figure 3-33 through Figure 3-37 show the center assembly PCT, center assembly mass flow rate, peripheral assembly PCT, peripheral assembly mass flow rate, and the exterior wall temperature as a function of time. The CFD predictions for both the detailed and porous media models and the experimental data agree favorably. Any discrepancy between the predictions and the data can be attributed to the experimental errors, discretization errors, and the thermal mass uncertainty. Figure 3-35 shows that the porous media model predicted slightly higher PCT for the peripheral assembly than the detailed model. This can be attributed to the modeling differences between the two models. The PCT in the porous media is obtained at the hot peripheral cell wall, whereas the PCT in the detailed model is obtained on cladding, as shown in Figure 3-32.

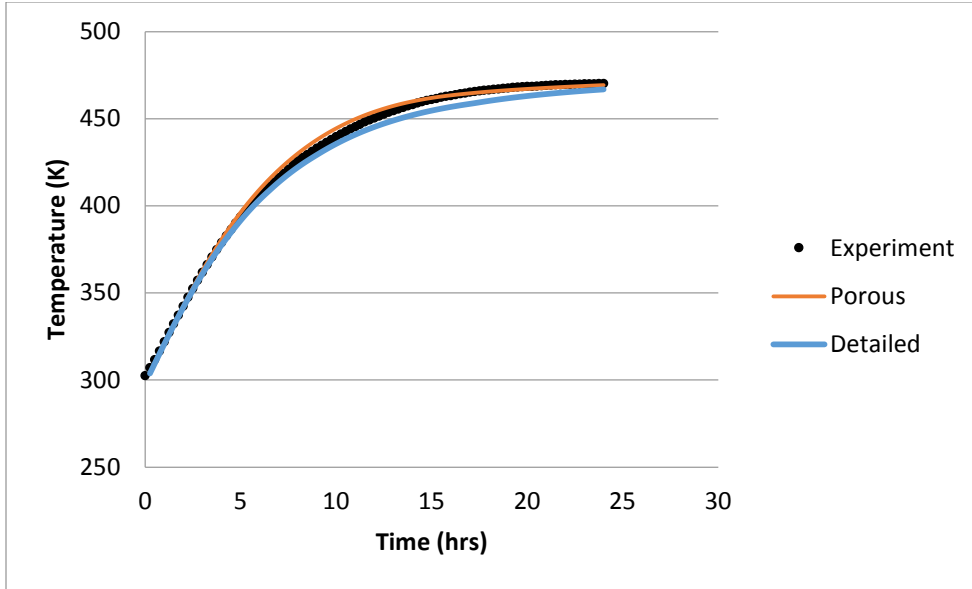


Figure 3-33 PWR 1x4 configuration—center assembly PCT as a function of time at 1 kW

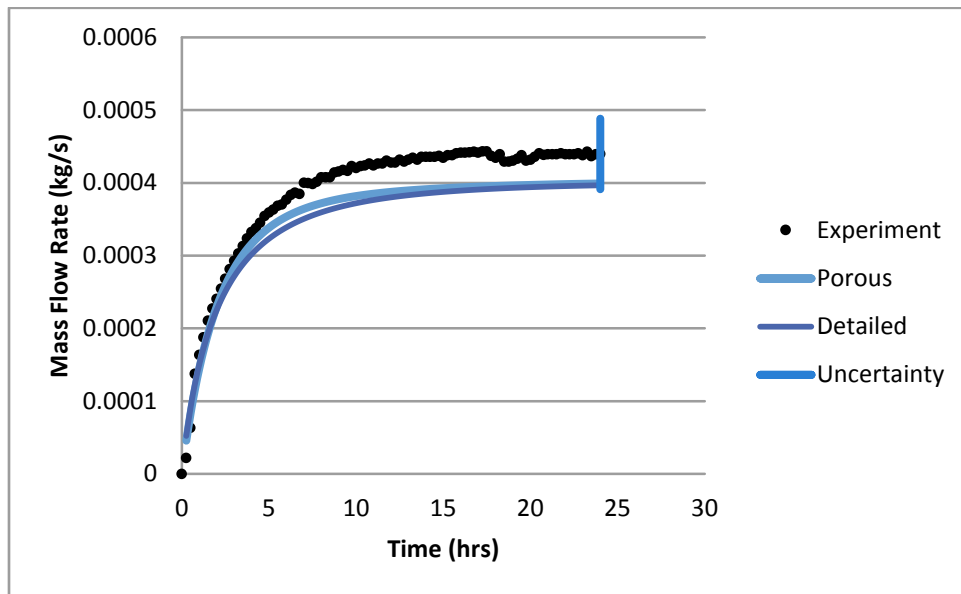


Figure 3-34 PWR 1x4 configuration—center assembly mass flow rate as a function of time at 1 kW

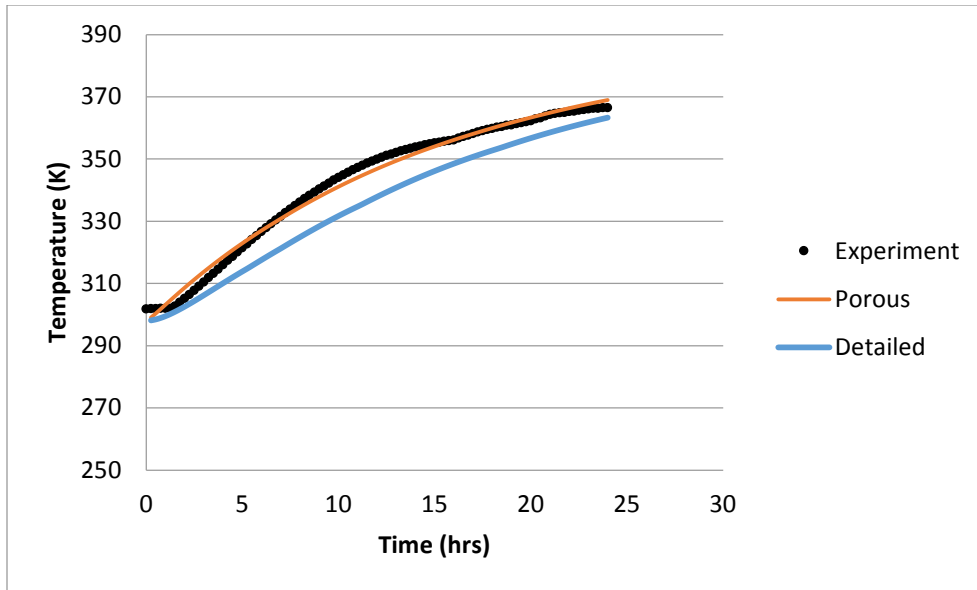


Figure 3-35 PWR 1x4 configuration—peripheral assembly PCT as a function of time at 1 kW

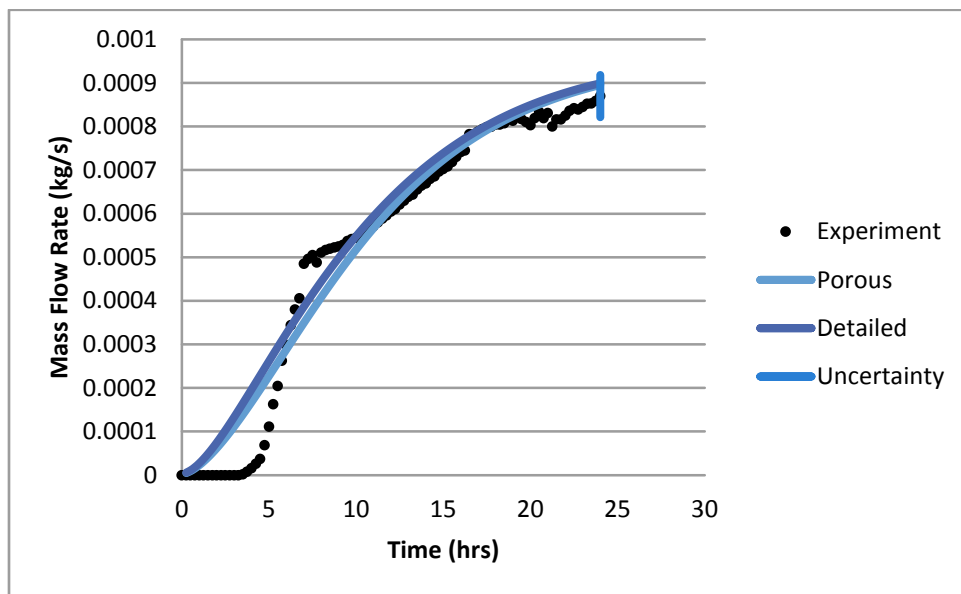


Figure 3-36 PWR 1x4 configuration—peripheral assembly mass flow rate as a function of time at 1 kW

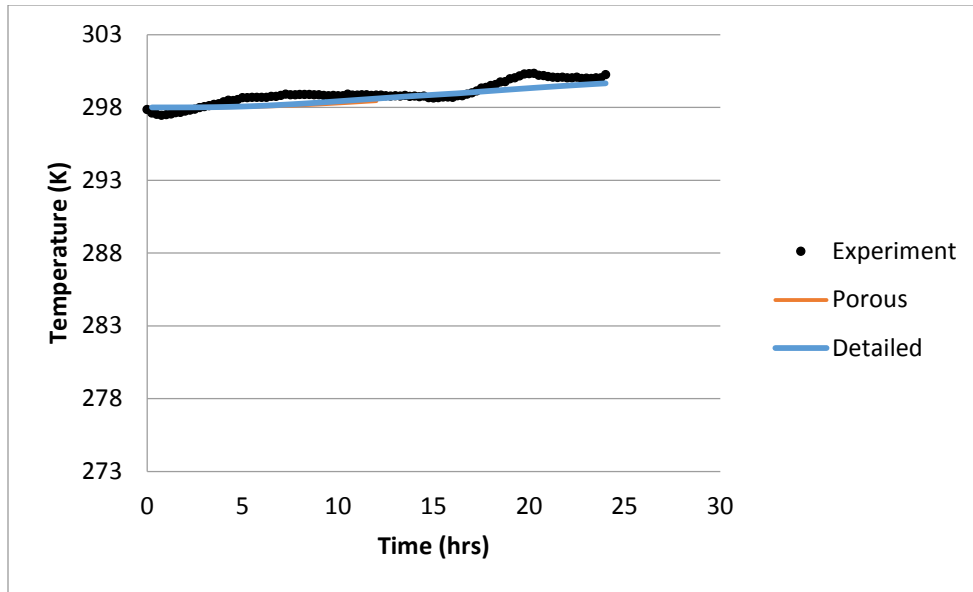


Figure 3-37 PWR 1x4 configuration—exterior wall maximum temperature as a function of time at 1 kW

Figure 3-38 through Figure 3-40 show the PCT of the center assembly, peripheral assembly, and the exterior wall temperature at 24 hours for the CFD predictions using the detailed and the porous models and the experimental data. Figure 3-38 and Figure 3-410 show that the predictions agree favorably with the experimental data. Figure 3-39 shows that the peripheral assembly PCT predicted by the porous media model is slightly higher than the detailed model because of the modeling difference. Table 3-11 shows good agreement between the two CFD models and the experimental data, considering the experimental and discretization errors.

Table 3-11 PWR 1x4 Configuration—PCT and Mass Flow Rate at 1 kW at 24 Hours

Model	Center Assembly		Peripheral Assembly	
	PCT (K)	Mass Flow Rate (kg/s)	PCT (K)	Mass Flow Rate (kg/s)
Experiment	470	0.00044	367	0.00087
Detailed	467	0.00040	363	0.00090
Porous	469	0.00040	369	0.00090

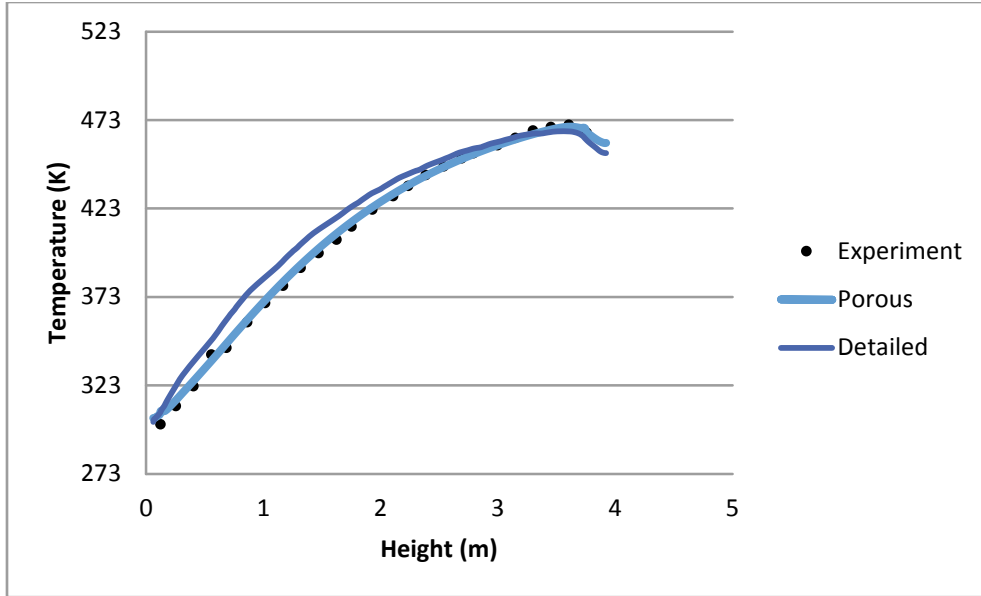


Figure 3-38 PWR 1x4 configuration—center assembly PCT as a function of height at 1 kW at 24 hours

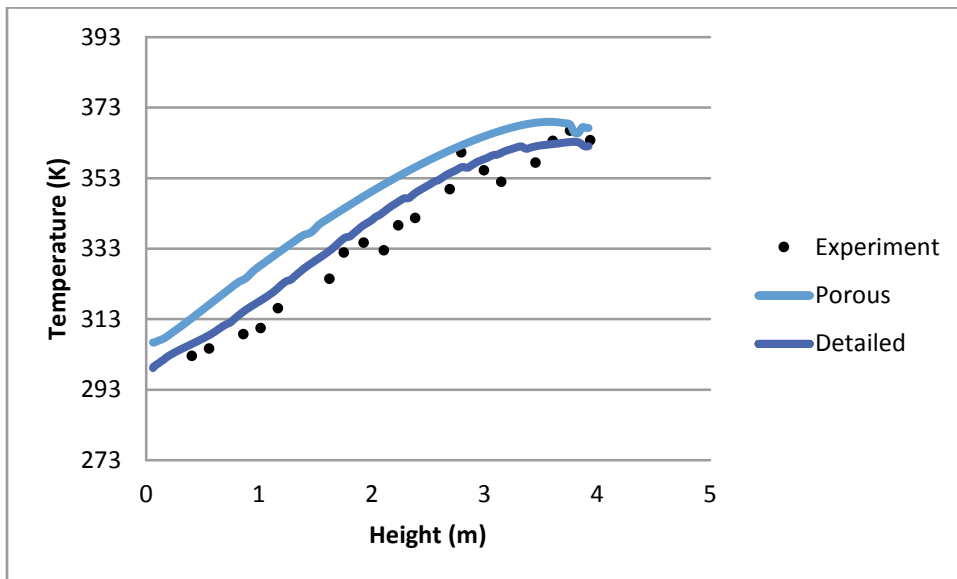


Figure 3-39 PWR 1x4 configuration—peripheral assembly PCT as a function of height at 1 kW at 24 hours

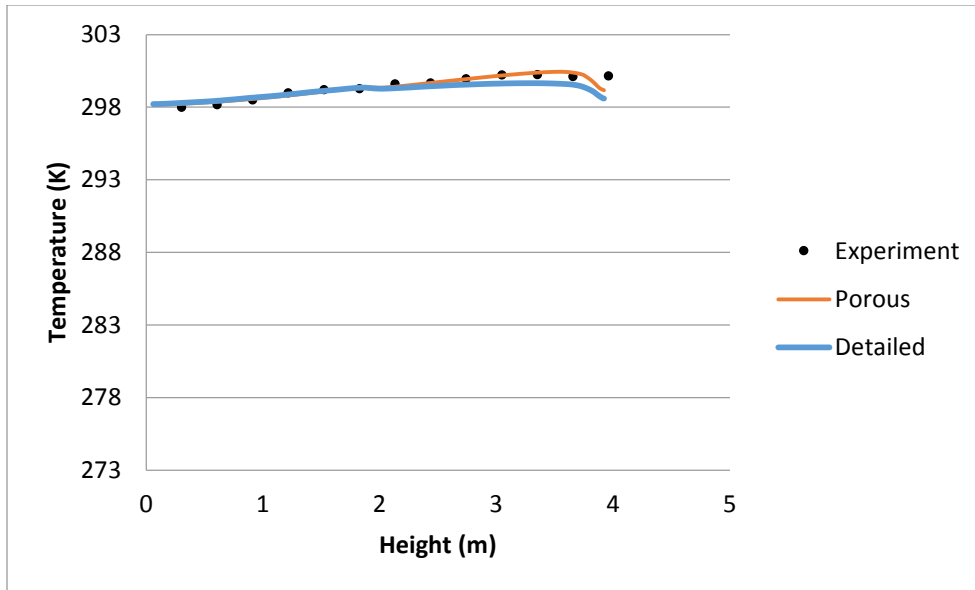


Figure 3-40 PWR 1x4 configuration—exterior wall maximum temperature as a function of height at 1 kW at 24 hours

3.4 Boiling-Water Reactor Single Assembly

This section discusses the results obtained in the experiment, using the detailed and porous CFD models. Both CFD models used 1/4th symmetry. Table 3-12 summarizes the scenarios modeled in this section.

Table 3-12 BWR Single Assembly—Models

Models	Steady State		Transient
Power (W)	1,369	2,236	1,369
Detailed	✓	✓	✓
Porous	✓	✓	✓

3.4.1 Power—1,369 W (Steady State)

Table 3-13 shows the PCT, mass flow rate through the assembly, drain mass flow rate, and the exterior wall temperature for the steady-state case. The table also has the corresponding experimental values at 13 hours. Temperature values from the experiment clearly did not reach steady state; therefore, the figures do not include the temperature values. On the other hand, mass flow through the assembly and the drains already reached the steady-state values as can be seen in Figure 3-45 and Figure 3-46 in Section 3.4.2 .

The mass flow rate through the assembly and drains obtained from CFD compare favorably with the experimental data. Figure 3-41 through Figure 3-43 show the variation of PCT, pool cell wall temperature, and exterior wall temperature as a function of height for the CFD detailed and porous media models. The predictions from the CFD are consistent, considering the discretization error and the differences in the two models.

Table 3-13 BWR Steady-State Mass Flow Rate at 1,369 W

Model	PCT (K)	Mass Flow Rate (kg/s)		Exterior Wall Temperature (K)
		Assembly	Drain Hole	
Detailed	637	0.00055	0.00040	314
Porous	637	0.00059	0.00039	314
Experiment at 13 hours	631	0.00060	0.00040	311

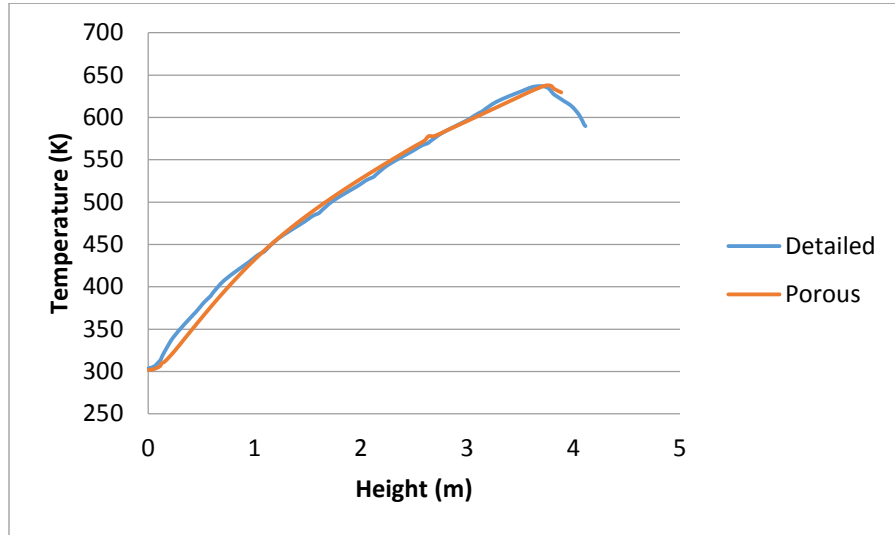


Figure 3-41 BWR steady-state PCT as a function of height at 1,369 W

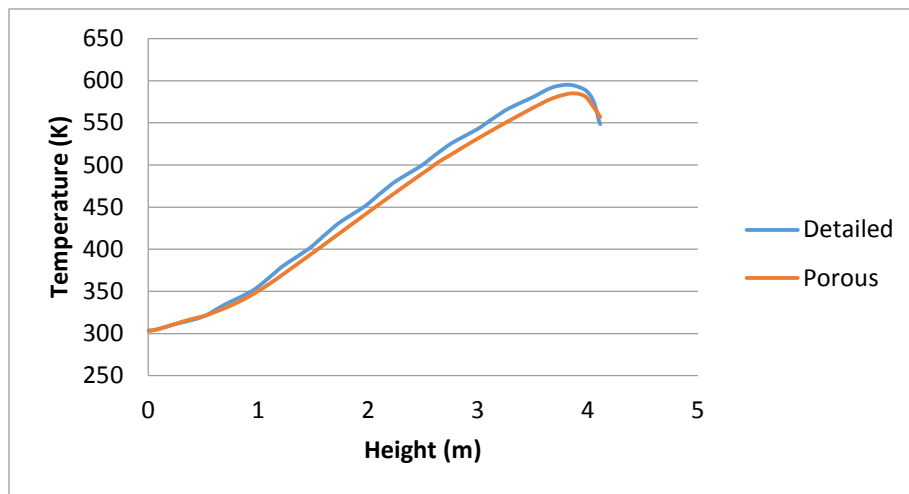


Figure 3-42 BWR steady-state pool cell wall maximum temperature as a function of height at 1,369 W

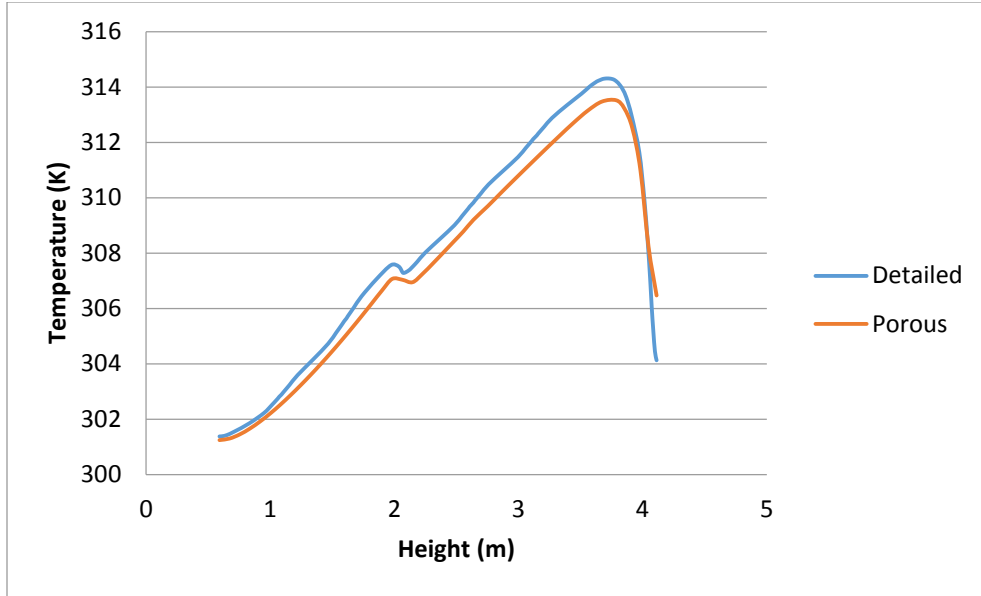


Figure 3-43 BWR steady-state exterior wall maximum temperature as a function of height at 1,369 W

3.4.2 Power—1,369 W (Transient)

Figure 3-44 through Figure 3-48 show the PCT, mass flow rate through the assembly, drain mass flow rate, cell wall temperature, and the exterior wall temperature as a function of time. The predictions from both CFD models agree favorably with the experimental data, considering the measurement uncertainty, discretization error, and thermal mass uncertainty.

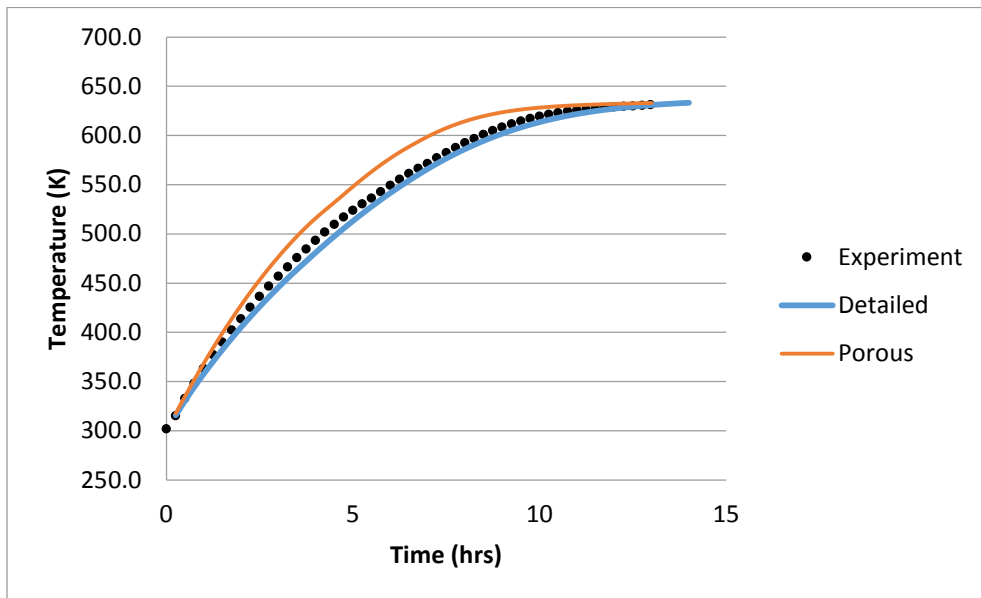


Figure 3-44 BWR PCT as a function of time at 1,369 W

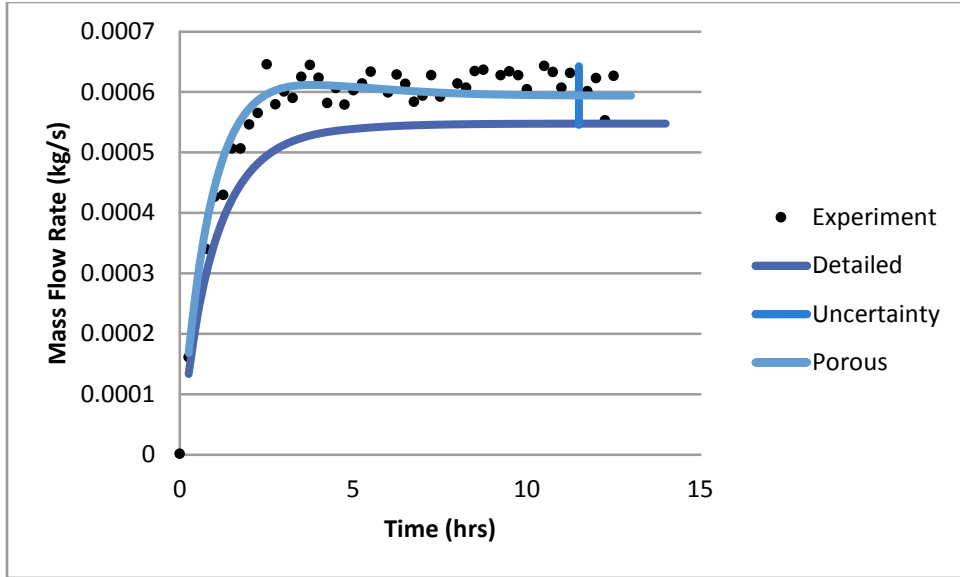


Figure 3-45 BWR inlet bundle mass flow rate as a function of time at 1,369 W

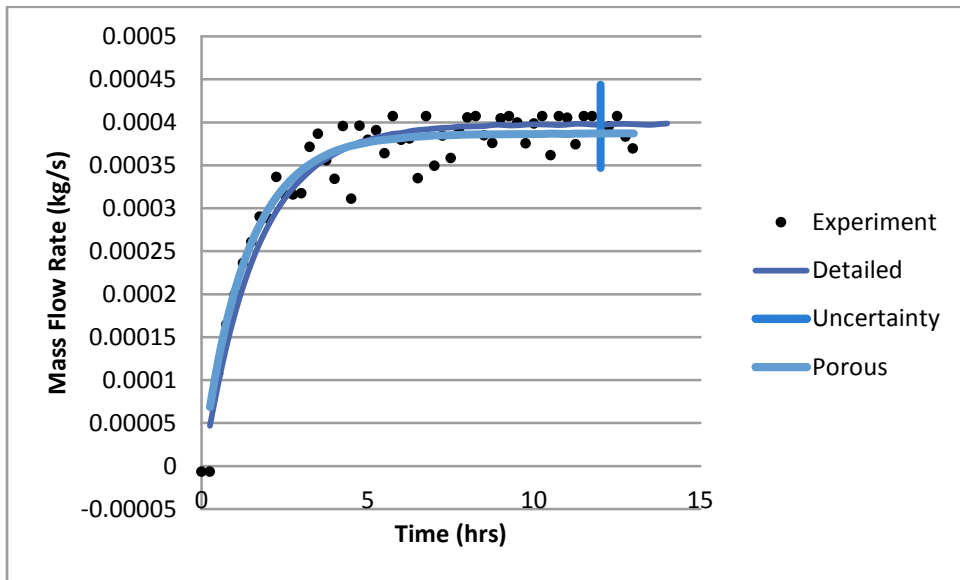


Figure 3-46 BWR inlet drain mass flow rate as a function of time at 1,369 W

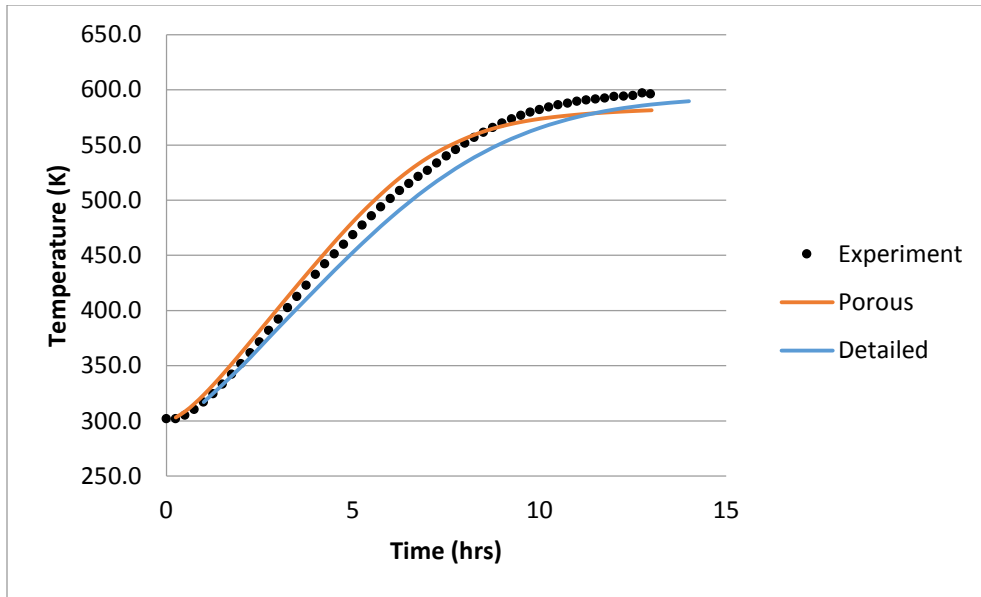


Figure 3-47 BWR pool cell wall maximum temperature as a function of time at 1,369 W

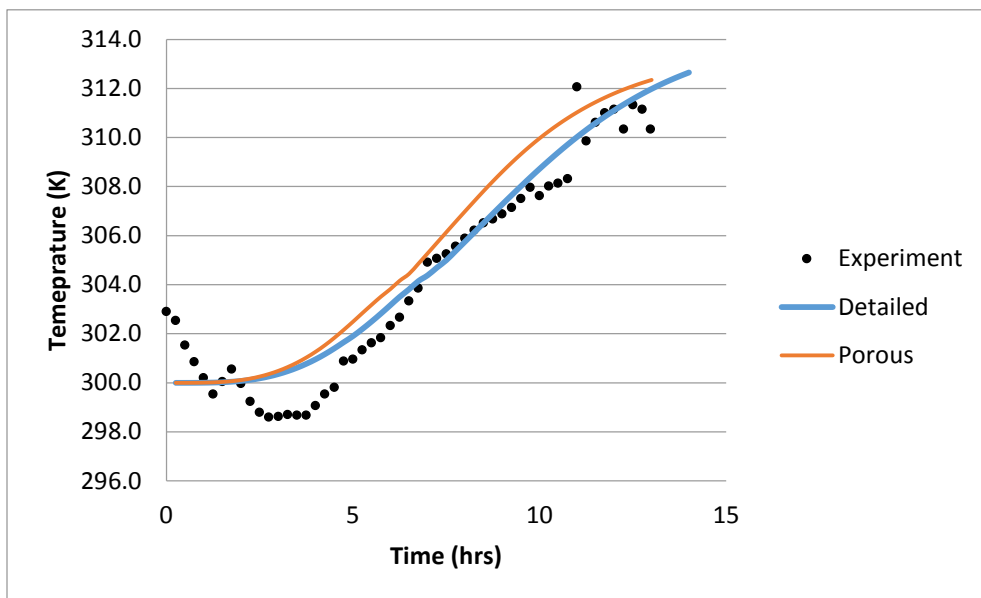


Figure 3-48 BWR exterior wall maximum temperature as a function of time at 1,369 W

Table 3-14 summarizes the PCT, mass flow rate through the assembly, and the drain mass flow rate for the experiment and both CFD models at 12 hours. The CFD predictions from both the detailed and the porous models, shown in Figure 3-49 through Figure 3-51, agree favorably with the experimental data, considering the uncertainties from measurements, discretization, and thermal mass.

Table 3-14 BWR Single Assembly—PCT and Mass Flow Rate at 1,369 W at 12 Hours

Model	PCT (K)	Mass Flow Rate (kg/s)	
		Assembly	Drain Hole
Experiment	629	0.00060	0.00040
Detailed	627	0.00055	0.00040
Porous	632	0.00059	0.00039

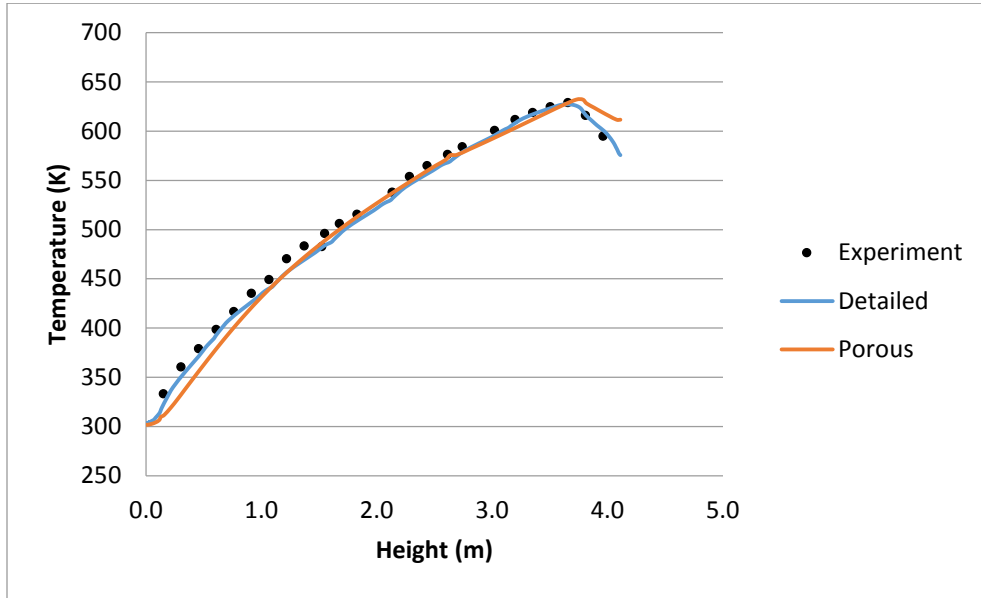


Figure 3-49 BWR PCT as a function of height at 1,369 W at 12 hours

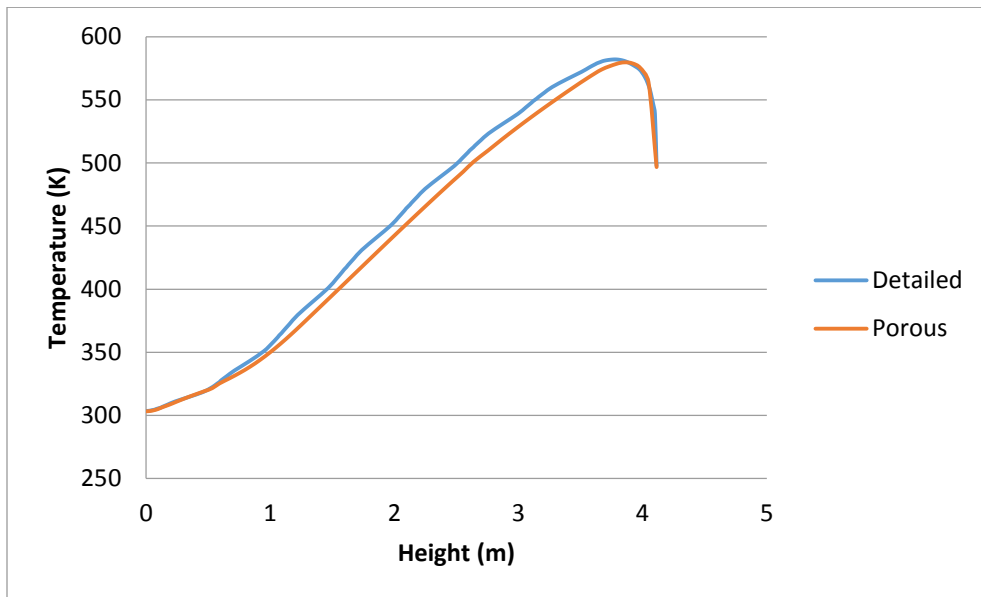


Figure 3-50 BWR pool cell wall maximum temperature as a function of height at 1,369 W at 12 hours

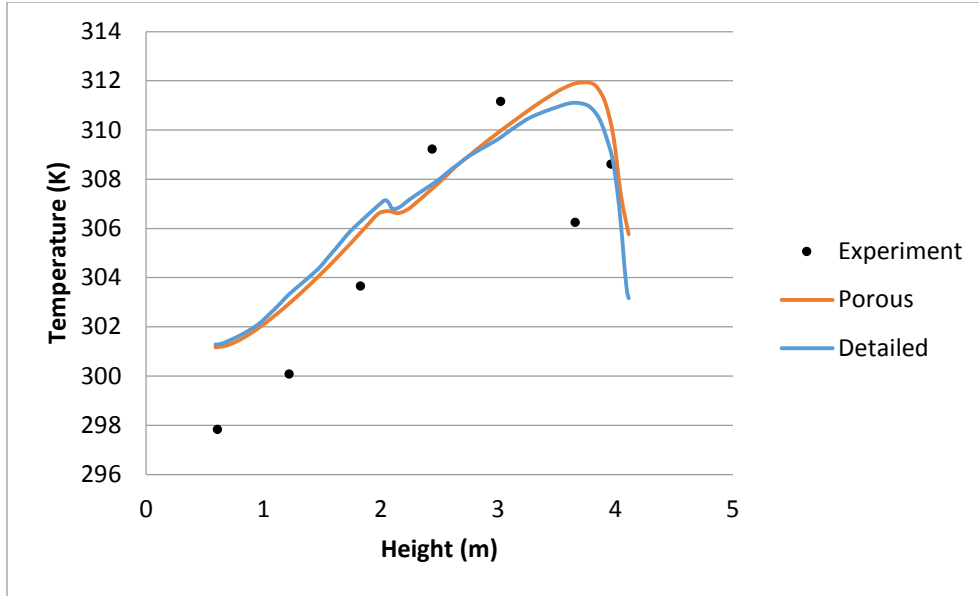


Figure 3-51 BWR exterior wall maximum temperature as a function of height at 1,369 W at 12 hours

3.4.3 Power—2,236 W (Steady State)

Table 3-15 shows the PCT, mass flow rate through the assembly, drain mass flow rate, and the exterior wall temperature for the steady-state case. The table also has the corresponding experimental values at 13 hours. Temperature values from the experiment clearly did not reach steady state; therefore, the figures do not include the temperature values. On the other hand, mass flow through the assembly and the drains already reached the steady-state values. The mass flow rate through the assembly and drains obtained from the CFD compare favorably with the experimental data. Figure 3-52 through Figure 3-54 show the variation of PCT, pool cell wall temperature, and exterior wall temperature as a function of height for the CFD detailed and porous media models. The two CFD model predictions are consistent, considering the discretization error and the differences in the two models.

Table 3-15 BWR Steady-State Mass Flow Rate at 2,236 W

Model	PCT (K)	Mass Flow Rate (kg/s)		Exterior Wall Temperature (K)
		Assembly	Drain Hole	
Detailed	817.8	0.00051	0.00041	328
Porous	818.2	0.00055	0.00041	327
Experiment at 13 hours	792	0.00057	0.00041	320

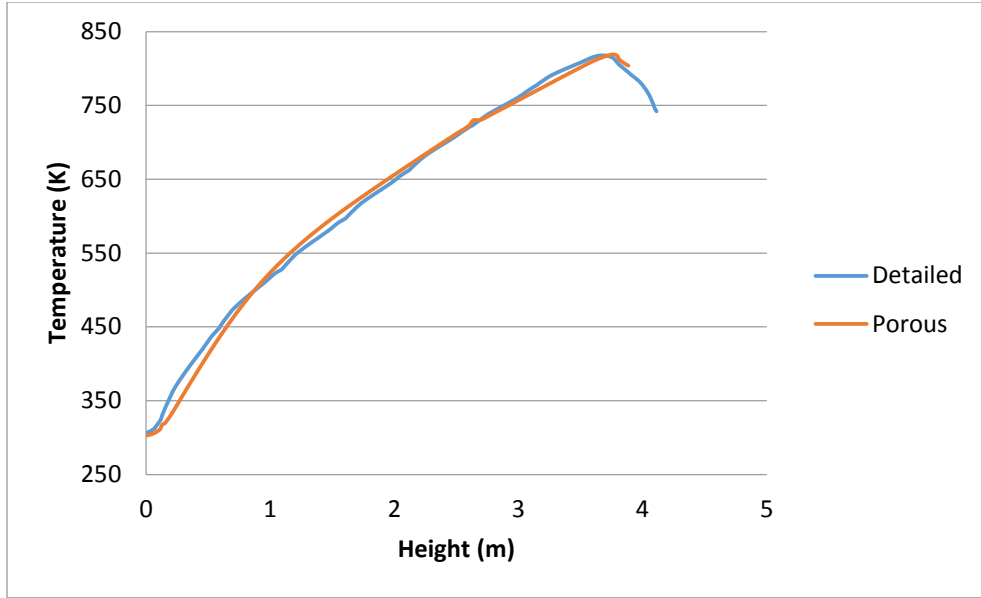


Figure 3-52 BWR steady-state PCT as a function of height at 2,236 W

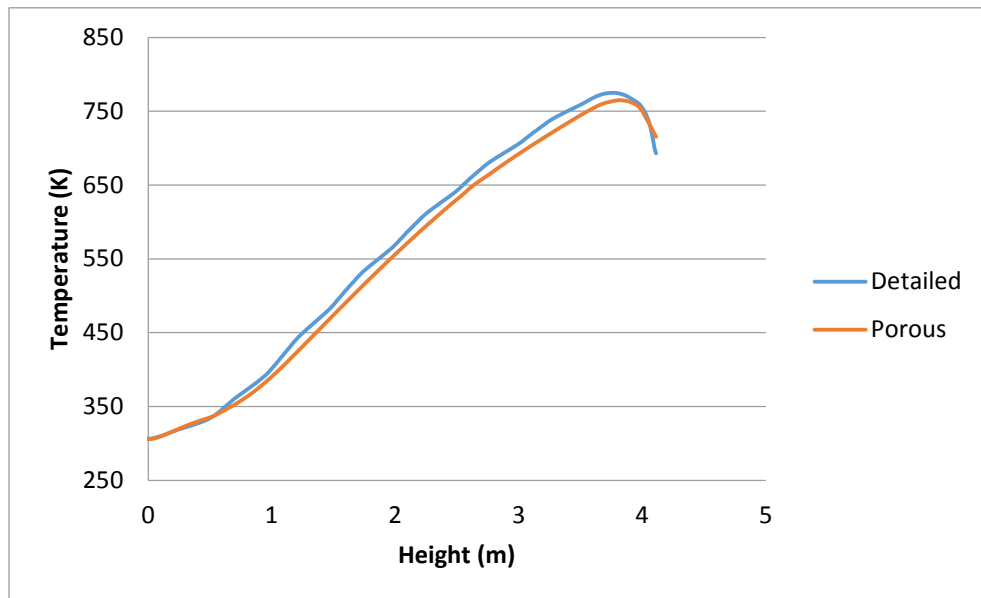


Figure 3-53 BWR steady-state pool cell wall maximum temperature as a function of height at 2,236 W

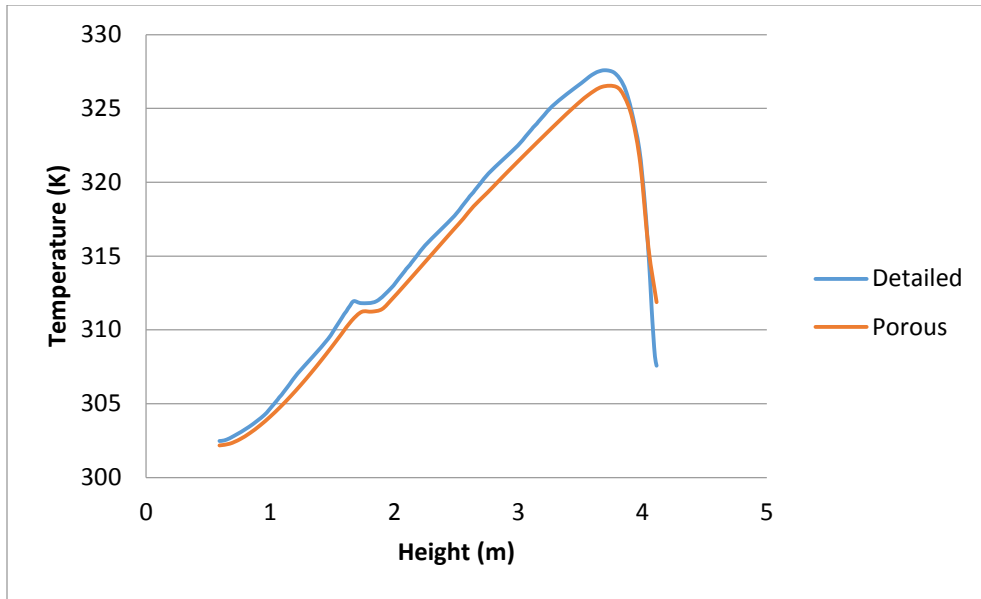


Figure 3-54 BWR steady-state exterior wall maximum temperature as a function of height at 2,236 W

4 COMPUTATIONAL FLUID DYNAMICS DISCRETIZATION ERROR ANALYSIS (GRID CONVERGENCE INDEX)

The credibility and predictive capability of CFD has been greatly enhanced and can be considered a reliable tool for engineering analysis if the numerical errors and uncertainties present in the solution can be reliably estimated. Error and uncertainty for a solver and a solution is formally estimated through a verification and validation process. In 2009, the American Society of Mechanical Engineers published a standard, “Standard for Verification and Validation in Computational Fluid Dynamics and Heat Transfer,” explaining the procedures for code verification, solution verification, and validation of CFD studies. The general objective of the verification and validation process is to estimate the accuracy of a numerical solution.

Validation is the process used to determine whether a model accurately represents the physical phenomena of interest to obtain an estimate of modeling uncertainty. This is primarily done by comparing simulated results with suitable experimental data. Verification deals with the uncertainty of the solution that can be attributed to numerical error, irrespective of how well the solution represents the actual physical process it models. A verification study consists of two components: code verification and solution verification. Code verification is used to demonstrate that the mathematical equations are correctly programmed. It ensures that the solver is free of any coding error and that the solution algorithm has been implemented correctly. In general, developers perform code verification based on evaluation of a known problem by the solver. In contrast, solution verification does not deal with the correctness of a code, but involves estimation of the numerical error or uncertainty for specific simulation results performed by users of a code. Discretization errors and iteration errors are the two main sources of numerical error. The solution verification process is also known as numerical error estimation.

This section presents the methodology and results from the numerical error estimation analysis performed for the PWR Cell 1 single assembly configuration. For this study, the GCI was determined for two representative target variables. These target variables included PCT and mass flow rate through the assembly.

Four mesh levels were used to calculate the GCI. The additional meshes were developed based on systematic refinement or coarsening of a baseline mesh. The approach for mesh refinement and coarsening used in this study was adopted from the guidelines for best practice use of CFD for dry storage cask analysis from NUREG-2152, “Computational Fluid Dynamics Best Practice Guidelines for Dry Cask Applications,” issued March 2013, to determine the approach for mesh refinement and coarsening used in this study. They used Equation 4-1 through Equation 4-8 to calculate the GCI.

$$h = \left[\frac{1}{N} * \sum_{i=1}^N (\Delta V) \right]^{\frac{1}{3}} \quad \text{Equation 4-1}$$

Where:

- h = the grid size
- ΔV = the volume of the i^{th} cell
- N = the total number of cells used for the computations.

Three sets of grids were selected as part of the study. Table 4-1 summarizes these sets.

Table 4-1 Total Number of Cells for Different Grid Levels

Level	Cell Number
1 (finest)	67,000
2	20,636
3	6,750
4 (coarsest)	1,980

To calculate the apparent order of accuracy, p , let $h_1 < h_2 < h_3$, $r_{21} = h_2/h_1$, and $r_{32} = h_3/h_2$.

$$p = \frac{1}{\ln(r_{21})} * \left| \ln \left| \frac{\varepsilon_{32}}{\varepsilon_{21}} \right| + q(p) \right| \quad \text{Equation 4-2}$$

$$q(p) = \ln \left(\frac{r_{21}^p - s}{r_{32}^p - s} \right) \quad \text{Equation 4-3}$$

$$s = 1 * \text{sign} \left(\frac{\varepsilon_{32}}{\varepsilon_{21}} \right) \quad \text{Equation 4-4}$$

where $\varepsilon_{32} = \phi_3 - \phi_2$, $\varepsilon_{21} = \phi_2 - \phi_1$, ϕ_k denoting the solution of the target variable ϕ on the k^{th} grid.

Note that $q(p) = 0$ for $r = \text{const}$. Equation 4-2 can be solved using fixed-point iteration, with the initial guess equal to the first term. The absolute value in Equation 4-2 is necessary to ensure

extrapolation towards $h=0$. Negative values of $\varepsilon_{32}/\varepsilon_{21} < 0$ are an indication of oscillatory

convergence. If possible, the percentage occurrence of oscillatory convergence should also be reported if agreement of the observed apparent order with the formal order of the scheme used can be taken as a good indication of the grids being in the asymptotic range; the converse should not necessarily be taken as a sign of unsatisfactory calculations. It should be noted that if either

$\varepsilon_{32} = \phi_3 - \phi_2$ or $\varepsilon_{21} = \phi_2 - \phi_1$ is "very close" to zero, the above procedure would not work. This might be an indication of oscillatory convergence or, in rare situations, may indicate that the "exact" solution has been attained. In such cases, if possible, calculations with additional grid refinement may be performed; if not, the results may be reported as such.

The extrapolated values can be calculated using the following equation:

$$\phi_{ext}^{21} = \frac{r_{21}^p \phi_1 - \phi_2}{r_{21}^p - 1} \quad \text{Equation 4-5}$$

Similarly, ϕ_{ext}^{32} was calculated.

The approximate relative errors were calculated, respectively:

$$e_a^{21} = \left| \frac{\phi_1 - \phi_2}{\phi_1} \right| \quad \text{Equation 4-6}$$

Finally, the relative GCI was calculated using the following equation:

$$GCI_{fine}^{21} = \frac{3e_a^{21}}{r_{21}^p - 1} \quad \text{Equation 4-7}$$

The absolute error and GCI is obtained by using the following equation:

$$e_a^{21} = |\phi_1 - \phi_2| \quad \text{Equation 4-8}$$

Table 4-2 and Table 4-3 summarize the three combinations and mesh level ratios used for the calculation of the GCI.

Table 4-2 Combinations

	Combination 1	Combination 2	Combination 3
Mesh level	1	1	1
Mesh level	2	2	3
Mesh level	3	4	4

Table 4-3 Mesh Level Ratios

Mesh Level ratio	Combination 1	Combination 2	Combination 3
r21	1.48	1.48	
r32	1.45		
r42		2.18	
r31			2.15
r43			1.51

4.1 Peak Cladding Temperature

Table 4-4 through Table 4-6 summarize the GCI results for the PCT.

Table 4-4 Computed Maximum Temperature

Level	Temperature (K)
1 (finest)	560.2
2	559.8
3	559.3
4 (coarsest)	558.4

Table 4-5 PCT—GCI for Calculated Order of Accuracy

	Combination 1	Combination 2	Combination 3
Order of accuracy (p)	0.3	0.8	1.1
GCI-abs (K)	9.8	11.2	2.0
GCI-relative (%)	1.8	2.0	0.4

Table 4-6 PCT—GCI for Formal Order of Accuracy

	Combination 1	Combination 2	Combination 3
Order of accuracy (p)	1	1	1
GCI-abs (K)	2.8	8.4	2.3
GCI-relative (%)	0.5	1.5	0.4

4.2 Mass Flow Rate

Table 4-7 through Table 4-9 summarize the GCI results for the mass flow rate.

Table 4-7 Computed Mass Flow Rate

Level	Mass flow rate (kg/s)
1 (finest)	0.000413
2	0.000414
3	0.000415
4 (coarsest)	0.000416

Table 4-8 Mass Flow Rate—GCI for Calculated Order of Accuracy

	Combination 1	Combination 2	Combination 3
Order of accuracy (p)	0.6	2.8	0.5
GCI-abs (kg/s)	1.0E-05	2.4E-06	4.2E-06
GCI-relative (%)	2.5	0.6	1.0

Table 4-9 Mass Flow Rate—GCI for Formal Order of Accuracy

	Combination 1	Combination 2	Combination 3
Order of accuracy (p)	1	1	1
GCI-abs (kg/s)	5.6E-06	9.9E-06	1.8E-06
GCI-relative (%)	1.4	2.4	0.4

5 CONCLUSION

The data obtained from the experiments for the single 17x17 PWR and 9x9 BWR assemblies and 17x17 PWR in a 1x4 configuration array provided valuable data for the validation of ANSYS FLUENT 16.0 for dry cask applications. The results in Section 3 of this report show good agreement between the experimental results and the CFD predictions, including both the detailed and porous media models. Data including temperature profiles at different locations such as PCT, pool cell wall, exterior wall temperature, and mass flow rate through the assembly were used for comparison.

Methods to calculate friction factors for the porous media model were developed and tested. The friction factor used in the porous media model as implemented in this investigation provided satisfactory CFD predictions. The CFD predictions showed that the friction factor increases as the pool cell size or the decay heat source decreases. k_{eff} which includes both the conduction and radiation model was tested, and proved effective for use in the porous media model. The tests also showed that the thermal mass can affect the transient data. In addition, selecting the correct heat transfer coefficient at the exterior wall of the control volume allowed the exclusion of the ambient volume from the calculation domain, reducing the computational effort and processing time. The results indicated that porous media model is capable to model the thermal response of an assembly when using the proper input.

The analysis also showed the importance of calculating the error obtained from an experiment as well as the CFD predictions. The validation in this study did not deal with modeling errors, as the study did not consider turbulence modeling. The air flowing through the assembly was in laminar regime for all the cases considered. The only error considered in the CFD predictions performed in this study was the discretization error (i.e., solution verification) or GCI evaluation.

Four levels of meshes were generated to perform the GCI calculations. The variables selected for the GCI analysis were PCT and mass flow rate. Computed data obtained from simulation runs using different grid levels showed little variation. The discretization error for the PCT and air mass flow rate was 2 percent and 2.5 percent, respectively.

The staff recommends that the lessons and guidelines discovered from this work be added to the NUREG-2152, "Computational Fluid Dynamics Best Practice Guidelines for Dry Cask Applications."

6 REFERENCES

American Society of Mechanical Engineers (ASME), "Standard for Verification and Validation in Computational Fluid Dynamics and Heat Transfer," V&V 20-2009.

ANSYS, Inc., ANSYS FLUENT Theory Guide Version 14.5, Canonsburg, PA, 2012a.

ANSYS, Inc., ANSYS FLUENT User Guide Version 14.5, Canonsburg, PA, 2012b.

Bergman, T.L.; Lavine, A.S.; Incropera, F.P.; and DeWitt, D.P., *Fundamentals of Heat and Mass Transfer*, Seventh Edition, John Wiley & Sons New York City, New York, 2011.

Celik, I.B.; Ghia, U.; Roache, P.J.; Freitas, C.J.; Coleman, H.; and Raad, E., "Procedure for Estimation and Reporting of Uncertainty Due to Discretization in CFD Applications," *ASME Journal of Fluids Engineering* (Special Publication), Vol. 130, 2008.

Celik I., and Karatekin, O., "Numerical Experiments on Application of Richardson Extrapolation With Nonuniform Grids," *ASME Journal of Fluids Engineering*, Vol. 119, No 3, pp. 584–590, 1997.

Kays, W., and Crawford, M., *Convective Heat and Mass Transfer*, McGraw-Hill Publishing Company, NY, 1980.

Oberkampf, W.L., and Roy, C.J., *Verification and Validation in Scientific Computing*, Cambridge University Press, Cambridge, Massachusetts, 2010.

Phillips, T.S., and Roy, C., "Evaluation of Extrapolation-Based Discretization Error and Uncertainty Estimators," AIAA-2011-215, Proceedings of the 49th AIAA Aerospace Sciences Meeting, including the New Horizons Forum and Aerospace Exposition, American Institute of Aeronautics and Astronautics, Orlando, Florida, January 4–7, 2011.

Rezende, H.C.; Santos, A.A.; Navarro, M.A.; and Jordao, E., "Verification and Validation of a Thermal Stratification Experiment CFD Simulation," *Nuclear Engineering and Design*, Vol. 248, pp. 72–81, 2012.

Rohsenow, W.M.; Hartnett, J.P.; and Cho, Y.I., *Handbook of Heat Transfer*, 3rd Edition, McGraw-Hill, New York, New York, 1998.

Sucec, J., *Heat Transfer*, William C. Brown Publishers, Dubuque, IA, 1985.

TRW Environmental Safety Systems, Inc., "Spent Nuclear Fuel Effective Thermal Conductivity Report," prepared for U.S. Department of Energy, July 11, 1996.

U.S. Nuclear Regulatory Commission, NUREG-2152, "Computational Fluid Dynamics Best Practice Guidelines for Dry Cask Applications," Washington, DC, March 2013.

U.S. Nuclear Regulatory Commission, NUREG/CR-7143, "Characterization of Thermal-Hydraulic and Ignition Phenomena in Prototypic, Full-Length Boiling Water Reactor Spent Fuel Pool Assemblies After a Postulated Complete Loss-of-Coolant Accident," Washington, DC, March 2013.

U.S. Nuclear Regulatory Commission, NUREG/CR-7215, "Spent Fuel Project Phase I: Pre-Ignition and Ignition Testing of a Single Commercial 17x17 Pressurized Water Reactor Spent Fuel Assembly under Complete Loss of Coolant Accident Conditions," Washington, DC, April 2016.

U.S. Nuclear Regulatory Commission, NUREG/CR-7216, "Spent Fuel Project Phase II: Pre-Ignition and Ignition Testing of a 1x4 Commercial 17x17 Pressurized Water Reactor Spent Fuel Assemblies under Complete Loss of Coolant Accident Conditions," Washington, DC, April 2016.

BIBLIOGRAPHIC DATA SHEET

(See instructions on the reverse)

NUREG-2208

2. TITLE AND SUBTITLE

Validation of Computational Fluid Dynamics Methods Using Prototypic Light Water Reactor Spent Fuel Assembly Thermal-Hydraulic Data

3. DATE REPORT PUBLISHED

MONTH	YEAR
March	2017

4. FIN OR GRANT NUMBER

5. AUTHOR(S)

Ghani Zigh, Sergio Gonzalez

6. TYPE OF REPORT

Technical

7. PERIOD COVERED (Inclusive Dates)

8. PERFORMING ORGANIZATION - NAME AND ADDRESS (If NRC, provide Division, Office or Region, U. S. Nuclear Regulatory Commission, and mailing address; if contractor, provide name and mailing address.)

Division of Systems Analysis
Office of Nuclear Regulatory Research
U.S. Nuclear Regulatory Commission
Washington, DC 20555-0001

9. SPONSORING ORGANIZATION - NAME AND ADDRESS (If NRC, type "Same as above", if contractor, provide NRC Division, Office or Region, U. S. Nuclear Regulatory Commission, and mailing address.)

Division of Spent Fuel Management
Office of Nuclear Material Safety and Safeguards
U.S. Nuclear Regulatory Commission
Washington, DC 20555-0001

10. SUPPLEMENTARY NOTES

11. ABSTRACT (200 words or less)

The research summarized in this report relates to the CFD validation studies performed for a single test assembly of a full-length commercial 17x17 Pressurized Water Reactor (PWR) fuel bundle, a 17X17 PWR 1x4 configuration where the center fuel assembly was electrically heated and the four surrounding assemblies were unheated and a single test assembly for a full-length commercial 9X9 Boiling Water Reactor (BWR) fuel bundle. For each of these configurations, a detailed and porous media model was developed in order to validate the results based on the experimental data. Parametric studies were conducted to assess model sensitivity. The grid conversion index (GCI) method published by the American Society of Mechanical Engineers (ASME) standard Verification and Validation (V&V) 20-2009 was used to calculate the discretization uncertainty of the model.

12. KEY WORDS/DESCRIPTORS (List words or phrases that will assist researchers in locating the report.)

CFD, Validation of Thermal-Hydraulic Data using ANSYS Fluent, GCI

13. AVAILABILITY STATEMENT

unlimited

14. SECURITY CLASSIFICATION

(This Page)

unclassified

(This Report)

unclassified

15. NUMBER OF PAGES

16. PRICE



Federal Recycling Program



UNITED STATES
NUCLEAR REGULATORY COMMISSION
WASHINGTON, DC 20555-0001

OFFICIAL BUSINESS



NUREG-2208

**Validation of Computational Fluid Dynamics Methods Using Prototypic Light Water Reactor
Spent Fuel Assembly Thermal-Hydraulic Data**

March 2017